Large eddy simulations and subgrid scale motions in stratified turbulence

by

Sina Khani

A thesis
presented to the University of Waterloo
in fulfillment of the
thesis requirement for the degree of
Doctor of Philosophy
in
Applied Mathematics

Waterloo, Ontario, Canada, 2015

This thesis consists of material all of which I authored or co-authored: see Statement of Contributions included in this thesis. This is a true copy of the thesis, including any required final versions, as accepted by my examiners.

I understand that my thesis may be made electronically available to the public.

Statement of Contributions

Chapters 2-4 consist of three papers published or submitted for publications in the *Journal of Turbulence* and *Journal of Fluid Mechanics*. These papers present research work that I have performed in my PhD program. The published and submitted papers are co-authored by my co-supervisor, Michael L. Waite, who played a normal supervisory role in the research and made some editing work on the manuscript text.

Abstract

Direct numerical and large eddy simulations (DNS & LES) of decaying and forced stratified turbulence are studied in this thesis. By defining a test filter scale k_c in the horizontal and vertical directions separately, the energy transfer spectra are investigated. It is shown that stratification affects the horizontal eddy viscosity significantly, by which the non-local energy transfer between large and small horizontal scales are increased. This non-local horizontal energy transfer is around 20% of the local horizontal energy transfer at the cut-off wavenumber k_c. In addition, the non-local horizontal energy transfer occurs at large vertical wavenumbers, including the buoyancy wavenumber $k_b = N/u_{rms}$, where N is the buoyancy frequency and u_{rms} is the root-mean-square velocity. The non-local horizontal eddy viscosity decreases and the local eddy viscosity is dominant if the value of the test cutoff k_c varies from large scales to the dissipation scales. Next, the performance of three common subgrid scale (SGS) models, i.e. the Kraichnan, Smagorinsky and dynamic Smagorinsky models, is investigated in stratified turbulence. It is shown that if the grid spacing Δ is small enough, the horizontal wavenumber spectra show an approximately $-5/3$ slope along with a bump at the buoyancy wavenumber k_b. Our results suggest that there is a maximum threshold on Δ, below which the dynamics of stratified turbulence, including Kelvin-Helmholtz instabilities, are captured. This criterion on Δ depends on the buoyancy scale L_b and varies with different SGS models: the Kraichnan model requires $\Delta/L_b < 0.47$, the Smagorinsky model requires $\Delta/L_b < 0.17$ and the dynamic Smagorinsky model requires $\Delta/L_b < 0.24$. In addition, the statistics of the dynamic Smagorinsky coefficient c_s demonstrate that large shear leads to small values of c_s in stratified turbulence (in line with the results for isotropic turbulence). Finally, it is shown that the net down-scale energy transfer in stratified turbulence is a combination of two large values of upscale and downscale energy transfer mechanisms. Overall, our results suggest that stratification changes the dynamics of SGS motions dramatically if the filter scale Δ is around the Ozmidov scale or smaller; in order to capture the dynamical features of stratified turbulence, LES requires resolution of L_b. In addition, when the buoyancy Reynolds number $Re_b \lesssim \mathcal{O}(1)$, the kinetic energy transfer shows some spectral backscatter at intermediate scales that is due to viscous effects and not to the turbulent mechanism.

Acknowledgements

I would like to thank to my co-supervisors Michael Waite and Kevin Lamb for their wonderful supervision, patience and guidance during my PhD program. My special thanks to Michael Waite, this research work was not performed without his instruction, help and support.

In addition, I would like to thank to my external committee member, Julian Andrzej Domaradzki, from the University of Southern California. I have learnt a lot from his work and I think my research is influenced by his publications. Also, I would like to thank to my committee members Marek Stastna, Hans De Sterck and Andrea Scott for their comments and support.

Furthermore, I would like to thank to the Applied Mathematics (AM) Department administrations, Maureen Fraser, Laura Frazee and Cyntia Brătan for having a nice and friendly work environment. Also, thank to the previous graduate coordinators, Helen Warren and Stephanie Martin. Meanwhile, I would like to thank to my friends in the AM department, those are in the fluids laboratory, Christopher Subich, Kris Rowe, Michael Dunphy, Nancy Soontiens, Luke Bovard, James Sandham, John Yawney, Anton Baglaenko, Jared Penney, Wentao Liu, Derek Steinmoeller, Erik Bembenek and those are in other research groups, Mohamad Alwan, Andrew Beltaos, Andree Susanto, Hamid Molavian, Amenda Chow, Ali Mahdipour and Ali Madani.

Finally, I would like to thank to my family for their love, support and patience. In particular, I would like to thank to my mom Fatemeh, without whom I never could be at this level. Also, I would like to thank to my fiancée, Farinaz, for her love and encouragement.

Dedication

In memory of my brother Soheil ... secret tears and loving thoughts would be with us forever.

Table of Contents

List of Tables

List of Figures

Chapter 1

Introduction

1.1 Overview

Turbulent flows are prevalent in atmosphere, ocean and engineering applications. In all of these fields, turbulence shows unsteady, irregular, and chaotic behaviours, in which the motions of different eddies are unpredictable. Turbulence may be classified by a specific characteristic in addition to its general features. For example, turbulence may be affected by shear, boundaries, rotation, magnetic fields, stratification, etc. These parameters complicate our understanding of turbulence, and require adjustments to the classical picture presented by Kolmogorov (1941). Turbulence includes a range of length scales: from large-scale motions, which set the turbulence parameters like the length scale $\mathcal{L}$, the velocity scale $\mathcal{U}$ and the kinetic dissipation rate ϵ; to small scales, which mainly are Re-dependent motions, where

$$Re = \frac{\mathcal{U}\mathcal{L}}{\nu}, \tag{1.1}$$

is the Reynolds number and ν is the kinematic molecular viscosity.

An important property of turbulence is the transfer of energy between different length scales. The dynamics of the energy cascade between large and small scales depends on the type of turbulence. For isotropic turbulence, cascade is downscale Kolmogorov (1941). Different physical phenomena such as stratification, shear and rotation may affect the dynamics of the energy cascade dramatically. The objective of this thesis is studying turbulence that is strongly affected by stable density stratification, namely stratified turbulence. Stratified turbulence occurs in the atmospheric mesoscale and oceanic sub-mesoscale, at

which scale eddies are strongly affected by stable stratification, but weakly affected by the Earth's rotation (e.g. Riley & Lelong, 2000). Stratification refers to the density changes in the vertical direction, and it has a profound affect on the vertical displacement of fluid particles.

Large eddy simulation (LES) is a numerical approach that resolves large energy containing scales and parametrizes the subgrid scale (SGS) motions. Since LES does not require one to directly resolve the smallest scales, it allows a larger grid spacing Δ that leads to a decrease in the computational costs. To do this, LES defines a filter scale that is generally the grid spacing Δ. Scales larger than Δ are resolved directly, but sub-filter scale motions are parametrized using SGS models. In this thesis, the actual features of SGS motions are studied in stratified turbulence using the direct numerical simulation (DNS) approach. Also, the performance of common SGS models are investigated in LES of stratified turbulence. Since the following chapters are written to be self-contained, this introduction presents background information on numerical approaches, stratified turbulence, LES and SGS modelling that is not included later. More detailed background and literature review is given in the following chapters.

1.2 Stratified turbulence

There is a long history in the stratified turbulence literature about the direction of the energy cascade and the shape of the horizontal wavenumber energy spectrum. One point of view, which was presented by Gage (1979) and Lilly (1983), argued for an upscale energy transfer in the horizontal direction of stratified turbulence in analogy with two-dimensional turbulence. However, more recent numerical studies on stratified turbulence (e.g. Riley & de Bruyn Kops, 2003; Waite & Bartello, 2004; Lindborg, 2006; Brethouwer et al., 2007; Waite, 2011; Kimura & Herring, 2012; Remmler & Hickel, 2012; Khani & Waite, 2013, 2014a,b) suggest a downscale energy cascade in horizontal wavenumber. In the presence of stratification, the classical picture of the energy spectrum for isotropic turbulence needs some modifications. Stratification introduces two new length scales: the buoyancy length scale (e.g. Billant & Chomaz, 2001)

$$L_b = \frac{\mathcal{U}}{N}, \tag{1.2}$$

and the Ozmidov length scale (e.g. Lumely, 1964)

$$L_o = \left(\frac{\epsilon}{N^3}\right)^{1/2}. \tag{1.3}$$

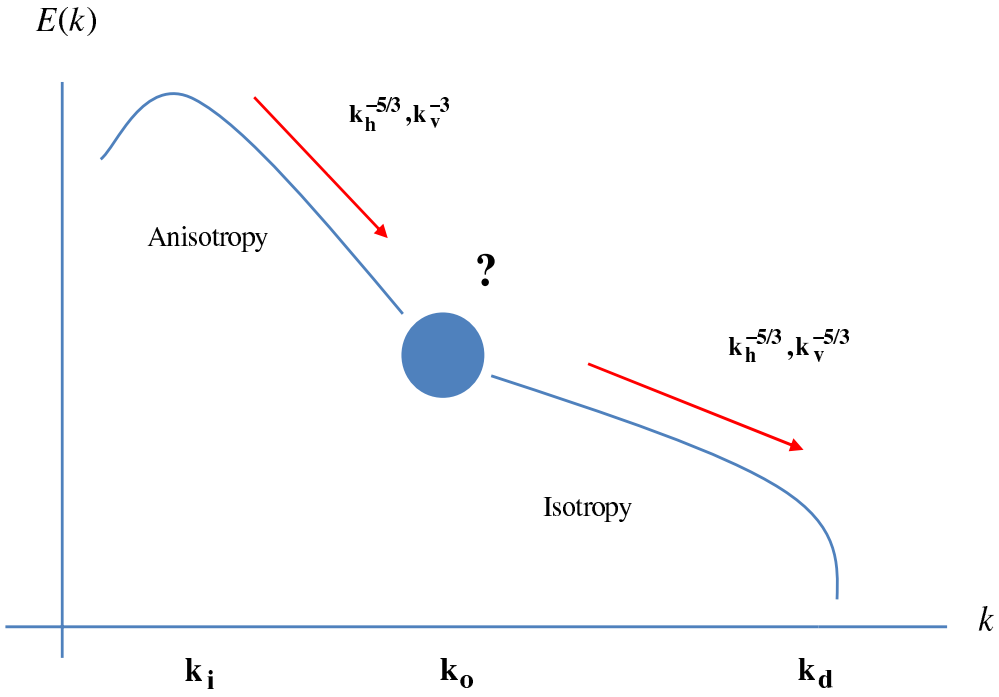

Figure 1.1: Schematic energy spectrum based on the stratified turbulence hypothesis, where k_i, k_o and k_d are the initial, Ozmidov and Kolmogorov wavenumbers, respectively, and the subscripts h and v denote accordingly the horizontal and vertical directions.

The buoyancy scale is the characteristic length scale in the vertical direction of stratified turbulence, where the elongated horizontal motions are layered vertically with the length scale L_b (e.g. Billant & Chomaz, 2001; Waite & Bartello, 2004). The Ozmidov scale is the smallest scale for which buoyancy effects are important, below which isotropic turbulence should occur (e.g. Lindborg, 2006). It is important to mention that $L_b > L_o$ in stratified turbulence (see below). According to the Lindborg (2006) stratified turbulence hypothesis, the energy spectrum for scales larger than the Ozmidov scale is anisotropic in which the horizontal and vertical wavenumber spectra have with different power laws. Nevertheless, for scales smaller than the Ozmidov scale, the isotropic Kolmogorov cascade is assumed to be valid (figure 1.1). As a result, setting a filter scale that is larger than the Ozmidov scale might necessitate a SGS model which is totally different than that when the filter scale is smaller than the Ozmidov scale. In other words, current SGS models, most of which are

designed for isotropic turbulence, may not be relevant for cases with $\Delta > L_o$. Therefore, studying SGS motions for which the filter scale is close to or larger than the Ozmidov scale is a necessary step of research in LES of stratified turbulence.

1.2.1 The governing equations

The dynamics of stratified turbulence can be described using the Navier-Stokes equations subjected to the Boussinesq approximation, in which the density perturbation $\rho - \rho_0$ is small compared to the constant reference density ρ_0, as follows (following the notation of Chung & Matheou, 2012)

$$\frac{\partial \boldsymbol{u}}{\partial t} + \boldsymbol{u} \cdot \nabla \boldsymbol{u} = -\frac{1}{\rho_0}\nabla(p + \rho_0 g z) + \nu \nabla^2 \boldsymbol{u} - \frac{g}{\rho_0}(\rho - \rho_0)\boldsymbol{e}_z, \tag{1.4}$$

$$\nabla \cdot \boldsymbol{u} = 0, \tag{1.5}$$

$$\frac{\partial(\rho - \rho_0)}{\partial t} + \boldsymbol{u} \cdot \nabla(\rho - \rho_0) = D\nabla^2(\rho - \rho_0), \tag{1.6}$$

where $\boldsymbol{u}$ is the velocity vector which includes three components u, v and w in $\boldsymbol{e}_x$, $\boldsymbol{e}_y$ and $\boldsymbol{e}_z$ directions, respectively; ρ and p are the density and pressure fields; ρ_0 is a constant reference density; and D is the mass or thermal diffusivity. We decompose the flow into background and fluctuation components, denoted by overbar and primes, respectively. Assuming linear background density gradient, the decomposition is written as

$$-\frac{g}{\rho_0}(\rho - \rho_0) = N^2 z - \frac{g}{\rho_0}\rho', \tag{1.7}$$

$$\boldsymbol{u} = \boldsymbol{u}', \tag{1.8}$$

$$p + \rho_0 g z = \rho_0 N^2 z^2/2 + p', \tag{1.9}$$

where $N^2 = -g/\rho_0(d\bar{\rho}/dz)$ is the buoyancy frequency, which assumed to be constant. Substituting the flow variables at (1.7-1.9) into the primary equations at (1.4-1.6), yields

$$\frac{\partial \boldsymbol{u}'}{\partial t} + \boldsymbol{u}' \cdot \nabla \boldsymbol{u}' = -\frac{1}{\rho_0}\nabla p' - \frac{g}{\rho_0}\rho' \boldsymbol{e}_z + \nu \nabla^2 \boldsymbol{u}', \tag{1.10}$$

$$\nabla \cdot \boldsymbol{u}' = 0, \tag{1.11}$$

$$\frac{\partial \rho'}{\partial t} + \boldsymbol{u}' \cdot \nabla \rho' + w' \frac{d\bar{\rho}}{dz} = D\nabla^2 \rho', \tag{1.12}$$

which are the main equations that we will use in our simulations of stratified turbulence. For simplicity and clarity, we non-dimensionalize equations (1.10-1.12) with velocity scale $\mathcal{U}$, length scale $\mathcal{L}$, and time scale $\mathcal{L}/\mathcal{U}$. Dropping primes, the dimensionless equations are as follows

$$\frac{\partial \boldsymbol{u}}{\partial t} + \boldsymbol{u} \cdot \nabla \boldsymbol{u} = -\nabla p - \frac{1}{F^2}\rho \boldsymbol{e}_z + \frac{1}{Re}\nabla^2 \boldsymbol{u}, \tag{1.13}$$

$$\nabla \cdot \boldsymbol{u} = 0, \tag{1.14}$$

$$\frac{\partial \rho}{\partial t} + \boldsymbol{u} \cdot \nabla \rho - w = \frac{1}{RePr}\nabla^2 \rho, \tag{1.15}$$

where F is the Froude number (see below) and $Pr = \nu/D$ is the Prandtl number. In the atmosphere and ocean, the buoyancy frequency generally varies with height. However, there are certain layers over which N is approximately constant. Nevertheless, the assumption of constant N is common in the idealized studies of stratified turbulence (e.g. Riley & de Bruyn Kops, 2003; Waite & Bartello, 2004; Lindborg, 2006; Brethouwer et al., 2007; Waite, 2011).

The importance of stratification is characterized by the Froude number, which shows the ratio of the buoyancy time scale $1/N$ to the turnover time $\mathcal{L}/\mathcal{U}$, written as

$$F = \frac{\mathcal{U}}{N\mathcal{L}}. \tag{1.16}$$

In the anisotropic part of the inertial subrange of stratified turbulence, we can define the horizontal and vertical Froude numbers as follows

$$F_h = \frac{\mathcal{U}}{N\mathcal{L}_h}, \tag{1.17}$$

$$F_v = \frac{\mathcal{U}}{N\mathcal{L}_v}, \tag{1.18}$$

where $\mathcal{L}_h$ and $\mathcal{L}_v$ are the appropriate length scales in the horizontal and vertical directions, respectively. If we perform a dimensional analysis on the set of equations (1.10-1.12) based on the buoyancy time scale $t_b \sim \mathcal{L}_h/N\mathcal{L}_v$, the internal wave equations result when $F_v \ll 1$ (see e.g. Riley & Lelong, 2000). However, if the advection time scale $t_a \sim \mathcal{L}_h/\mathcal{U}$ is used, the resulting equations are more appropriate for stratified turbulence when $F_h \ll 1$ and $F_v \sim 1$ (see e.g. Brethouwer et al., 2007). If Re is very high such that $Re_b \gg 1$, F_z will be ~ 1, therefore the two key parameters are F_h and Re, by which if $F_h \ll 1$ and the buoyancy

Reynolds number (e.g. Riley & de Bruyn Kops, 2003; Hebert & de Bruyn Kops, 2006b; Brethouwer et al., 2007; Almalkie & de Bruyn Kops, 2012; Bartello & Tobias, 2013)

$$Re_b = ReF_h^2, \tag{1.19}$$

is very high, stratified turbulence is ensured. Here, Re is defined using $\mathcal{L}_h$. Using the Taylor hypothesis (e.g. Pope, 2000) to define the horizontal length scale $\mathcal{L}_h \sim \mathcal{U}^3/\epsilon$, we could define an alternative approximation for Re_b using the flow parameters as the following (this is sometimes taken as the primary definition of Re_b, e.g. Smyth & Moum, 2000)

$$Re_b \sim \frac{\epsilon}{\nu N^2}. \tag{1.20}$$

In the regime with small horizontal Froude number, the vertical lengthscale is much smaller than the horizontal lengthscale

$$\frac{\mathcal{L}_v}{\mathcal{L}_h} \sim \frac{\mathcal{U}/N}{\mathcal{L}_h} \equiv F_h \ll 1. \tag{1.21}$$

Using the Taylor hypothesis, we can also get

$$\frac{L_b}{L_o} \equiv F_h^{-1/2} > 1. \tag{1.22}$$

In this regime, Lindborg (2006) argued that the horizontal and vertical energy spectra are solely dependent to the horizontal and vertical lengthscales, respectively, written as

$$E(k_h) = \mathcal{U}^2 \mathcal{L}_h \mathcal{E}_h(k_h \mathcal{L}_h), \tag{1.23}$$

$$E(k_v) = \mathcal{U}^2 \mathcal{L}_v \mathcal{E}_v(k_v \mathcal{L}_v), \tag{1.24}$$

where $\mathcal{E}_h(k_h\mathcal{L}_h)$ and $\mathcal{E}_v(k_v\mathcal{L}_v)$ are non-dimensional functions. Using the Taylor hypothesis and assuming that the characteristic horizontal and vertical scales are much larger than the Ozmidov scale, it is concluded that the horizontal and vertical wavenumber energy spectra do not depend on the buoyancy frequency N and the kinetic dissipation rate ϵ, respectively (see Lindborg, 2006). As a result, the horizontal and vertical energy spectra in the inertial subrange of stratified turbulence could be written as follows

$$E(k_h) \sim \epsilon^{2/3} k_h^{-5/3}, \tag{1.25}$$

$$E(k_v) \sim N^2 k_v^{-3}. \tag{1.26}$$

A similar argument was also suggested by Dewan (1997). Using atmospheric observations, Lindborg (2006) has estimated the critical horizontal Froude number for which motions are dominated by stratified cascade to be

$$F_h^{critic} \approx 0.02. \tag{1.27}$$

In this thesis, this criterion on F_h is considered as a characteristic for a stratified turbulence cascade.

1.3 Numerical simulations

Turbulent flows can be studied experimentally or numerically, and both approaches have advantages and disadvantages. In this thesis, we consider the latter and investigate stratified turbulence using numerical simulations. There are two common numerical approaches for simulations of turbulent flows: DNS and LES. In DNS, we resolve all scales from the large energy-containing scale, which is set by the initial conditions and/or forcing, down to the Kolmogorov scale

$$L_d = \left(\frac{\nu^3}{\epsilon}\right)^{1/4}, \tag{1.28}$$

at which viscous dissipation occurs (e.g. Pope, 2000). For small and moderate Re, DNS is the ideal choice since it directly resolves all scales without any needs for parametrizations. However, Re in the atmosphere and ocean is around $\mathcal{O}(10^8)$ or higher (e.g. Vallis, 2006; Waite, 2014). Such large Re are well beyond what can be captured by DNS because of limited computational resources. For example, the DNS of stratified turbulence by Almalkie & de Bruyn Kops (2012), which is one of the largest available DNS, includes Re of the order 10^4. Recently, Piomelli (2014) argues that a numerical simulation with Re of the order $\mathcal{O}(10^8)$ will not be possible until 2070.

LES is an alternative approach, in which the large scale motions are resolved, but small subgrid scale features are parameterized. Hypothetically, if the Re is very large in isotropic turbulence, there is a clear separation between large and small scales. This gap between large and small scales, called the inertial subrange, is characterized by energy transfer from the energy-containing range (large scales) to the dissipation range (small scales) through a self-similar mechanisms (i.e. energy cascade, e.g. Pope, 2000). The LES approach defines a filter scale (the grid spacing Δ) inside the inertial subrange, such that large scales are directly resolved, but subgrid small scales are not captured. Since LES

filters the dissipation range, we need a dissipative mechanism to model SGS eddies for the sake of numerical stability and realistically capture the downscale cascade, e.g. the eddy-viscosity hypothesis (e.g. Pope, 2000). There are several different types of filtering operators and SGS models in the physical and wavenumber space (see next chapters).

1.3.1 DNS

DNS resolves all scales from the large scale $\mathcal{L}$ down to the Kolmogorov scale L_d. Hence, the dissipation mechanism for DNS is molecular viscosity. Spectral methods are ideal numerical schemes for the spatial discretization because of their high accuracy. Assuming periodic boundary conditions, the flow variables are represented by truncated Fourier series, e.g. for the velocity

$$\boldsymbol{u}(\boldsymbol{x},t) = \sum_{\boldsymbol{k}} \hat{\boldsymbol{u}}(\boldsymbol{k},t) e^{i\boldsymbol{k}\cdot\boldsymbol{x}}, \tag{1.29}$$

where $\boldsymbol{k} = (k_1, k_2, k_3)$ is the wavenumber and $\hat{\boldsymbol{u}}(\boldsymbol{k},t)$ is the Fourier coefficient of $\boldsymbol{u}(\boldsymbol{x},t)$. The range of $\boldsymbol{k}$ is set by the size of the domain in each direction (see below). In this situation, the governing equations of motion (1.13-1.15) can be rewritten as

$$(\frac{\partial}{\partial t} + \frac{k^2}{Re})\hat{u}_j(\boldsymbol{k},t) + \frac{1}{F^2}\hat{\rho}(\boldsymbol{k},t)\boldsymbol{e}_z = -ik_m P_{jr}(\boldsymbol{k}) \sum_{\boldsymbol{p}+\boldsymbol{q}=\boldsymbol{k}} \hat{u}_r(\boldsymbol{p},t)\hat{u}_m(\boldsymbol{q},t), \tag{1.30}$$

$$k_i\hat{u}_i(\boldsymbol{k},t) = 0, \tag{1.31}$$

$$(\frac{\partial}{\partial t} + \frac{k^2}{RePr})\hat{\rho}(\boldsymbol{k},t) - \hat{w}(\boldsymbol{k},t) = -ik_m \sum_{\boldsymbol{p}+\boldsymbol{q}=\boldsymbol{k}} \hat{u}_m(\boldsymbol{p},t)\hat{\rho}(\boldsymbol{q},t), \tag{1.32}$$

where $k = \sqrt{k_1^2 + k_2^2 + k_3^2}$ and $P_{ij}(\boldsymbol{k}) = \delta_{ij} - k_i k_j/k^2$ is the projection tensor that is used to eliminate the pressure term (e.g. Rose & Sulem, 1978). We have assumed that the density perturbations are periodic. It is worthwhile to note that only the background density gradient, and not the full background density, appears in the equations (1.10-1.12). Since the background gradient is constant, periodic vertical boundary conditions are consistent with our equations.

The number of physical space grid points in each direction is given by n, which determines the size of the simulation and ultimately the attainable Re in DNS. The smallest wavenumber is defined by $k_0 = 2\pi/\mathcal{L}$ and higher wavenumbers are integer multiples of k_0,

where the integer values are between $-n/2+1$ and $n/2$. Therefore, the largest attainable wavenumber is

$$k_{max} = \frac{n\pi}{\mathcal{L}}. \tag{1.33}$$

As a result, the corresponding physical space grid spacing is

$$\Delta = \frac{\pi}{k_{max}}. \tag{1.34}$$

Using the fast Fourier transform, we can transform between physical and wavenumber space in the cost of $\mathcal{O}(n^3 \log n)$ (e.g. Pope, 2000). To avoid aliasing errors at large wavenumbers, we can use the two-thirds rule (e.g. Orszag, 1971; Durran, 2010), in which the largest third of the wavenumbers are filtered, and hence the effective grid spacing is increased to

$$\Delta_{eff} = \frac{3}{2}\frac{\pi}{k_{max}}. \tag{1.35}$$

It is worthwhile mentioning that the limitation of Fourier-based spectral methods is their applicability, as these methods are mainly appropriate for use in idealized cases with periodic boundary conditions.

The resolution requirements of DNS are what determine the computational costs. The domain size $\mathcal{L}$ (i.e. effectively the size of simulation) should be large enough to capture the energy-containing eddies. The grid spacing Δ also needs to be small enough to resolve the dissipation scale, i.e. $\Delta/L_d \lesssim 1$. Using the Taylor hypothesis, the number of grid points in each direction are directly related to the Re as follows (e.g. Pope, 2000)

$$\frac{\mathcal{L}}{L_d} \sim Re^{3/4}, \tag{1.36}$$

which demonstrates that increased Re increases the computational costs. Since the smallest-scale eddies are dependent on viscosity, much of this computational cost is devoted to resolving the dissipation range. As already mentioned, the dissipation range presents universal behaviours that are independent of large scale eddies. Overall, DNS is not an efficient computational approach for numerical simulations as Re increases.

1.3.2 LES

For large scales, the requirements of LES is similar to DNS, in which the domain size $\mathcal{L}$ should be large enough to resolve the energy-containing eddies. However by contrast with

DNS, LES does not need a grid spacing on the order of the Kolmogorov scale since this approach does not resolve the dissipation range. Asymptotically, LES resolves turbulent eddies in the limit of

$$Re \to \infty, \tag{1.37}$$

$$\nu \to 0, \tag{1.38}$$

therefore, it is applicable to neglect the molecular viscosity term in (1.10) and the diffusivity term in (1.12); instead, we need additional terms (usually turbulent-viscosity terms) to model the effects of unresolved small scale motions on large scale eddies. In LES, the largest resolved wavenumber in spectral methods is defined by the grid spacing Δ or the cutoff wavenumber k_c, which are related by

$$\Delta = \frac{\pi}{k_c}. \tag{1.39}$$

Similar to DNS, the effective grid spacing Δ_{eff} subjected to the two-thirds rule is written as

$$\Delta_{eff} = \frac{3\pi}{2k_c}. \tag{1.40}$$

In LES, the momentum equation (1.13) and the energy equation (1.15) are modified as follows

$$\frac{\partial \bar{\boldsymbol{u}}}{\partial t} + \bar{\boldsymbol{u}} \cdot \nabla \bar{\boldsymbol{u}} = -\nabla \bar{p} - \frac{1}{F^2} \bar{\rho} \boldsymbol{e}_z - \nabla \cdot \boldsymbol{\tau}, \tag{1.41}$$

$$\frac{\partial \bar{\rho}}{\partial t} + \bar{\boldsymbol{u}} \cdot \nabla \bar{\rho} - \bar{w} = -\nabla \cdot \boldsymbol{h}, \tag{1.42}$$

where the bar denotes filtered variables; $\boldsymbol{\tau}$ and $\boldsymbol{h}$ are the SGS momentum and density fluxes. Several approaches exist for parametrizing the SGS fluxes. In chapter 3, the SGS fluxes are represented using Smagorinsky (1963) and Kraichnan (1976) SGS models in the physical and wavenumber spaces, respectively. Chapter 4 considers the dynamic Smagorinsky model (e.g. Germano et al., 1991).

1.3.3 Hyperviscosity

A different approach to avoid resolving the molecular dissipation range is to replace the viscous term $\nu \nabla^2 \boldsymbol{u}(\boldsymbol{x}, t)$ in (1.10) with the hyperviscosity term

$$\nu_{hyp} (-1)^{m+1} \nabla^{2m} \boldsymbol{u}(\boldsymbol{x}, t), \tag{1.43}$$

where $m > 1$ (e.g. Herring & Métais, 1989; Waite & Bartello, 2004; Lindborg, 2006). This modification in wavenumber space corresponds to replacing $\nu k^2 \hat{\boldsymbol{u}}(\boldsymbol{k}, t)$ with

$$\nu_{hyp} k^{2m} \hat{\boldsymbol{u}}(\boldsymbol{k}, t). \tag{1.44}$$

A similar modification needs to be done for the density equation (1.12) as well. The advantage of hyperviscosity is that it is simple to implement in spectral methods, and it makes the dissipation range narrower, allowing for a longer inertial subrange than DNS at the same resolution. As a result, hyperviscosity modifies the definition of the Kolmogorov wavenumber, which needs to be resolved as in DNS, as follows

$$k_d = \left(\frac{\epsilon}{\nu_{hyp}^3} \right)^{1/(6m-2)}. \tag{1.45}$$

For $m = 1$, hyperviscosity dissipation yields the regular viscous dissipation.

1.4 Motivation

LES of stratified turbulence, where the Ozmidov scale is not necessarily resolved, is desired. This approach would allow us to study idealized atmospheric turbulence at large Re and with a reasonable computational costs. In addition, the anisotropic structures of stratified turbulence can be analyzed. SGS motions, in this situation, are anisotropic and therefore the common isotropic SGS models, such like Smagorinsky (1963) and Kraichnan (1976), might not be appropriate. Most previous numerical work on stratified turbulence has employed DNS (e.g. Riley & de Bruyn Kops, 2003; Brethouwer et al., 2007; Almalkie & de Bruyn Kops, 2012) or hyperviscosity (e.g. Herring & Métais, 1989; Waite & Bartello, 2004; Lindborg, 2006), which are in the intermediate range of Re and very expensive. Nevertheless, a few LES work have been done recently (e.g. Remmler & Hickel, 2012; Paoli et al., 2013), in which the applied SGS models are isotropic. However, there has been little discussion on the relation between the filter scale Δ and the dynamics of stratified turbulence. The typical Kolmogorov scale in the atmosphere and ocean is of order tens of millimeters (e.g. Waite, 2014), however, the realistic maximum domain size is of the order hundreds or thousands of kilometers (e.g. Riley & Lindborg, 2008). Therefore, DNS is not feasible in this situation and LES is desired. Also, current LES schemes that employ isotropic SGS models might not be proper for LES of stratified turbulence when L_o is not resolved.

The first step in this investigation of SGS motions in stratified turbulence is an *a priori* test using DNS results. The *a priori* testing refers to analyzing SGS motions using the actual DNS results. Next, we evaluate the performance of current isotropic SGS models in stratified turbulence. Finally, we measure the local up- and downscale kinetic and potential energy transfer in DNS to better understand dynamics around the Ozmidov and buoyancy scales. These three steps are the basis for future work, in which an anisotropic SGS model that captures the dynamical features of stratified turbulence is desired.

1.5 Thesis objectives

In this thesis, DNS and LES of stratified turbulence are studied. The objective of this work is to understand subgrid dynamics in stratified turbulence and how well they are parametrized by several standard SGS schemes, laying the groundwork for eventual development of improved models. The four main sections of this thesis are described below.

1.5.1 Effective eddy viscosity

In chapter 2, we study the actual behaviour of effective SGS motion in DNS of stratified turbulence. In this chapter, we perform DNS of decaying stratified turbulence for which all scales from large energy-containing down to the dissipation scales are resolved. The DNS results are analyzed using test filters to separate large and small scales. The test filter scales are larger than the Kolmogorov scale and similar to or smaller than the Ozmidov scale, to ensure that we have SGS eddies in the inertial subrange. This methodology helps us to study directly the effects of small eddies on larger scales. Comparing stratified cases with non-stratified simulations at different test filter scales provide comprehensive insights about the following questions:

- How does stratification affect interactions between large and small scales in turbulent flows?
- How different are effective SGS eddies for stratified turbulence when $\Delta \gtrsim L_o$ compared to when $\Delta \ll L_o$?
- When the test filter is applied separately in the horizontal and vertical directions, how different are the interactions between large and sub-test-filter scales (i.e. anisotropy)?
- How different are the horizontal and vertical eddy viscosities in stratified and unstratified turbulence?

1.5.2 Effects of buoyancy scale in LES of stratified turbulence

In chapter 3, LES of forced stratified turbulence using two common isotropic SGS models, i.e. the Smagorinsky (1963) and Kraichnan (1976) models, are studied where $\Delta > L_o$. The performance of isotropic SGS models, and the maximum resolution for which the dynamics of stratified turbulence are fully captured, are investigated. In this chapter, we try to answer the following questions:

- What is the maximum grid spacing for which the isotropic SGS models perform reasonably in stratified turbulence?
- What are the important parameters that the resolution criterion depends on?
- Which SGS model is less expensive and why?
- How different are the eddy dissipation spectra in the horizontal and vertical directions in stratified turbulence?

1.5.3 The dynamic Smagorinsky model for LES

Chapter 4 presents LES of forced stratified turbulence using the dynamic Smagorinsky model, which is a dynamical improvement on SGS modelling, and is presented by Germano et al. (1991); Lilly (1992). We apply the dynamic approach to the classical Smagorinsky model to improve the performance of LES in resolving dynamics of stratified turbulence while the total computational costs are decreased. These are some desirable inquires that we address in this chapter:

- Does the dynamic Smagorinsky model improves the performance of the regular Smagorinsky model in stratified turbulence in computational costs and resolving the dynamics of the flow?
- How does stratification affect the dynamic Smagorinsky coefficient c_s and its satatistics?
- What is the relationship between stratification, shear and c_s in stratified turbulence?

1.5.4 The dynamics of energy transfer in DNS of stratified turbulence

Chapter 5 includes a detailed analysis on the dynamics of up- and down-scale energy transfer for both physical and wavenumber spaces in DNS of stratified turbulence. The effective SGS kinetic and potential dissipation rate, effective SGS energy transfer spectra and effective turbulent Prandtl number are studied subject to different test cutoffs k_c. We address the following questions:

- Is backscatter important in stratified turbulence?
- How does the local energy transfer depend on the test cutoff k_c (i.e. investigation on the direction of energy transfer and self-similarity)?
- How sensitive are the dynamics of energy transfer to the flow parameters like resolution, buoyancy frequency and the buoyancy Reynolds number?

Chapter 6 includes the concluding remarks of this thesis along with the author's perspectives for future work. Chapters 2-4 are based on three published and submitted papers, and as a result they are written to be relatively self-contained.

Chapter 2

Effective eddy viscosity in stratified turbulence

This chapter presents an *a priori* testing on DNS results of decaying stratified turbulence by applying the test cutoff wavenumber k_c in the horizontal and vertical directions. It is shown that there is a non-local energy transfer in the horizontal direction that occurs at small vertical scales. Overall, anisotropic features, which are due to the presence of stratification, seem to be important when k_c is around or smaller than the Ozmidov wavenumber k_o.

This chapter is based on the published paper, Khani S. and M. L. Waite. Effective eddy viscosity in stratified turbulence. *J. Turbul.* 14(7): 49-70 2013,

2.1 Introduction

The nature of turbulence in the atmosphere and the ocean is characterized by very high Reynolds numbers. Moreover, in the atmospheric mesosphere and the oceanic sub-mesoscale range, turbulent flows are strongly affected by stable stratification, but only weakly affected by the Earth's rotation (Riley & Lelong, 2000). Thus, vertical motions are restrained by buoyancy forces and horizontal structures are elongated into anisotropic pancake-like vortices (Billant & Chomaz, 2000, 2001). Such flows can have Reynolds numbers of the order 10^8 or higher. Performing a direct numerical simulation (DNS) at such scales, therefore, requires that an enormous range of scales be resolved. Such resolution is not possible because of high computational memory and time costs. Large-eddy simulation (LES) is an alternative approach that removes the need to resolve any but the large-scale motions. The basic idea behind LES is to explicitly resolve large scales and to model the effects of small scales on large ones through subgrid-scale (SGS) models.

Recent advances in the understanding of geophysical turbulence have described the appearance of stratified turbulence when the buoyancy Reynolds number is sufficiently high and the horizontal Froude number is sufficiently low (Riley & de Bruyn Kops, 2003; Lindborg, 2006; Brethouwer et al., 2007; Riley & Lindborg, 2008). Under such conditions, the inertial subrange of stratified turbulence is divided into an anisotropic range at large scales and an isotropic range at small scales. The anisotropic and isotropic parts of the inertial subrange are separated by the Ozmidov (Lumely, 1964) wavenumber $k_o = (N^3/\epsilon)^{1/2}$, where ϵ is the kinetic energy dissipation rate and N is the buoyancy frequency. Generally, SGS models are used to model small-scale isotropic turbulence (Smagorinsky, 1963; Kraichnan, 1976; Chollet & Lesieur , 1981; Siegel & Domaradzki, 1994; Lesieur & Métais, 1996). In the inertial subrange of isotopic turbulence, the energy spectrum $E(k)$ is (Kolmogorov, 1941)

$$E(k) \sim \epsilon^{2/3} k^{-5/3}, \tag{2.1}$$

where $k = \sqrt{k_x^2 + k_y^2 + k_z^2}$ is the total wavenumber. However, stratified turbulence includes an additional anisotropic subrange because of stratification. According to the stratified turbulence hypothesis (Lindborg, 2006; Brethouwer et al., 2007), the energy spectrum in this range is proportional to different power laws in the horizontal and vertical wavenumbers

$$E(k_h) \sim \epsilon^{2/3} k_h^{-5/3} \qquad\qquad E(k_v) \sim N^2 k_v^{-3}, \tag{2.2}$$

where $k_h = \sqrt{k_x^2 + k_y^2}$ and $k_v = |k_z|$ respectively stand for the wavenumbers in the horizontal and vertical directions. Although simulations are largely consistent with these

predictions, the universality of $-5/3$ and -3 slopes is still under investigation (Waite & Bartello, 2004; Brethouwer et al., 2007; Waite, 2011; Almalkie & de Bruyn Kops, 2012; Waite, 2014). Isotropic SGS models do not seem to be the proper approach for modelling the effects of turbulent scales in the anisotropic part of the stratified turbulence inertial range. Since these models have been designed to represent the effects of small-scale motions in the isotropic subrange, it is important to study in detail the features of the anisotropic inertial subrange. One approach is to directly measure the effective spectral eddy viscosity using DNS results. This type of fundamental analysis has already been done for the Kolmogorov isotropic inertial subrange (as in e.g. Domaradzki et al., 1987, 1993), but it has not been studied for anisotropic stratified turbulence. The main aim of this paper is to study the dynamics of energy transfer in the anisotropic inertial subrange of stratified turbulence using the effective eddy viscosity point of view. A theoretical spectral eddy viscosity model for isotropic turbulence has been suggested by Kraichnan (1976), who considered an infinite inertial subrange. The Kraichnan eddy viscosity model includes two parts: a constant plateau at small wavenumbers, which represents the non-local energy transfer between SGS motions and large resolved scales, and a cusp near the cutoff wavenumber k_c, which accounts for the local energy transfer around the cutoff (Kraichnan, 1976; Bartello et al., 1996).

In this paper, we use DNS of stratified turbulence to explicitly measure the effective spectral eddy viscosity in the horizontal and vertical directions, following the Lindborg (2006) hypothesis of an anisotropic cascade from large to small horizontal scales. If the cascade to small scales is fundamentally anisotropic, the shapes of the effective eddy viscosity in the horizontal and vertical directions will provide insight into the nature of this energy transfer. We compare the results of this study to those of the original Kraichnan eddy viscosity model (Kraichnan, 1976) and also the results of Domaradzki et al. (1987, 1993) for unstratified turbulence, and evaluate how different they are. Our objective is to clarify the effects of stratification on SGS models. In Section 2.2 we review the literature on stratified flows and DNS and LES of stratified turbulence. This section also describes the governing equations of stratified flows as well as equations for measuring effective eddy viscosity. An overview of our numerical experiments and initial conditions is presented in Section 2.3. In Section 2.4, we present our simulation results and discuss the effects of stratification, Reynolds numbers, and the cutoff location. Finally, conclusions are given in Section 2.5.

2.2 Background

Strong stratification generates horizontal motions with large vertical shear, referred to as layered pancake structures (Gage, 1979; Lilly, 1983; Billant & Chomaz, 2001). Although Gage (1979) and Lilly (1983) proposed an inverse energy cascade (in analogy with two-dimensional turbulence) for these anisotropic three-dimensional structures, more recent results point to a downscale cascade Lindborg (e.g. 2006). The vertical scale (Billant & Chomaz, 2001; Waite & Bartello, 2004) of the pancake structures is u_{rms}/N, which yields a vertical Froude number of $O(1)$. This scaling for the vertical Froude number is the basis for the stratified turbulence hypothesis (Lindborg, 2006; Brethouwer et al., 2007) in which the inertial subrange has an anisotropic part at large scales in addition to the classical isotropic part at small scales.

Several studies have investigated numerical simulations of stratified turbulence, both DNS (Riley & de Bruyn Kops, 2003; Brethouwer et al., 2007; Almalkie & de Bruyn Kops, 2012; Waite, 2014) and LES (Siegel & Domaradzki, 1994; Kaltenbach, 1994; Carnevale et al., 2001; Remmler & Hickel, 2012). The main disadvantage of the DNS approach is its intrinsic limitation in achieving high Reynolds number flows. For example, in the DNS study by Almalkie & de Bruyn Kops (2012), in which the spatial resolution is very high, the maximum Reynolds number is $O(10^4)$. On the other hand, the LES of Siegel & Domaradzki (1994) and Carnevale et al. (2001), who used spatial and spectral eddy viscosity, respectively, neglected the effects of anisotropy in their SGS models. In addition, the implicit LES (ILES) approach (e.g. Remmler & Hickel, 2012) uses numerical diffusion to represent SGS, and thus very sensitive to the numerical scheme (Domaradzki & Radhakrishnan, 2005). Therefore, there is a real need for better understanding of SGS motions of stratified flows.

The non-dimensionalized Navier-Stokes equations under the Boussinesq approximation are

$$\frac{\partial \boldsymbol{u}}{\partial t} + \boldsymbol{u}\cdot\nabla\boldsymbol{u} = -\nabla p - \frac{1}{{Fr_\ell}^2}\rho\boldsymbol{e}_z + \frac{1}{Re_\ell}\nabla^2\boldsymbol{u}, \tag{2.3}$$

$$\nabla\cdot\boldsymbol{u} = 0, \tag{2.4}$$

$$\frac{\partial \rho}{\partial t} + \boldsymbol{u}\cdot\nabla\rho - w = \frac{1}{Re_\ell Pr}\nabla^2\rho, \tag{2.5}$$

where $\boldsymbol{u}$ is the velocity vector, and ρ and p are the density and pressure fluctuations from their ambient values. The initial Reynolds number Re_ℓ, Froude number Fr_ℓ, and Prandtl

number Pr are defined as

$$Re_\ell = \frac{u\ell}{\nu}, \tag{2.6}$$

$$Fr_\ell = \frac{u}{N\ell}, \tag{2.7}$$

$$Pr = \frac{\nu}{D}, \tag{2.8}$$

where u and ℓ are the initial velocity- and length-scales, respectively, ν is the molecular viscosity, and D is the mass diffusivity. In this work, we take $Pr = 1$ and assume constant N. This latter assumption is common in idealized studies of stratified turbulence (Riley & de Bruyn Kops, 2003; Waite & Bartello, 2004; Brethouwer et al., 2007; Riley & Lindborg, 2008; Waite, 2011, 2014).

Assuming periodic boundary conditions, a flow variable $f(\boldsymbol{x}, t)$ can be expanded in a Fourier series as

$$f(\boldsymbol{x}, t) = \sum_{\boldsymbol{k}} \hat{f}(\boldsymbol{k}, t) e^{i\boldsymbol{k}\cdot\boldsymbol{x}}, \tag{2.9}$$

where $\hat{f}(\boldsymbol{k}, t)$ is the Fourier coefficient of f, and the sum is up to an isotropic cutoff $|\boldsymbol{k}| < k_{max}$. In DNS, k_{max} is set to be around the Kolmogorov wavenumber

$$k_d = (\frac{\epsilon}{\nu^3})^{\frac{1}{4}}, \tag{2.10}$$

which ensures that the dissipation is resolved. Our k_{max}/k_d is always greater than 0.5, which, following Moin & Mahesh (1998), means that most of the dissipation is resolved. The equations of motion (2.31-2.5) can be re-written as

$$(\frac{\partial}{\partial t} + \frac{k^2}{Re_\ell})\hat{u}_j(\boldsymbol{k}, t) + \frac{1}{{Fr_\ell}^2}\hat{\rho}(\boldsymbol{k}, t)\boldsymbol{e}_z = -ik_m P_{jr}(\boldsymbol{k}) \sum_{\boldsymbol{p}+\boldsymbol{q}=\boldsymbol{k}} \hat{u}_r(\boldsymbol{p}, t)\hat{u}_m(\boldsymbol{q}, t), \tag{2.11}$$

$$k_i\hat{u}_i(\boldsymbol{k}, t) = 0, \tag{2.12}$$

$$(\frac{\partial}{\partial t} + \frac{k^2}{Re_\ell Pr})\hat{\rho}(\boldsymbol{k}, t) - \hat{w}(\boldsymbol{k}, t) = -ik_m \sum_{\boldsymbol{p}+\boldsymbol{q}=\boldsymbol{k}} \hat{u}_m(\boldsymbol{p}, t)\hat{\rho}(\boldsymbol{q}, t), \tag{2.13}$$

where the projection tensor $P_{ij}(\boldsymbol{k}) = \delta_{ij} - k_i k_j/k^2$ is used to eliminate the pressure term (Rose & Sulem, 1978). If we define a test cutoff wavenumber k_c, we can express the

interactions between wavevectors with $|\boldsymbol{k}| > k_c$ and those with $|\boldsymbol{k}| \leq k_c$. Consider the non-linear terms on the right-hand side of equations (2.11) and (2.13):

$$F_j(\boldsymbol{k},t) = -ik_m P_{jr}(\boldsymbol{k}) \sum_{\boldsymbol{p}+\boldsymbol{q}=\boldsymbol{k}} \hat{u}_r(\boldsymbol{p},t)\hat{u}_m(\boldsymbol{q},t), \tag{2.14}$$

$$J(\boldsymbol{k},t) = -ik_m \sum_{\boldsymbol{p}+\boldsymbol{q}=\boldsymbol{k}} \hat{u}_m(\boldsymbol{p},t)\hat{\rho}(\boldsymbol{q},t). \tag{2.15}$$

The corresponding nonlinear terms in the kinetic and potential energy equations (see Appendix A), T_k and T_p, can be obtained by multiplying equations (2.14) and (2.15) by $\hat{u}_j^*$ and $(1/{Fr_\ell}^2)\hat{\rho}^*$, and adding the complex conjugates (denoted by $*$) yielding (Lindborg, 2006; Rose & Sulem, 1978; Pope, 2000):

$$T_k(\boldsymbol{k},t) = -\frac{i}{2}k_m P_{jr} \sum_{\boldsymbol{p}+\boldsymbol{q}=\boldsymbol{k}} \{ \quad \hat{u}_j^*(\boldsymbol{k},t)\hat{u}_r(\boldsymbol{p},t)\hat{u}_m(\boldsymbol{q},t) + \quad \hat{u}_j(\boldsymbol{k},t)\hat{u}_r^*(\boldsymbol{p},t)\hat{u}_m^*(\boldsymbol{q},t)\}, \tag{2.16}$$

$$T_p(\boldsymbol{k},t) = -\frac{i}{2{Fr_\ell}^2}k_m \sum_{\boldsymbol{p}+\boldsymbol{q}=\boldsymbol{k}} \{ \quad \hat{\rho}^*(\boldsymbol{k},t)\hat{u}_m(\boldsymbol{p},t)\hat{\rho}(\boldsymbol{q},t) + \quad \hat{\rho}(\boldsymbol{k},t)\hat{u}_m^*(\boldsymbol{p},t)\hat{\rho}^*(\boldsymbol{q},t)\}. \tag{2.17}$$

Based on the cutoff k_c, we can decompose T_k and T_p into $\overline{T_k}$ and $\overline{T_p}$, in which the sums in equations (2.16) and (2.17) are restricted to $\boldsymbol{p}$ and $\boldsymbol{q}$ with $|\boldsymbol{p}|$, $|\boldsymbol{q}| < k_c$; and T_k^s and T_p^s, in which at least one of $|\boldsymbol{p}|$ or $|\boldsymbol{q}|$ is above the cutoff k_c. The quantities T_k^s and T_p^s represent energy transfer into $\boldsymbol{k}$ from interactions with wavenumbers above k_c. The spectral eddy viscosity approach models T_k^s and T_p^s by (Kraichnan, 1976; Domaradzki et al., 1987; Bartello et al., 1996; Pope, 2000)

$$T_k^s(\boldsymbol{k},t) = -2\nu_e(\boldsymbol{k},t)k^2E(\boldsymbol{k},t), \tag{2.18}$$

$$T_p^s(\boldsymbol{k},t) = \frac{T_k^s(\boldsymbol{k},t)}{Pr_t} = -2\frac{\nu_e(\boldsymbol{k},t)}{Pr_t}k^2E(\boldsymbol{k},t), \tag{2.19}$$

where $\nu_e(\boldsymbol{k},t)$ is the spectral eddy viscosity coefficient, $E(\boldsymbol{k},t) = \frac{1}{2}\hat{u}_j(\boldsymbol{k},t)\hat{u}_j^*(\boldsymbol{k},t)$ is the kinetic energy in wavevector $\boldsymbol{k}$, and Pr_t is the turbulent Prandtl number (usually assumed to be constant e.g. Lesieur, 1990; Batchelor et al., 1992; Siegel & Domaradzki, 1994). The eddy viscosity at wavenumber $\boldsymbol{k}$ can therefore be defined as

$$\nu_e(\boldsymbol{k},t) = -\frac{T_k^s(\boldsymbol{k},t)}{2k^2E(\boldsymbol{k},t)}. \tag{2.20}$$

Assuming an isotropic eddy viscosity, $T_k^s(\boldsymbol{k},t)$ and $E(\boldsymbol{k},t)$ in (2.20) can be integrated over spheres of radius k to get the spherical eddy viscosity (following the Pope, 2000, notation) as (Domaradzki et al., 1987)

$$\nu_e(k|k_c,t) = -\frac{T_k^s(k,t)}{2k^2E(k,t)}, \tag{2.21}$$

where $T_k^s(k,t)$ is the integrated energy transfer between the cutoff-resolved motions and modes with $k > k_c$, and $E(k,t)$ is the integrated energy spectrum. Here, cutoff-resolved refers to scales with wavenumbers below the test cutoff k_c. This approach was introduced by Domaradzki et al. (1987) for measuring effective eddy viscosity in DNS of isotropic turbulence. More recently, Domaradzki & Radhakrishnan (2005) measured the effective eddy viscosity in an implicit model of decaying turbulence. They found that without careful choice of the numerical scheme, ILES was unlikely to successfully represent SGS features.

Based on the Lindborg (2006) stratified turbulence hypothesis, in which there is an anisotropic cascade from large to small horizontal scales, it seems appropriate to modify the above approach to apply a test cutoff k_c in the horizontal direction. In this case, $T_k^s(\boldsymbol{k},t)$ in (2.20) changes to $T_k^{s,h}(\boldsymbol{k},t)$, which refers to the energy transfer between modes with $k_h < k_c$, i.e. horizontal cutoff-resolved, and modes with $k_h > k_c$. In this situation, we assume axisymmetric horizontal eddy viscosity, and integrate $T_k^{s,h}(\boldsymbol{k},t)$ and $E(\boldsymbol{k},t)$ over shells of constants k_h to find the horizontal eddy viscosity. In addition, we can also apply the test cutoff k_c in the vertical direction to define $T_k^{s,v}(\boldsymbol{k},t)$ and integrate over k_x and k_y to compute a vertical eddy viscosity. In summary, to measure the horizontal and vertical eddy viscosity, equation (2.21) can be used if altered somewhat:

$$\nu_e^h(k_h|k_c,t) = -\frac{T_k^{s,h}(k_h,t)}{2k_h^2E(k_h,t)}, \tag{2.22}$$

$$\nu_e^v(k_v|k_c,t) = -\frac{T_k^{s,v}(k_v,t)}{2k_v^2E(k_v,t)}. \tag{2.23}$$

where $T_k^{s,h}(k_h,t)$ and $T_k^{s,v}(k_v,t)$ are the integrated energy transfer between cutoff-resolved motions and modes with $k_h > k_c$ and $k_v > k_c$, respectively; where k_c is applied accordingly in the horizontal and vertical directions. Moreover, $E(k_h,t)$ and $E(k_v,t)$ are the integrated energy spectrum in the horizontal and vertical directions, respectively.

The distinctions between the horizontal, vertical, and spherical eddy viscosities are important. These eddy viscosities are categorized based on directions in which the test cutoff is applied. When we apply the cutoff k_c in the horizontal direction, for example, we filter at the horizontal cutoff-resolved resolution π/k_c. However, the vertical resolution remains unchanged (i.e. $\Delta z \sim \pi/k_d$). Therefore, by applying the test cutoff k_c in a specific direction, the effective resolution in that direction decreases. As a result, we have a specific eddy viscosity based on the definition of the cutoff k_c in a specific direction. In summary, the kinetic energy equation is affected by these three definitions of the test cutoff k_c in the spherical, horizontal, and vertical directions and are, respectively

$$\frac{\partial E(k,t)}{\partial t} + B(k,t) = \overline{T_k}(k,t) - 2\nu_e(k|k_c,t)k^2E(k,t), \tag{2.24}$$

$$\frac{\partial E(k_h,t)}{\partial t} + B(k_h,t) = \overline{T_k}^h(k_h,t) - 2\nu_e^h(k_h|k_c,t)k_h^2E(k_h,t), \tag{2.25}$$

$$\frac{\partial E(k_v,t)}{\partial t} + B(k_v,t) = \overline{T_k}^v(k_v,t) - 2\nu_e^v(k_v|k_c,t)k_v^2E(k_v,t), \tag{2.26}$$

where the molecular dissipation is neglected for clarity, and

$$B(\boldsymbol{k},t) = \frac{1}{2Fr_\ell^2}\{\hat{\rho}(\boldsymbol{k},t)\hat{w}^*(\boldsymbol{k},t) + \hat{\rho}^*(\boldsymbol{k},t)\hat{w}(\boldsymbol{k},t)\}, \tag{2.27}$$

is the buoyancy flux, the spherical, horizontal, and vertical wavenumber spectra of which are defined as above.

Applying the test cutoff k_c in different directions (i.e. the horizontal, vertical, and spherical) results in different influences over the triad interactions of $\boldsymbol{p}$, $\boldsymbol{q}$, and $\boldsymbol{k}$ in (2.16-2.17). For example, compare the effect of defining the test cutoff in the horizontal direction to that in the spherical one. Applying the cutoff in the horizontal direction, modes with $k_h < k_c$ are retained, but there is no restriction on k_v or k. However, if we apply the cutoff k_c in the spherical direction, all large-scale modes with $k < k_c$ are included; this restriction involves both the horizontal and vertical scales. Hence if, for example, there is an energy exchange between large and small horizontal scales at large vertical wavenumbers, the horizontal eddy viscosity will measure this energy transfer but the spherical eddy viscosity will not. In this case, there is a non-local energy transfer in the horizontal direction, which

occurs at large vertical wavenumbers. This energy transfer will therefore lead to a non-local horizontal eddy viscosity but no spherical eddy viscosity. This behaviour could lead to confusion for unstratified turbulence where the underlying cascade is isotropic. However, given the overwhelming evidence for an anisotropic cascade in stratified turbulence (e.g. Riley & de Bruyn Kops, 2003; Waite & Bartello, 2004; Lindborg, 2006; Hebert & de Bruyn Kops, 2006b; Brethouwer et al., 2007), the separate consideration of horizontal and vertical eddy viscosity is meaningful and important.

Stratification is characterized in our simulations by two Froude numbers: the initial Froude number, as defined in (2.7); and a time-dependent horizontal Froude number

$$Fr_h = \frac{u_{rms}}{NL_h}, \tag{2.28}$$

where u_{rms} is the root-mean-square velocity and the horizontal scale $L_h \equiv [u_{rms}]^3/\epsilon$ is defined using the Taylor hypothesis (Brethouwer et al., 2007). We will evaluate this approximation below in Section 2.4. In the same manner, we define the buoyancy Reynolds number (Brethouwer et al., 2007) as

$$Re_b = \frac{\epsilon}{\nu N^2}. \tag{2.29}$$

When the horizontal Froude number Fr_h is sufficiently small (i.e. when flows are strongly stratified), the buoyancy Reynolds number plays a similar role to the Reynolds number in non-stratified flows. In fact, the buoyancy Reynolds number sets the magnitude of the vertical viscous term in the Boussinesq equations (Brethouwer et al., 2007). Thus, a flow with a smaller horizontal Froude number (stronger stratification) needs larger Reynolds numbers to ensure turbulence. There are a variety of other Froude numbers defined in the literature; e.g. Riley & de Bruyn Kops (2003) used the periodic buoyancy frequency to define the Froude number $2\pi u/N\ell$ which differs from (2.7) by a factor 2π; the associated buoyancy Reynolds number differs by a significant factor $(2\pi)^2$.

2.3 Methodology

In this work, DNS of stratified turbulence are employed to measure the effective eddy viscosity. An idealized decaying stratified turbulence test case has been considered, following the DNS of Riley & de Bruyn Kops (2003). The initial condition consists of Taylor-Green

Table 2.1: List of numerical simulations for DNS.

Identifier	Fr_ℓ	Re_ℓ	n	k_{max}/k_d
$F0.6$	0.64	6400	768	$0.73 - 0.94$
$F0.3$	0.32	6400	768	$0.69 - 0.84$
UNST	∞	6400	768	$0.5 - 1.25$
$F0.6R$	0.64	800	256	$1.21 - 1.41$
k_c	10	20	40	80

(TG) vortices in a periodic cubic domain of size $L = 4\pi$, i.e. two TG wavelengths. The TG vortices are designed to have horizontal structures with vertical variations:

$$\boldsymbol{u}(\boldsymbol{x}, 0) = \cos(z)[\cos(x)\sin(y), -\sin(x)\cos(y), 0]. \tag{2.30}$$

Low-level noise of approximately 10% of the initial energy is also added to the initial condition (Riley & de Bruyn Kops, 2003). In our study, the random noise is distributed isotropically, and noise is restricted to wavenumbers with $k_h \leq 7/2$ and $|k_z| \leq 7/2$. Since the non-dimensional domain is 4π, wavenumbers spacing is $1/2$.

The spectral transform method has been used to solve the governing equation with n grid points in the x, y, and z directions. To eliminate aliasing errors, the two-thirds rule (e.g. Durran, 2010) with spherical wavenumber truncation is applied, yielding an effective grid spacing of $\Delta x = 1.5L/n$. The third-order Adams-Bashforth scheme is adopted for time-stepping of the nonlinear and buoyancy terms; the implicit trapezoidal method is used for the diffusion terms. Simulations with two different initial Reynolds numbers $Re_\ell = 6400$ and 800, and three initial Froude numbers $Fr_\ell = 0.32$, 0.64, and ∞ are considered. Finally, four values of $k_c = 10$, 20, 40, 80 are employed as test cutoffs to analyze the effective eddy viscosity. Table 2.1 shows a list of the parameters and corresponding identifiers used in this study.

2.4 Results and Discussion

2.4.1 Overview of simulations

Figure 2.1 illustrates the general evolution of the energy, dissipation rates, kinetic energy spectra, and kinetic energy dissipation spectra for two stratified and one non-stratified cases with the same initial $Re_\ell = 6400$, and one stratified case with initial $Re_\ell = 800$. Figure 2.1(a) shows total (kinetic plus potential) energy versus time. The non-stratified case is much less energetic than the stratified case for $t \gtrsim 10$. This behaviour is also evident in figure 2.1(b), where the total dissipation rate is much higher in the non-stratified turbulence at early times (as in e.g. Domaradzki et al., 1993; Remmler & Hickel, 2012). Figures 2.1(c,d) show respectively the spherical energy spectrum $E(k)$ and the kinetic energy dissipation spectrum $D(k) = 2\nu k^2 E(k)$ averaged over a time range around the maximum dissipation rates of the stratified and non-stratified cases ($15 \leq t \leq 20$ for the stratified cases with $Fr_\ell = 0.64$; $20 \leq t \leq 25$ for the stratified case with $Fr_\ell = 0.32$; and $10 \leq t \leq 15$ for the non-stratified case). Table 2.1 shows the range of k_{max}/k_d for all simulations. Since we are interested in results with large Reynolds and buoyancy Reynolds numbers, time averages are computed around the time of maximum ϵ. At these times, the Kolmogorov scale is smallest and hence closest to the grid scale, and k_{max}/k_d reaches the minimum value shown in table 2.1, which is still consistent with DNS (Moin & Mahesh, 1998). This resolution of the Kolmogorov scale is similar to other recent DNS studies of stratified turbulence (e.g. Riley & de Bruyn Kops, 2003; Hebert & de Bruyn Kops, 2006a,b; Bartello & Tobias, 2013). It is also noteworthy that the large-scale energy increases with decreasing initial Froude number (from $Fr_\ell = \infty$ to 0.64 to 0.32), regardless of the value of the initial Reynolds number (figures 2.1c,d).

For the non-stratified case, the approximate time for the onset of turbulence is $t \approx 10$, when the dissipation rate is maximum. However, the time of maximum $\epsilon_{tot} = \epsilon + \epsilon_p$, where ϵ_p is the potential energy dissipation, is postponed in the stratified flows. This behaviour can also be seen in figure 2.1(a) where the total energy is almost constant for $Fr_\ell = 0.64$ up to $t \approx 15$, and for $Fr_\ell = 0.32$ up to $t \approx 20$. Decreasing the initial Froude number from 0.64 to 0.32, at fixed Re_ℓ, may suppress the onset of turbulence as it causes Re_b to fall to around 1 (see below). Hence, in the stratified case, higher Reynolds numbers may be necessary to accelerate the onset of turbulence as in the non-stratified case. The maximum ϵ_{tot} occurs at $t = 15$ for $Fr_\ell = 0.64$ and $t = 21$ for $Fr_\ell = 0.32$. This behaviour demonstrates a delay in the commencement of turbulence caused by decreasing the initial Froude number (Riley & de Bruyn Kops, 2003; Hebert & de Bruyn Kops, 2006a) (and hence the horizontal Froude number as well). The vertical arrows in figures 2.1(c,d) indicate values of the test cutoff

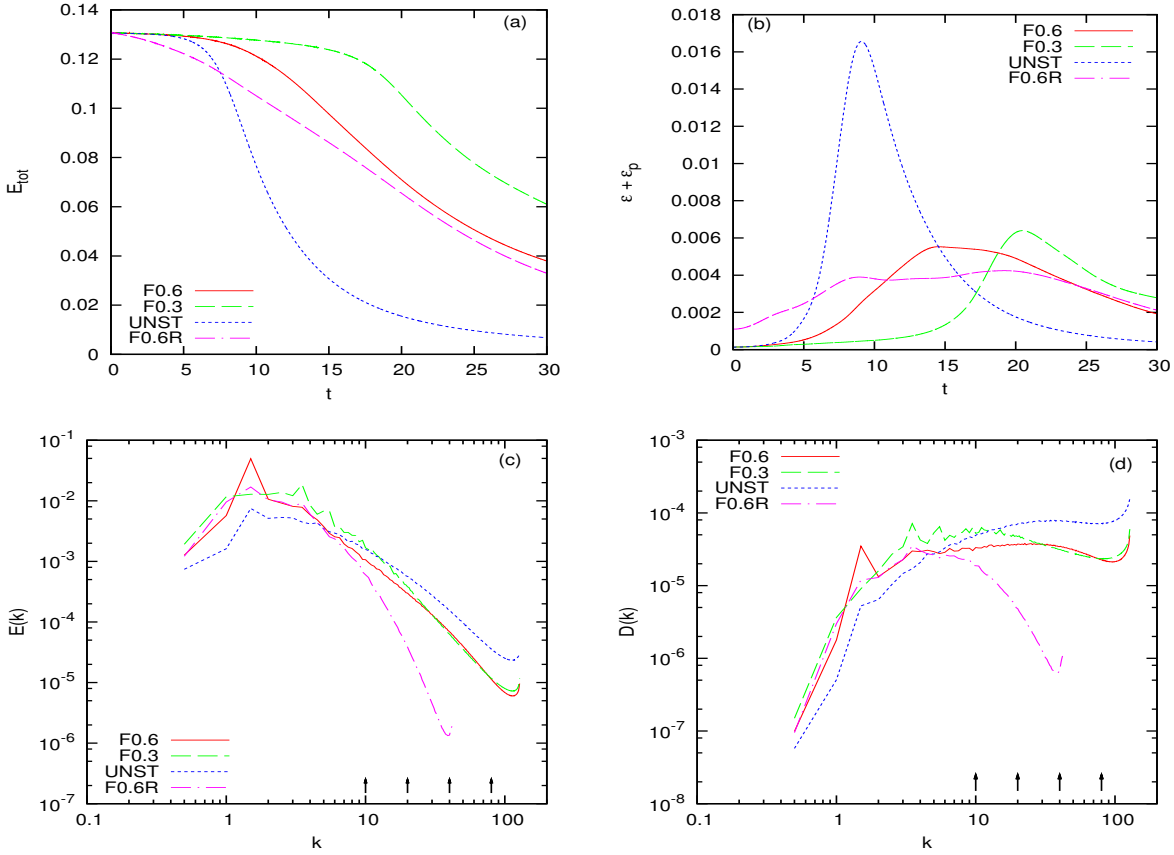

Figure 2.1: (a) Total energy, (b) total dissipation rate, (c) time-averaged kinetic energy spectra, and (d) time-averaged dissipation spectra. Arrows indicate values of the different test cutoffs k_c, which are presented in Section 2.4.2. See table 2.1 for the identifiers.

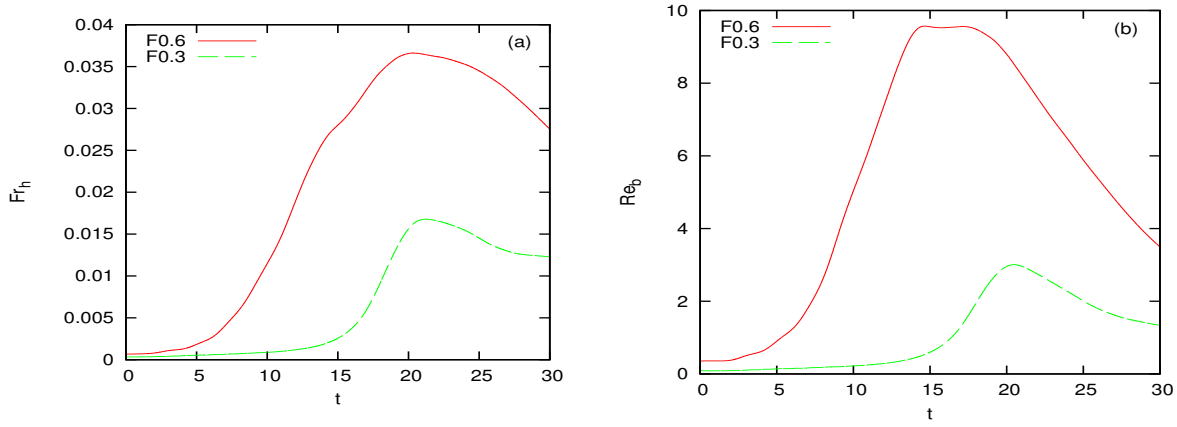

Figure 2.2: Time series of (a) horizontal Froude number and (b) buoyancy Reynolds number for the two stratified simulations with $Re_\ell = 6400$. Froude and buoyancy Reynolds numbers are computed with a horizontal length scale obtained from Taylor's hypothesis, which may not be valid at early times.

k_c, which will be addressed in Section 2.4.2.

Figure 2.2 shows the time series of the horizontal Froude number and the buoyancy Reynolds number for two different initial Froude numbers. Recall that the time-dependent L_h is defined using Taylor's hypothesis, which is not expected to be valid when the flow is not turbulent. As a result, figure 2.2 does not necessarily yield reasonable results before the commencement of turbulence. Therefore, for $Fr_\ell = 0.64$, figure 2.2 is expected to be valid when $t \gtrsim 15$. Similarly, for $Fr_\ell = 0.32$, it is valid when $t \gtrsim 20$. As seen in figure 2.2(a), the horizontal Froude numbers are relatively small and fairly close to the Lindborg (2006) threshold of value 0.02 for stratified turbulence. (Since Riley & de Bruyn Kops, 2003, defined their Froude numbers based on the periodic buoyancy frequency, the Froude numbers in figure 2.2(a) should be multiplied by 2π to compare their results). Figure 2.2(b) shows that the values of the buoyancy Reynolds number are $O(1)$ for $Fr_\ell = 0.32$ and $O(10)$ for $Fr_\ell = 0.64$, suggesting that these flows are (marginally) strongly stratified turbulence. For case $Fr_\ell = 0.32$, the buoyancy Reynolds number is $Re_b \leq 4$, and so the vertical viscous shear may be significant (Brethouwer et al., 2007). In the literature, simulations with $Fr_\ell = 0.64$ and $Fr_\ell = 0.32$, and $Re_\ell = 6400$ have been reported to be inside the strongly stratified turbulence regime (Brethouwer et al., 2007; Hebert & de Bruyn Kops, 2006a).

Time series of the horizontal and vertical length-scales are shown in figure 2.3. These

length-scales are calculated using the horizontal and vertical energy spectra as follows (Lindborg, 2006):

$$l_h = \frac{2\pi \int_0^\infty E(k_h)\,\mathrm{d}k_h}{\int_0^\infty k_h E(k_h)\,\mathrm{d}k_h}, \qquad l_v = \frac{2\pi \int_0^\infty E(k_v)\,\mathrm{d}k_v}{\int_0^\infty k_v E(k_v)\,\mathrm{d}k_v}. \tag{2.31}$$

In the unstratified case, l_h decreases significantly over $0 \leq t \leq 10$. Increased stratification leads to a much smaller decrease (or even slight increase) in l_h, so the horizontal length-scale almost retains its original length. However, the vertical scale decreases significantly in all cases. For example, the $Fr_\ell = 0.32$ case retains its initial horizontal length-scale up to $t = 15$, at which time the vertical length-scale is about 30% of its initial value (see figure 3.7b). After the onset of turbulence, the buoyancy Reynolds number decreases, and so the simulation transitions from marginally viscous (i.e. $Re_b \gtrsim 1$) to viscosity-affected (i.e. $Re_b \lesssim 1$) stratified turbulence. According to figure 3.7(a), the horizontal scales increase as Re_b decreases.

There are four interesting results in figure 2.3: first of all, as seen in figure 2.3(c), using the Taylor hypothesis to estimate l_h can be a good approximation for the non-stratified case since l_h/L_h is almost constant (≈ 0.6) after the onset of turbulence. For stratified turbulence, on the other hand, $l_h/L_h \approx 0.4$ at the time of maximum ϵ_{tot} and increases with time. A similar trend for l_h for stratified turbulence has been observed in other experimental (Praud et al., 2005) and numerical (Hebert & de Bruyn Kops, 2006b) studies. Secondly, the vertical length-scales for $Fr_\ell = 0.64$ and $Fr_\ell = 0.32$ are shown in figure 2.3(d), scaled by the buoyancy scale $L_b = 2\pi u_{rms}/N$. The factor 2π is included, following (Waite, 2011, 2014), because it is the buoyancy wavenumber $k_b = N/u_{rms}$ that appears in applications (e.g. Billant & Chomaz, 2000). After turbulence commences (i.e. $t \gtrsim 20$), $l_v \sim L_b$ is a fairly good approximation. It is found that l_v is larger than L_b for the case with smaller Re_b, in agreement with the finding that l_v is set by viscosity at small Re_b (Hebert & de Bruyn Kops, 2006a; Brethouwer et al., 2007). Moreover, figures 3.7(a) and 3.7(b) also demonstrate an approximate equality of l_h and l_v for the non-stratified case. And finally, for the simulation with $Fr_\ell = 0.64$ and $Re_\ell = 800$, we can see an almost constant horizontal length-scale throughout the simulation (figure 2.3a) and hence a fairly weak agreement with Taylor's hypothesis (figure 2.3c). This behaviour is consistent with small Re_b in which the stratified flow seems to not be very turbulent.

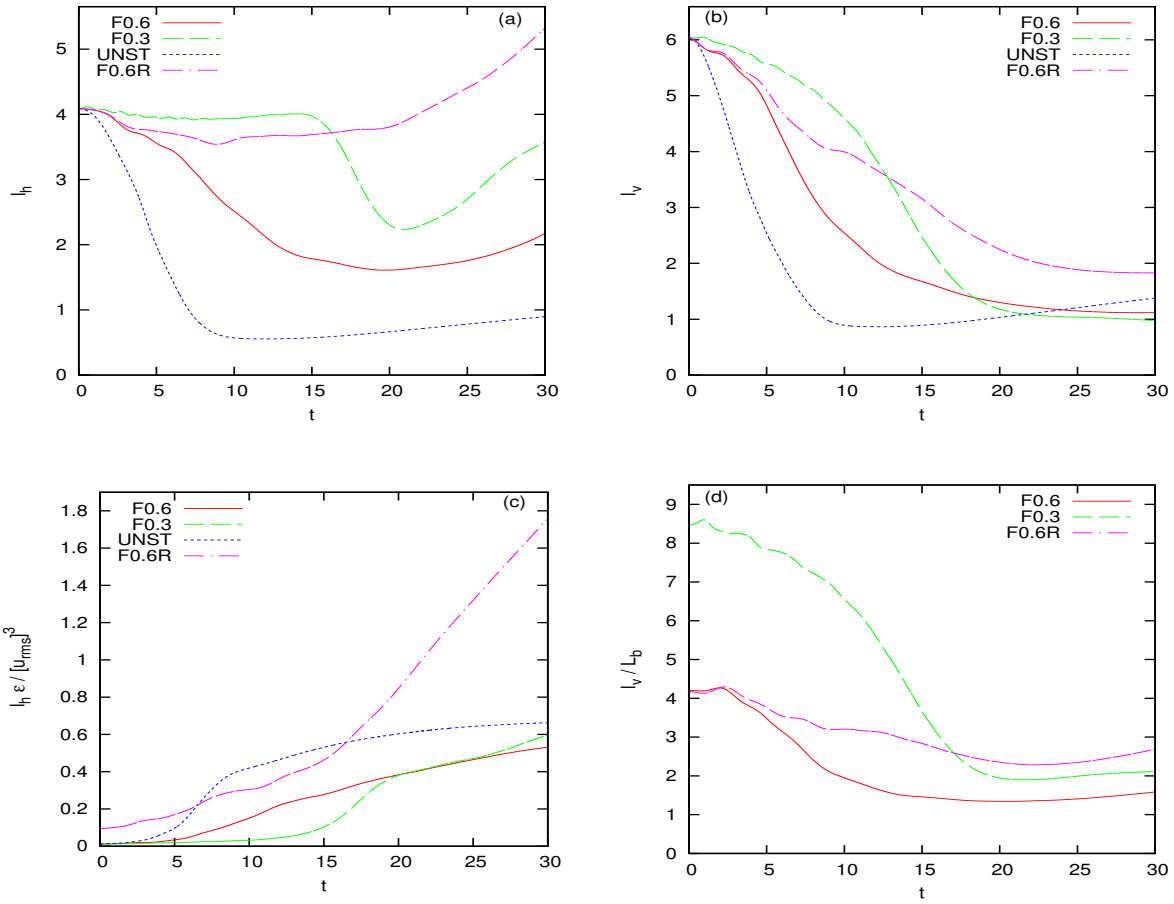

Figure 2.3: Time series of (a) the horizontal length-scale, (b) the vertical length-scale, (c) the horizontal length-scale scaled using the Taylor hypothesis, and (d) the vertical length-scale scaled by the buoyancy scale L_b.

2.4.2 Effective eddy viscosity

This section describes the results of directly measuring the effective eddy viscosity in the horizontal, vertical, and spherical directions. Effective eddy viscosity represents the effects of smaller-scale motions on eddies with wavenumbers below k_c. Four different cutoffs k_c have been employed in each of the horizontal, vertical, and spherical directions to analyze the DNS results. The effective eddy viscosities have been averaged over a time range around the maximum dissipation rates (as in figures 2.1c,d). Based on the Kraichnan eddy viscosity model (Kraichnan, 1976), the effective cutoff k_c should be inside the inertial subrange. According to figure 2.1(d), $k_c = 80$ is inside the dissipation range. Therefore, we expect the measured eddy viscosity in this case to be small. All figures in this section are plotted in terms of $k^+ = k/k_c$ or $k_h^+ = k_h/k_c$ or $k_v^+ = k_v/k_c$. Moreover, the values of eddy viscosities in each figure (except figure 2.8) have been normalized by the value of the corresponding molecular viscosity to show their effectiveness. The values of the SGS energy transfer in figures 2.4(c,d) are normalized by those of the spherical SGS energy transfer at the test cutoff $k_c = 40$.

Stratification and effective eddy viscosity in different directions

First, we examine the $Fr_\ell = 0.64$ case when the cutoff wavenumber $k_c = 40$ is around the Ozmidov wavenumber $k_o \approx 35$. The unstratified case is also considered for comparison. Figure 2.4(a,b) show the non-stratified and stratified eddy viscosities, along with the Kraichnan theoretical eddy viscosity model (Kraichnan, 1976). The SGS energy transfer T_k^s, $T_k^{s,h}$, and $T_k^{s,v}$ are shown in figures 2.4(c,d). According to figure 2.4(a), the horizontal, vertical, and spherical eddy viscosities are very similar for non-stratified turbulence when $k^+ \gtrsim 0.1$. This behaviour is a sign of isotropic unstratified turbulence in which, for $k_c = 40$, the effective eddy viscosities are independent of direction. There are differences in the spherical, horizontal, and vertical eddy viscosities at large scales (i.e. $k^+ \lesssim 0.1$), which is to be expected given the anisotropy of the initial TG vortices. The slightly negative values of the effective eddy viscosity for small k^+ have also been previously reported (Domaradzki et al., 1987; Métais & Lesieur, 1992; Domaradzki et al., 1993; Domaradzki & Radhakrishnan, 2005). Large positive values of vertical eddy viscosity in figure 2.4(a) when $k_v^+ \lesssim 0.1$ demonstrates a non-local energy transfer from large to small vertical scales (cf. $T_k^{s,v}$ in figure 2.4c). It is important to note that for measuring the vertical eddy viscosity, we did not apply a restriction on the horizontal wavenumbers. Since the energy transfer in the non-stratified case is likely isotropic, the non-local energy transfer in the vertical direction may result from a local spherical transfer around k_c. The same conclusions hold for the large positive horizontal eddy viscosity as well.

In the stratified case, the horizontal eddy viscosity exhibits a very different behaviour: it has a positive plateau for $0.05 \lesssim k_h^+ \lesssim 0.8$ and a sharp cusp near k_c (figure 2.4b). This behaviour is also clear in figure 2.4(d), in which for $0.05 \lesssim k_h^+ \lesssim 0.8$, the horizontal SGS energy transfer $T_k^{s,h}$ has an almost constant plateau, which has a value of 23% of the local horizontal SGS energy transfer at the cutoff k_c. However, ν_e is smaller overall than in the unstratified case. The presence of stratification results in a considerable difference between ν_e^h and ν_e^v: it increases the non-local energy transfer and effective eddy viscosity in the horizontal direction. A peak around $k_h^+ = 0.05$ is seen in the horizontal eddy viscosity, which is due to the effects of the initial conditions. Moreover, when $k_v^+ \lesssim 0.02$, the non-local vertical energy transfer is larger than the non-local horizontal energy transfer (figure 2.4d). This behaviour suggests that there is a stronger energy transfer between large vertical scales and small vertical ones, which is consistent with the development of layers and small-scale turbulence with vertical wavenumbers above the cutoff k_c.

In summary, figures 2.4(b,d) display two phenomena for $k^+ \ll 1$ in the stratified case. In the vertical, there is a transfer of energy from large to small scales. This large non-local energy transfer, which yields a large vertical eddy viscosity at small k_v, which is shown through the vertical eddy viscosity, is in agreement with the layering hypothesis of stratified turbulence (e.g. Billant & Chomaz, 2001). The other phenomenon is the presence of a positive plateau for $0.05 \lesssim k_h^+ \lesssim 0.8$ in the horizontal eddy viscosity and the horizontal SGS energy transfer $T_k^{s,h}$. Such non-local energy exchange between large and small horizontal scales is reminiscent of recent results in forced stratified turbulence (Waite, 2011) and the breakdown of columnar vortices (Augier et al., 2012; Deloncle et al., 2008).

As mentioned above, the shape of the horizontal eddy viscosity in the stratified case shows a non-local energy transfer between large and small horizontal scales. All vertical scales are included in the calculation of $T_k^{s,h}$ and ν_e^h, so it is important to know if there is a specific vertical scale at which the non-local horizontal energy transfer occurs. In figure 2.4(b), it is clear that there is essentially no effective eddy viscosity in the spherical direction when $0.1 \leq k^+ \lesssim 0.8$. Similarly, there is no spherical SGS energy transfer for $0.1 \leq k^+ \lesssim 0.8$ (figure 2.4d). There is no sign of non-local energy transfer between small and large k. As a result, the non-local horizontal energy transfer has to occur entirely at large vertical wavenumbers. This means that this non-local horizontal energy transfer and eddy viscosity correspond to a local energy transfer in the spherical direction.

We have shown that the non-local energy transfer in the horizontal direction occurs at vertical wavenumbers which are larger than k_c. Recent works (Waite, 2011; Augier et al., 2012) have found non-local energy transfer between large-horizontal-scale motions and the buoyancy wavenumber $k_b = N/u_{rms}$. For $Fr_\ell = 0.64$ the maximum of N/u_{rms}

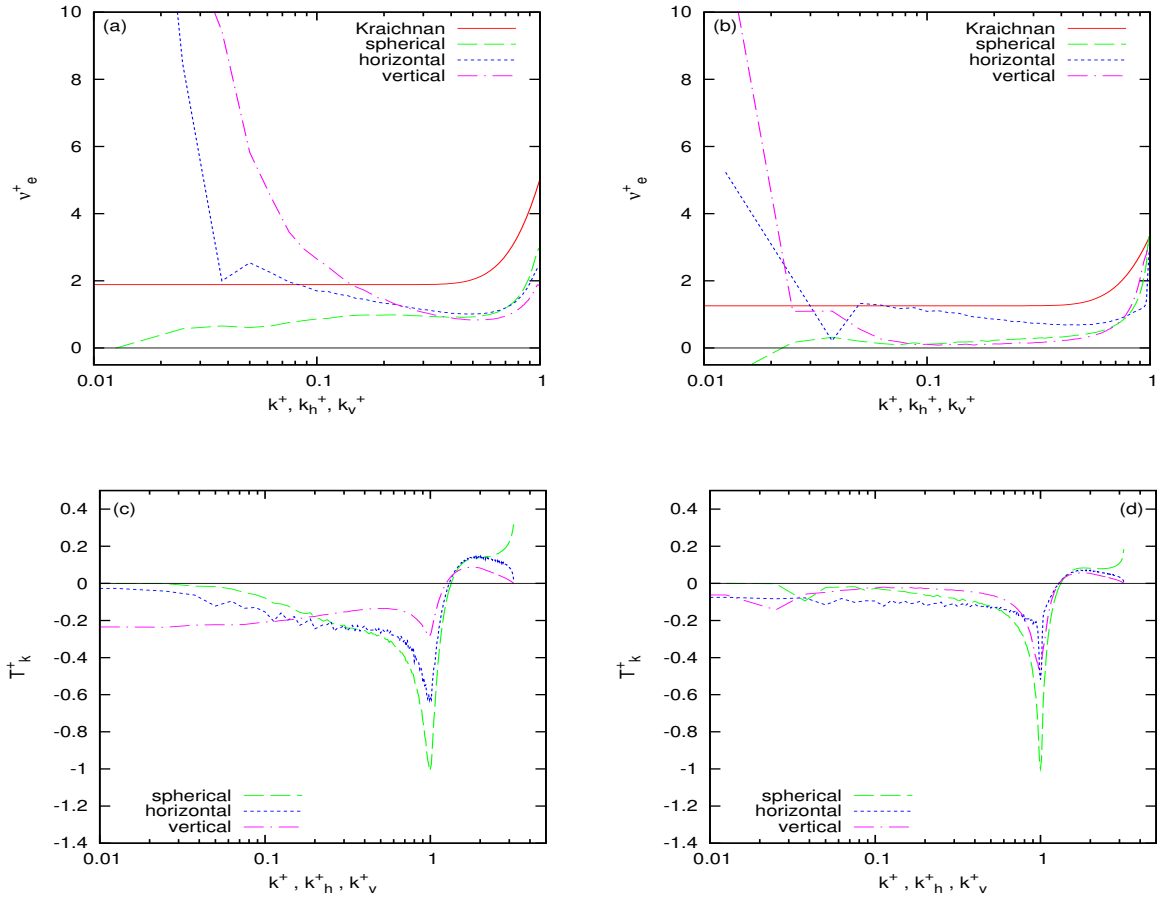

Figure 2.4: Effective eddy viscosity for (a) the unstratified case and (b) corresponding stratified case (runs UNST and $F0.6$, respectively), with $k_c = 40$. Based on the time average over the maximum dissipation rates. The theoretical eddy viscosity for the Kraichnan model (Lesieur & Rogallo, 1989) is given by the solid line. Here, ν_e^+ stands for ν_e/ν, ν_e^h/ν, and ν_e^v/ν; and $k^+ = k/k_c$, $k_h^+ = k_h/k_c$, $k_v^+ = k_v/k_c$ in all cases. Panels (c) and (d) show the corresponding SGS energy transfer spectra for the unstratified and stratified cases, respectively. Values in (c) and (d) are normalized by the corresponding absolute values of $T_k^s(k_c)$ for the non-stratified and stratified cases. The solid black line indicates the value of zero.

for $15 \leq t \leq 20$ is about 6.5. If we normalize this value by using the test cutoff k_c in figure 2.4, which is 40, it gives $k_b/k_c = 0.16$. By contrast, the Ozmidov wavenumber has $k_o/k_c \approx 1$. As seen in figures 2.4(b,d), there is a wide plateau in the horizontal direction for $0.05 \lesssim k_h^+ \lesssim 0.8$, which illustrates a non-local horizontal energy transfer between scales larger than the Ozmidov scale, including the buoyancy scale, and those smaller than the Ozmidov scale. It is noteworthy that the spherical SGS energy transfer in the stratified case is smaller than that of the non-stratified case at the cutoff $k_c = 40$, i.e. the local energy transfer, by a factor of around 2.

Consider the theoretical Kraichnan model, which is also shown in figures 2.4(a,b). This model has been calculated by assuming an infinite inertial subrange (Domaradzki et al., 1993; Métais & Lesieur, 1992) and is widely used (Lesieur & Rogallo, 1989; Briscolini & Santangelo, 1994; Cerutti et al., 2000; Carnevale et al., 2001). It has two distinct parts: a constant plateau for $k \ll k_c$ and a cusp near the cutoff k_c. By contrast, the effective eddy viscosity computed here is from DNS with a relatively short inertial subrange. Therefore, we do not expect to measure a plateau with the same amplitude as in Kraichnan's model. Batchelor et al. (1992) applied a 'zero' plateau, while retaining the cusp parameters of the Kraichnan model, to LES of homogeneous turbulence generated by buoyancy. They found that this modification increases the accuracy of the mean-square velocity fluctuations in their simulations (Batchelor et al., 1992). The long-dashed curve in figure 2.4(a) shows the measured spherical eddy viscosity. Domaradzki et al. (1987, 1993) have measured the eddy viscosity for a case of non-stratified decaying turbulence; our measured unstratified spherical eddy viscosity is very similar to theirs.

Effects of different Reynolds numbers

Two simulations with the same initial Froude number $Fr_\ell = 0.64$ but with different initial Reynolds numbers $Re_\ell = 800$ and 6400 have been considered to show the effects of changing Reynolds numbers on the effective eddy viscosity. Since the Kolmogorov wavenumber for the lower Reynolds number case is $k_d = 42$, we have applied the test cutoff wavenumber $k_c = 20$ in both high and low-resolution cases to calculate the effective eddy viscosity.

Figure 2.5 shows the spherical and horizontal effective eddy viscosities normalized by their corresponding molecular viscosities in (a,b); and normalized by just the molecular viscosity of case $Re_\ell = 6400$ in (c,d). According to figure 2.5(a), the spherical eddy viscosity of case $Re_\ell = 800$ displays an almost zero plateau for $k \ll k_c$ and a cusp near k_c. The effective eddy viscosity is much smaller than its corresponding molecular viscosity for $k, k_h < k_c$. In the $Re_\ell = 6400$ case, there is a more significant plateau, and the eddy viscosity in the cusp is much larger than its corresponding molecular viscosity (i.e.

$\nu_e^+ > 1$). These two different behaviours can be explained by the critical role of the buoyancy Reynolds number if stratified turbulence is to be ensured. The maximum value of Re_b in the $Re_\ell = 800$ case is about 0.98 and the horizontal length-scale is almost constant versus time (figure 2.3a), suggesting little if any stratified turbulence . Hence, the values of effective eddy viscosity are almost zero even at $k^+ \approx 0.7$.

The horizontal eddy viscosity for case $Re_\ell = 6400$ is dramatically affected by the occurrence of stratified turbulence. The shape of the eddy viscosity shows a large non-local horizontal eddy viscosity for $k_h \ll k_c$, and a sharp cusp nearby k_c (figure 2.5b). The horizontal eddy viscosity for the case $Re_\ell = 800$ is correspondingly very weak and very similar to its spherical eddy viscosity. Figures 2.5(c,d), illustrate the spherical and horizontal eddy viscosities in both cases which are normalized by the molecular viscosity of the case $Re_\ell = 6400$. It is found that increasing the Reynolds number increases the non-local horizontal eddy viscosity for $k_h \ll k_c$ and decreases the cusp value near k_c (figures 2.5c,d).

Effects of different Froude numbers

In this section, we study the effects of various stratifications on the effective eddy viscosity when the initial Reynolds number is $Re_\ell = 6400$ and $k_c = 40$. Two cases – one with an initial Froude number of 0.64 and the other with one of 0.32 – have been considered. The horizontal eddy viscosity for case $Fr_\ell = 0.32$ is clearly larger than that of case $Fr_\ell = 0.64$ when $k_h^+ \lesssim 0.7$ (figure 2.6b). In other words, there is an enhanced transfer of energy directly from large to small horizontal scales when the stratification is increased. The local energy transfer near the cutoff k_c, however, is less dependent on Fr_ℓ; the horizontal eddy viscosity of case $Fr_\ell = 0.64$ is slightly larger than that of case $Fr_\ell = 0.32$ at the cusp. By contrast, the effect of changing Fr_ℓ on the spherical and vertical eddy viscosities is relatively minor (figures 2.6a,c).

Effects of changing the cutoff wavenumbers

To study the effects of the cutoff wavenumber k_c on the effective eddy viscosity, the case with $Re_\ell = 6400$ and $Fr_\ell = 0.64$ has been considered with four different cutoffs $k_c = 10$, 20, 40, 80 (figure 2.7). As already mentioned, the Ozmidov wavenumber $k_o \approx 35$, so k_c ranges from smaller to larger than k_o.

Following figure 2.7(a) towards 2.7(d) shows that by increasing the value of the test cutoff k_c, the horizontal eddy viscosity changes its shape by dramatically decreasing its

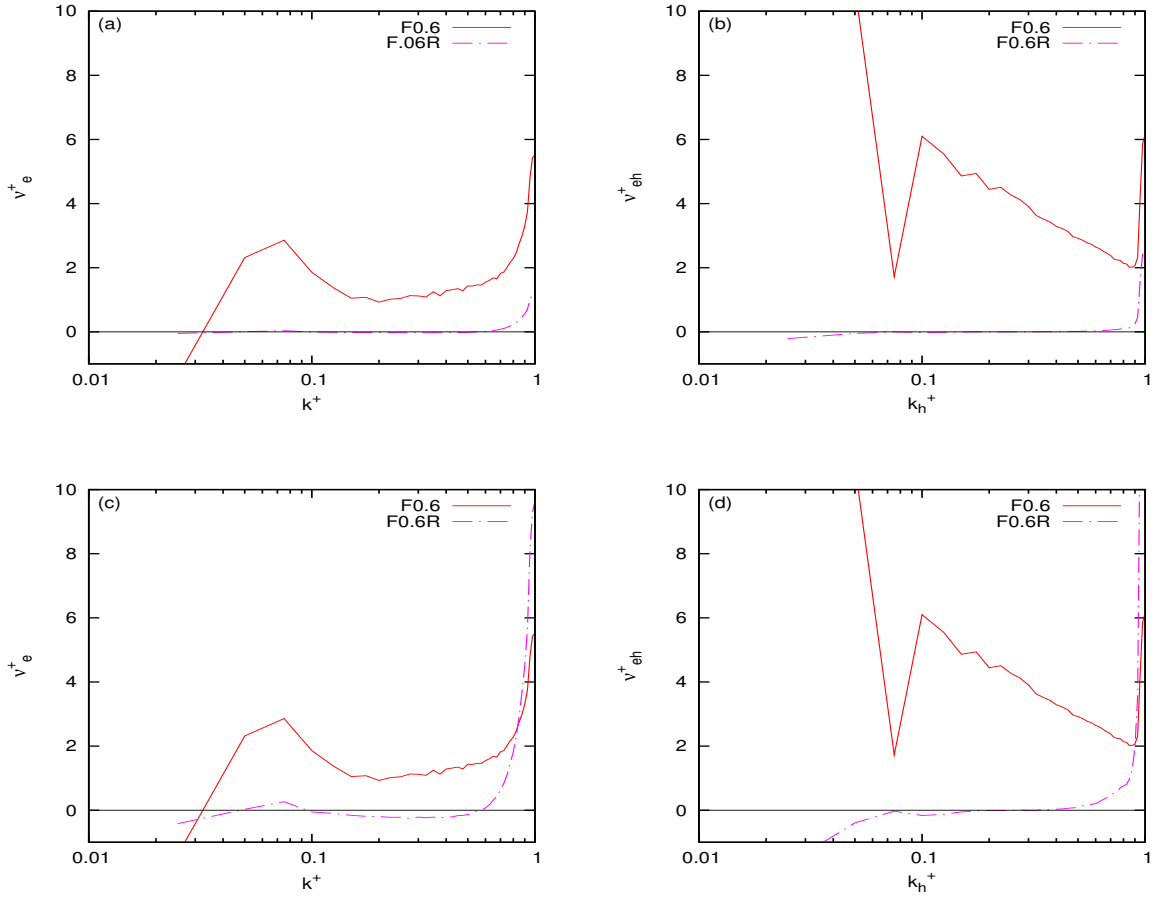

Figure 2.5: Effective (a,c) spherical and (b,d) horizontal eddy viscosity for two simulations with $Fr_\ell = 0.64$ and $Re_\ell = 6400$ (solid) and 800 (dashed), with $k_c = 20$. In (a,b), the eddy viscosity of each case are normalized by the corresponding molecular viscosity; in (c,d) they are normalized by the $Re_\ell = 6400$ molecular viscosity. The solid black line indicates the value of zero.

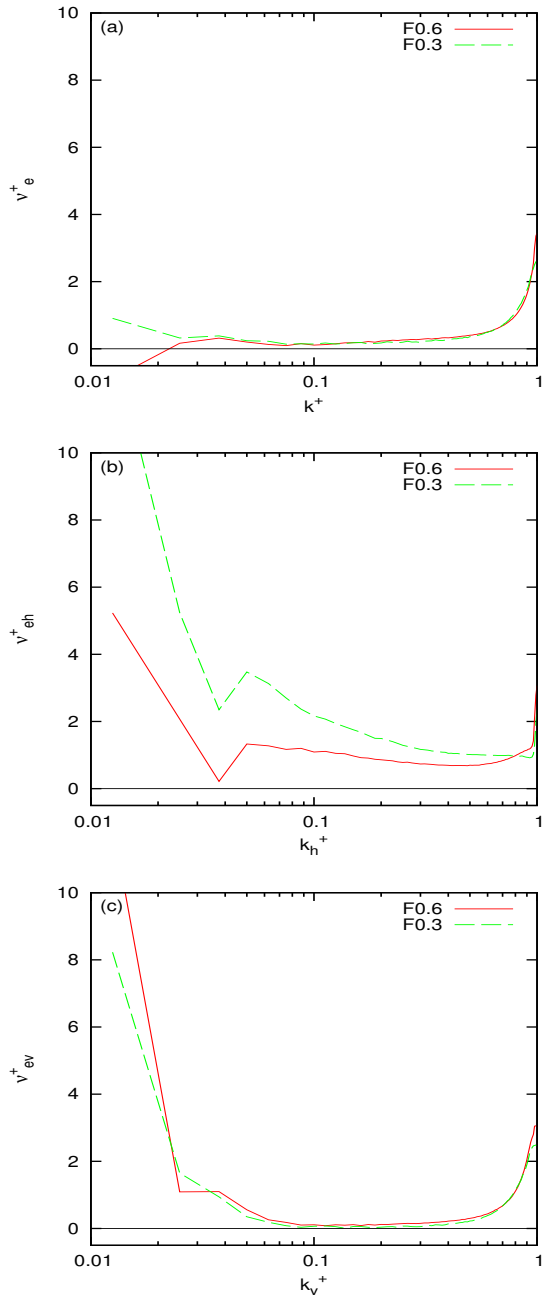

Figure 2.6: (a) Spherical, (b) horizontal, and (c) vertical effective eddy viscosity for different stratification (runs $F0.6$ and $F0.3$) at $k_c = 40$. The solid black line indicates the value of zero.

non-local ($k_h \ll k_c$) and cusp ($k_h \approx k_c$) values. This trend means that by increasing the test cutoff k_c at fixed Re_ℓ, non-local and local horizontal eddy viscosity (energy exchange) decreases, with local energy transfer dominating non-local at large k_c. Similar behaviour was observed by Bartello et al. (1996) in rotating stratified turbulence. When the cutoff k_c decreases toward the initial large scales, the horizontal eddy viscosity increases due to enhanced energy transfer between energetic horizontal motions and modes with $k_h > k_c$ (i.e. non-local horizontal energy transfer due to the elongated triads mechanism). However, when the cutoff k_c moves toward the dissipation range, modes with $k_h > k_c$ exchange less energy with energetic initial horizontal scales and more with modes with $k_h \lesssim k_c$ (i.e. the local triad mechanism). Therefore, local energy transfer dominates the non-local horizontal transfer for increased k_c (Kraichnan, 1976; Bartello et al., 1996).

According to figure 2.1(d), $k_c = 80$ is in the dissipation range; thus, the measured eddy viscosities using this cutoff are on the order of the molecular viscosity or less. As seen in figure 2.7(d), at the cutoff point (i.e. $k^+ = 1$), the value of Kraichnan's model is less than that of the molecular viscosity (i.e. $\nu_e^+ \lesssim 1$). This finding demonstrates that the cutoff value has been chosen inside the dissipation range in which the Kraichnan model is not valid. Furthermore, when $k^+ \gtrsim 0.1$, the horizontal, vertical, and spherical eddy viscosities of stratified turbulence overlap fairly well in figure 2.7(d), suggesting relative isotropy in the dissipation range in this case.

It is also interesting to consider the potential self-similarity of the effective eddy viscosity computed with different cutoffs k_c. Spherical, horizontal, and vertical effective eddy viscosities computed with four different test cutoff k_c are shown in figure 2.8. For a better evaluation of self-similarity, the vertical axes are normalized (Métais & Lesieur, 1992; Pope, 2000) by $[E(k_c)/k_c]^{1/2}$. Significant changes in the structure of the horizontal eddy viscosity (figure 2.8b) demonstrate the absence of a self-similar inertial subrange when the cutoff k_c is applied in the horizontal direction. This non-similarity in the horizontal direction make sense because self-similarity is expected mainly when local energy transfer dominates (i.e. the similarity cascade Kraichnan, 1967). By contrast, the vertical and spherical eddy viscosities show some degrees of self-similarity in the inertial subrange when $k^+, k_v^+ \gtrsim 0.1$ for $k_c \geq 20$, especially for $k_c \gtrsim k_o$ which is ≈ 35 (figure 2.8a,c).

2.5 Conclusions

Decaying stratified and non-stratified turbulence has been analyzed to measure the spherical, horizontal, and vertical eddy viscosities in DNS results. As seen in previous studies,

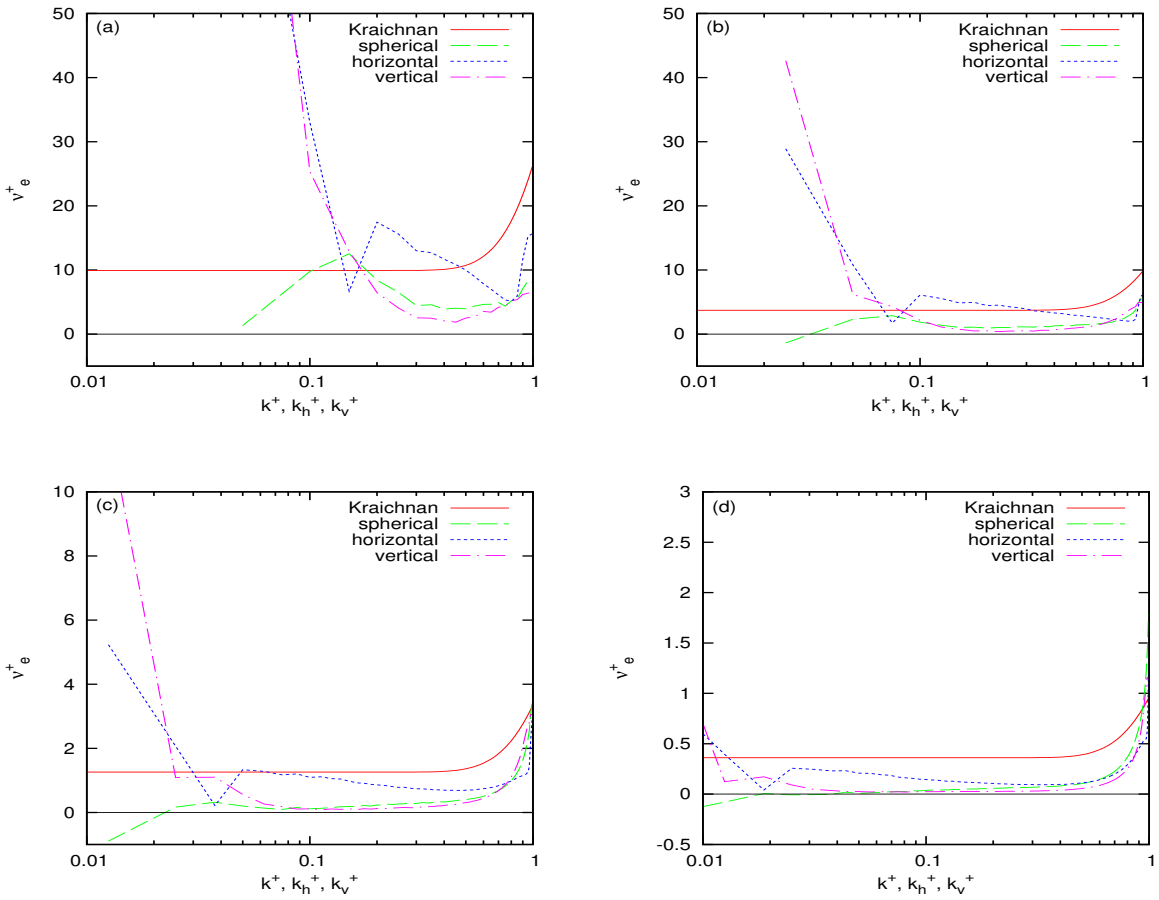

Figure 2.7: Effective eddy viscosities $F0.6$ computed with different cutoff wavenumber k_c = (a) 10, (b) 20, (c) 40, and (d) 80. The solid red line: the Kraichnan model (Lesieur & Rogallo, 1989). The scales of the vertical axes varies in panels (c) and (d) from (a,b). The solid black line indicates the value of zero.

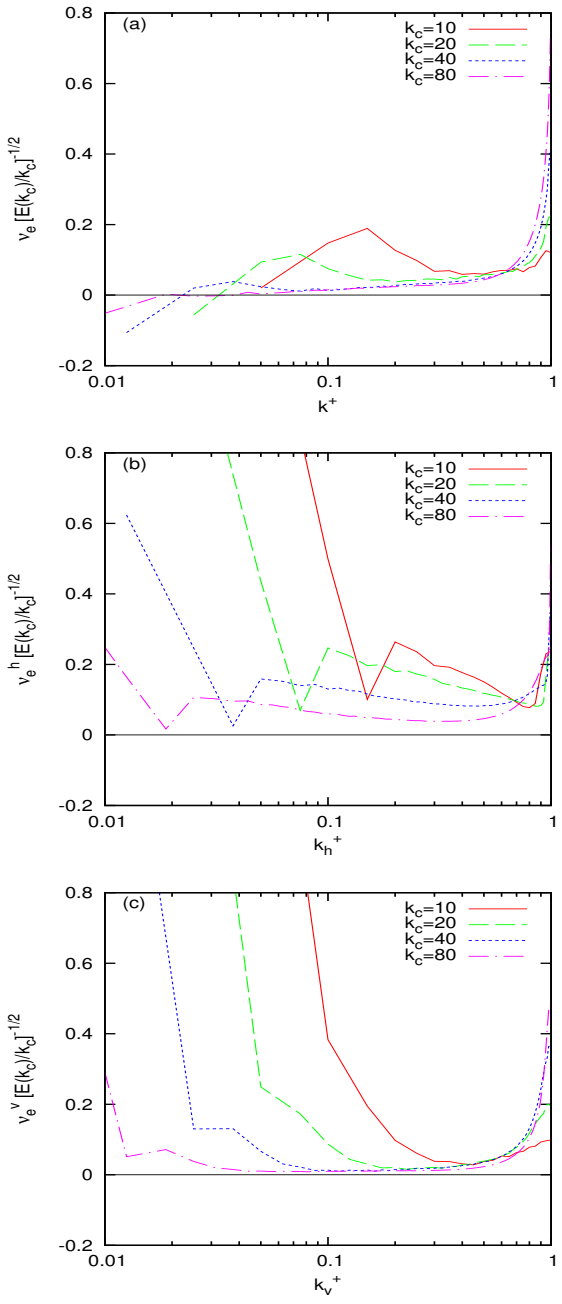

Figure 2.8: (a) Spherical, (b) horizontal, and (c) vertical effective eddy viscosity $F0.6$ using different cutoff wavenumbers k_c. Eddy viscosities are normalized (Métais & Lesieur, 1992; Pope, 2000) by $[E(k_c)/k_c]^{1/2}$ to evaluate the self-similarity clearly. The solid black line indicates the value of zero.

stratification decreases the total dissipation rate, and the time of peak dissipation is postponed. Furthermore, the energy spectrum steepens due to enhanced viscous effects when stratification increases or the Reynolds number decreases, due to the reduction of the buoyancy Reynolds number.

When $k_c = 40$, the spherical, horizontal, and vertical eddy viscosities overlap fairly well in the non-stratified case when $k^+ \gtrsim 0.1$ (i.e. small scales), but since the initial motions are anisotropic, there are clear differences between these eddy viscosities when $k^+ \lesssim 0.1$. In the non-stratified case, the non-local energy transfer in the horizontal or vertical directions may be interpreted as a local energy transfer in the spherical direction because of the Kolmogorov cascade. The effective eddy viscosities in stratified turbulence appear very different. When the cutoff is around the Ozmidov wavenumber, the horizontal and vertical eddy viscosities are quite different from one another. Furthermore, the horizontal SGS energy transfer $T_k^{s,h}$ at $k_h^+ \ll 1$ is around 20% of the local horizontal SGS energy transfer at $k^+ = 1$. Meanwhile, T_k^s at $k^+ = 1$ for the stratified case is two times smaller than that of the non-stratified case. These behaviours show an almost constant plateau in horizontal energy transfer for $k_h \ll k_c$, and a decrease in local energy transfer near k_c, in the presence of strong stratification. Positive values of the horizontal eddy viscosities demonstrate a forward energy cascade from large to small horizontal scales in stratified turbulence, as seen in other studies (Riley & de Bruyn Kops, 2003; Waite & Bartello, 2004; Lindborg, 2006; Brethouwer et al., 2007; Riley & Lindborg, 2008; Waite, 2011; Almalkie & de Bruyn Kops, 2012; Waite, 2014).

These results are consistent with the findings of Augier et al. (2012) in which a columnar vortex pair first transforms into layered structures at large horizontal scales. We claim that the large positive vertical eddy viscosity of stratified turbulence at large vertical scales (i.e. $k_v^+ \lesssim 0.02$) shows a non-local energy transfer from large to small vertical scales. Moreover, we have shown that for stratified turbulence, there is energy transfer directly from large to small horizontal scales in the range of large vertical wavenumbers, i.e. non-local in the horizontal direction but local in the spherical direction. This finding is reminiscent of the second stage of the vortex breakdown discussed by Augier et al. (2012), in which secondary Kelvin-Helmholtz instabilities are generated and ultimately transition into small-scale turbulence below the buoyancy scale. Our results show that energy may transfer directly to horizontal scales that are even smaller than the buoyancy scale. Further studies with a wider scale separation between the initial, buoyancy, and cutoff wavenumbers are needed to investigate the details of direct non-local horizontal energy transfer between the (large) energetic scales with wavenumbers below k_c, and small-scale motions with wavenumbers above k_c. However, this large separation would requires a high Re_ℓ and Re_b.

Changing the cutoff wavenumber k_c has a considerable effect on the shapes and values of effective eddy viscosities. When the cutoff is near the scale of the initial conditions, the values of measured horizontal eddy viscosity shows a non-local transfer for $k_h \ll k_c$. However, by moving the cutoff k_c towards the Kolmogorov scale, the effective eddy viscosity decreases dramatically. This behaviour demonstrates a decrease in the non-local horizontal energy transfer by increasing the value of test cutoff k_c into the dissipation range, as expected.

We have confirmed that stratification modifies the effective eddy viscosity qualitatively. A stratified inertial subrange that clearly includes scales above and below the Ozmidov scale requires very high Reynolds number. Such an inertial subrange is difficult to obtain with a DNS approach. By contrast, LES of stratified turbulence, in which the Ozmidov scale is not resolved, is seriously affected by anisotropic features. Kraichnan's theoretical model is based on the assumption that local energy transfer, near the cutoff k_c, dominates non-local energy transfer, at $k \ll k_c$. This idea was also confirmed by Domaradzki et al. (1993) in DNS results of non-stratified isotropic turbulence. However, as shown here, the presence of stratification increases the non-local horizontal energy transfer for $k_h \ll k_c$, between large energetic and SGS horizontal motions, which is significant. Therefore, an isotropic SGS model such as the Kraichnan model (with the infinite inertial subrange) does not seem to be a proper approach for LES of stratified turbulence. For example, in a recent paper by Schaefer-Rolffs & Becker (2013) about large-scale atmospheric dynamics, where stratification is important, a dynamic Smagorinsky model has been applied just to the horizontal direction. Our future work will include investigations on how to improve current SGS models to consider the effects of anisotropy and non-locality and hence the effects of stratification in the horizontal direction.

2.6 Acknowledgment

The authors would like to thank Kevin Lamb and two anonymous referees for helpful discussions and comments on this paper. This work was made possible by the facilities of the Shared Hierarchical Academic Research Computing Network (SHARCNET: www.sharcnet.ca) and Compute/Calcul Canada. Financial support from the Natural Sciences and Engineering Research Council of Canada is gratefully acknowledged.

Chapter 3

Buoyancy scale effects in large eddy simulations of stratified turbulence

In this chapter LES of forced stratified turbulence using two common SGS models, the Kraichnan and Smagorinsky models, are studied. It is shown that if the grid spacing Δ is fine enough, the horizontal wavenumber energy spectrum presents an approximately $-5/3$ slope, along with a bump around the buoyancy wavenumber k_b. Our results also suggest a critical value for Δ, below which the dynamics of stratified turbulence are fully captured. This criterion depends on the adopted SGS model and resolving the buoyancy lengthscale L_b.

This chapter is based on the published paper, Khani S. and M. L. Waite. Buoyancy scale effects in large-eddy simulations of stratified turbulence. *J. Fluid Mech.* 754: 75-97 2014,

3.1 Introduction

Stratified turbulence is characterized by very large Reynolds number $Re = u_{rms} l_h/\nu$ and sufficiently small horizontal Froude number $Fr_h = u_{rms}/N l_h$, such that the buoyancy Reynolds number

$$Re_b = Re\, Fr_h^2, \tag{3.1}$$

is also high (Brethouwer et al., 2007). Here, u_{rms} and l_h are the root-mean-square velocity and horizontal length scale, respectively; ν is the molecular viscosity and N is the buoyancy frequency. According to Taylor's hypothesis, $l_h \sim (u_{rms})^3/\epsilon$, and so equation (3.1) yields

$$Re_b \sim \frac{\epsilon}{\nu N^2}, \tag{3.2}$$

where ϵ is the kinetic energy dissipation rate (the use of Taylor's hypothesis for stratified turbulence is common, but may be questionable; see e.g. Hebert & de Bruyn Kops, 2006b; Khani & Waite, 2013). The Ozmidov scale (e.g. Lumely, 1964)

$$L_o = 2\pi \left(\frac{\epsilon}{N^3}\right)^{1/2}, \tag{3.3}$$

is the smallest scale for which buoyancy effects are important. (We include the 2π factor in (3.3) and for other characteristic length scales because it is often the corresponding wavenumber $k_o = 2\pi/L_o$ that appears in applications; e.g. Waite, 2011). Based on the stratified turbulence hypothesis (Lindborg, 2006), the Ozmidov scale divides the inertial subrange into two parts: an anisotropic part, from large scales down to the Ozmidov scale; and an isotropic part, for smaller scales down to the Kolmogorov scale $\eta = 2\pi\left(\nu^3/\epsilon\right)^{1/4}$. The dynamical picture of stratified turbulence is described by flat horizontal motions and suppressed the vertical velocity, in which the vertical structure is characterized by layers of thickness

$$L_b = 2\pi \frac{u_{rms}}{N}, \tag{3.4}$$

which is named the buoyancy scale (e.g. Riley & de Bruyn Kops, 2003; Waite & Bartello, 2004; Lindborg, 2006). Previous work (e.g. Waite & Bartello, 2004; Lindborg, 2006; Brethouwer et al., 2007; Waite, 2011, 2014) shows that resolution of L_b is necessary to capture the stratified turbulence cascade.

Direct numerical simulation (DNS) of stratified turbulence is very challenging because the ratio of the Ozmidov to Kolmogorov scales depends on the buoyancy Reynolds number as follows

$$\frac{L_o}{\eta} = \left(\frac{\epsilon}{\nu N^2}\right)^{3/4} \sim Re_b^{3/4}. \tag{3.5}$$

Since stratified turbulence has $Re_b \gg 1$, and DNS requires resolution of the Kolmogorov scale, it is necessary that the grid spacing be much smaller than the Ozmidov scale. An alternative approach is large-eddy simulation (LES), for which large scales are resolved but subgrid scale (SGS) motions, including the small-scale end of the inertial subrange, are modelled. Owing to the computational costs, we are interested in performing LES of stratified turbulence, in which the grid spacing Δ may be larger than the Ozmidov scale L_o. However, previous numerical studies with hyperviscosity suggest that resolution of the buoyancy scale may be important (e.g. Waite & Bartello, 2004; Lindborg, 2006; Waite, 2011). In this paper, we investigate the performance of two common LES schemes, the Smagorinsky (1963) and Kraichnan (1976) models, in simulations of stratified turbulence. For both schemes, we determine the extent to which the buoyancy scale needs to be resolved for the LES to capture the dynamics of stratified turbulence properly.

In §3.2, we review the literature of stratified turbulence, the LES approach, and the classical SGS models. The methodology including numerical approach outlined in §3.3. Section 3.4 includes results and their interpretations. Concluding remarks are given in §3.5.

3.2 Background

3.2.1 Stratified turbulence

Most previous numerical studies in stratified turbulence are DNS and hyperviscosity simulations. Hyperviscosity simulations are performed in the same spirit as DNS: the viscosity and diffusion operators are modified to extend the inertial range, but the associated dissipation scale is resolved (e.g. Waite & Bartello, 2004). Recent advances in the study of stratified turbulence show that a layerwise structure emerges, in which the horizontal lengthscale is much larger than the vertical one (e.g. Billant & Chomaz, 2001; Riley & de Bruyn Kops, 2003; Hebert & de Bruyn Kops, 2006b; Brethouwer et al., 2007). In addition, there is a forward energy transfer mechanism from large to small horizontal scales (e.g. Waite & Bartello, 2004; Lindborg, 2006; Brethouwer et al., 2007). For scales larger than L_o, different kinetic energy spectral slopes have been proposed in the horizontal and vertical directions. Lindborg (2006) argued that $-5/3$ in k_h and -3 in k_v are expected, where $k_h = \sqrt{k_x^2 + k_y^2}$ is the horizontal wavenumber, $k_v = |k_z|$ is the vertical wavenumber, and $\boldsymbol{k} = (k_x, k_y, k_z)$ is the three-dimensional wavevector. When L_b is not resolved in the vertical direction, a steeper horizontal spectrum, with a slope as large as -5, results (e.g. Waite & Bartello, 2004). Even when L_b is resolved, deviations from the $-5/3$ slope have

been reported; e.g. Waite (2011) and Kimura & Herring (2012) found slopes closer to -2. Moreover, *a priori* testing shows that the horizontal and vertical effective eddy viscosities are very different when the test cutoff wavenumber k_c is smaller than k_o (Khani & Waite, 2013). Finally, a non-local horizontal energy transfer from large horizontal scale to the buoyancy scale, associated with Kelvin-Helmholtz (KH) instabilities, has been found in forced stratified turbulence (Waite, 2011, 2014), the breakdown of columnar vortices (Augier et al., 2012), and decaying stratified turbulence (Khani & Waite, 2013). All of the results described above have been found when DNS or hyperviscosity simulation is the adopted numerical approach. Despite the emphasis on hyperviscosity and DNS, some LES studies have been investigated (e.g. Siegel & Domaradzki, 1994; Carnevale et al., 2001; Smith & Waleffe , 2002; Remmler & Hickel, 2012; Paoli et al., 2013). We are interested in studying LES of stratified turbulence and determining the dependence of the results on the grid spacing Δ.

3.2.2 Large-eddy simulations

LES is based on the filtered equations of motion, where the filter applied to a variable q is given by (e.g. Leonard, 1974; Pope, 2000)

$$\bar{q}(\boldsymbol{x},t) = \int_D G(\boldsymbol{x}-\acute{\boldsymbol{x}},\boldsymbol{x})q(\acute{\boldsymbol{x}},t)\mathrm{d}\acute{\boldsymbol{x}}, \tag{3.6}$$

where $\bar{q}(\boldsymbol{x},t)$ is the filtered quantity, G is a filtering function, which generally depends on $\boldsymbol{x}$ and the distance between two-correlation points, i.e. $\boldsymbol{r}=\boldsymbol{x}-\acute{\boldsymbol{x}}$, and D is the spatial domain. In practice, it is customary to work with homogeneous and isotropic filter functions that are independent of $\boldsymbol{x}$ and $\boldsymbol{r}$, and just depend on $r=|\boldsymbol{r}|$. There are a few applicable homogeneous filter functions (see e.g. Pope, 2000). For the spectral transform numerical method, it is convenient to work with the sharp spectral filter (as applied in e.g. Germano et al., 1991; Piomelli et al., 1991; Moin et al., 1991; Kang et al., 2003), which is defined as follows

$$\hat{G}(\boldsymbol{k}) = \begin{cases} 1 & : \quad |\boldsymbol{k}| \leq k_c \\ 0 & : \quad |\boldsymbol{k}| > k_c \end{cases}, \tag{3.7}$$

where $\hat{G}$ is the Fourier coefficient of G, $\boldsymbol{k}$ is the wavenumber vector, and k_c is the cutoff wavenumber. By applying the filter function $\hat{G}$ to variable q, we get

$$\bar{q}(\boldsymbol{x},t) = \sum_{\boldsymbol{k}} \hat{q}(\boldsymbol{k},t)\hat{G}(\boldsymbol{k})e^{i\boldsymbol{k}\cdot\boldsymbol{x}} = \sum_{|\boldsymbol{k}|\leq k_c} \hat{q}(\boldsymbol{k},t)e^{i\boldsymbol{k}\cdot\boldsymbol{x}}, \tag{3.8}$$

where Fourier modes with wavenumbers smaller than k_c are maintained and the larger modes are killed. The LES grid spacing Δ and filter cutoff k_c are related by

$$\Delta \equiv \frac{\pi}{k_c}. \tag{3.9}$$

Physical space

Applying the sharp spectral filter to the Navier-Stokes equations under the Boussinesq approximation, which is non-dimensionalized with a velocity scale u and length scale ℓ, yield (following the notation of Pope, 2000)

$$\frac{\partial \bar{u}_i}{\partial t} + \frac{\partial}{\partial x_j}(\bar{u}_i \bar{u}_j) = -\frac{\partial \bar{p}}{\partial x_i} - \frac{1}{{Fr_\ell}^2}\bar{\rho}\boldsymbol{e}_z - \frac{\partial \tau^r_{ij}}{\partial x_j} + \bar{f}_i, \tag{3.10}$$

$$\frac{\partial \bar{u}_j}{\partial x_j} = 0, \tag{3.11}$$

$$\frac{\partial \bar{\rho}}{\partial t} + \frac{\partial}{\partial x_j}(\bar{\rho}\bar{u}_j) - \bar{w} = -\frac{\partial h_j}{\partial x_j}, \tag{3.12}$$

where $\boldsymbol{u}$, p, ρ, and $\boldsymbol{f}$ are the velocity, perturbation pressure, perturbation density, and forcing fields, respectively; and $Fr_\ell = u/N\ell$ is the Froude number. Since we assume large Reynolds numbers and that Δ is much larger than the Kolmogorov scale, viscous dissipation and diffusion are neglected. The subgrid momentum flux $\boldsymbol{\tau}$ and the subgrid density flux $\boldsymbol{h}$ are given as follows

$$\tau_{ij} = \overline{u_i u_j} - \bar{u}_i \bar{u}_j, \tag{3.13}$$

$$h_j = \overline{u_j \rho} - \bar{u}_j \bar{\rho}. \tag{3.14}$$

The deviatoric part of $\boldsymbol{\tau}$ is defined as

$$\tau^r_{ij} = \tau_{ij} - \frac{1}{3}\tau_{rr}\delta_{ij}, \tag{3.15}$$

where the modified pressure $\bar{p}$ absorbs the isotropic part of the subgrid momentum flux. The filtered momentum and energy equations (3.10,3.12) are not closed because $\boldsymbol{\tau}^r$ and $\boldsymbol{h}$ are not known in terms of the filtered velocity and density fields. We need to model these unknown fluxes using the SGS models.

Wavenumber space

Similar to physical space, we could work in Fourier space to perform LES of stratified turbulence. Applying the sharp spectral filter $\hat{G}(\boldsymbol{k})$ to the Navier-Stokes equations under the Boussinesq approximation in Fourier space, yields

$$\frac{\partial}{\partial t}\hat{\bar{u}}_j(\boldsymbol{k},t) + \frac{1}{{Fr_\ell}^2}\hat{\bar{\rho}}(\boldsymbol{k},t)\boldsymbol{e}_z = -ik_m P_{jr}(\boldsymbol{k}) \sum_{\substack{\boldsymbol{p}+\boldsymbol{q}=\boldsymbol{k},\\ |\boldsymbol{k}|<k_c}} \hat{u}_r(\boldsymbol{p},t)\hat{u}_m(\boldsymbol{q},t) + \hat{\bar{f}}_j, \tag{3.16}$$

$$k_j\hat{\bar{u}}_j(\boldsymbol{k},t) = 0, \tag{3.17}$$

$$\frac{\partial}{\partial t}\hat{\bar{\rho}}(\boldsymbol{k},t) - \hat{\bar{w}}(\boldsymbol{k},t) = -ik_m \sum_{\substack{\boldsymbol{p}+\boldsymbol{q}=\boldsymbol{k},\\ |\boldsymbol{k}|<k_c}} \hat{u}_m(\boldsymbol{p},t)\hat{\rho}(\boldsymbol{q},t), \tag{3.18}$$

where $P_{ij} = \delta_{ij} - k_i k_j/k^2$ is the projection tensor, and $k^2 = \boldsymbol{k}\cdot\boldsymbol{k}$. Like in physical space, non-linear terms in the right-hand side of (3.16,3.18), i.e.

$$F_j(\boldsymbol{k},t) = -ik_m P_{jr}(\boldsymbol{k}) \sum_{\substack{\boldsymbol{p}+\boldsymbol{q}=\boldsymbol{k},\\ |\boldsymbol{k}|<k_c}} \hat{u}_r(\boldsymbol{p},t)\hat{u}_m(\boldsymbol{q},t), \tag{3.19}$$

$$J(\boldsymbol{k},t) = -ik_m \sum_{\substack{\boldsymbol{p}+\boldsymbol{q}=\boldsymbol{k},\\ |\boldsymbol{k}|<k_c}} \hat{u}_m(\boldsymbol{p},t)\hat{\rho}(\boldsymbol{q},t), \tag{3.20}$$

are not known in terms of the filtered Fourier coefficients $\hat{\bar{\boldsymbol{u}}}$ and $\hat{\bar{\rho}}$. Based on the definition of the cutoff wavenumber k_c, we could divide (3.19) into a filtered term $\bar{\boldsymbol{F}}$ and a subgrid term $\boldsymbol{F}^s$, such that

$$\bar{F}_j(\boldsymbol{k},t) = -ik_m P_{jr}(\boldsymbol{k}) \sum_{\substack{\boldsymbol{p}+\boldsymbol{q}=\boldsymbol{k},\\ |\boldsymbol{k}|<k_c}} \hat{\bar{u}}_r(\boldsymbol{p},t)\hat{\bar{u}}_m(\boldsymbol{q},t), \tag{3.21}$$

$$F^s_j(\boldsymbol{k},t) = -ik_m P_{jr}(\boldsymbol{k}) \sum_{\substack{\boldsymbol{p}+\boldsymbol{q}=\boldsymbol{k},\\ |\boldsymbol{k}|<k_c,\ \max\{|\boldsymbol{p}|,|\boldsymbol{q}|\}>k_c}} \hat{u}_r(\boldsymbol{p},t)\hat{u}_m(\boldsymbol{q},t), \tag{3.22}$$

in which $\boldsymbol{F}^s$ is unknown and needs to be modelled using SGS models. In a similar way, equation (3.20) could be divided into the filtered term $\bar{J}$ and the subgrid term J^s, for which the latter is unknown and should be modelled to close the problem.

3.2.3 SGS models

Most SGS models are based on the eddy viscosity assumption, which is based on the turbulent-viscosity hypothesis (e.g. Pope, 2000). In this point of view, the nonlinear subgrid terms are related to the filtered physical variables or the filtered Fourier coefficients through an eddy viscosity term in physical or wavenumber space, respectively. We consider two SGS models here: the Smagorinsky (1963) model, which is local in physical space and damps resolved regions with strong rate of strain; and the Kraichnan (1976) model, which is spectrally local and damps mainly the smallest resolved length scales.

The Smagorinsky model (physical space)

The deviatoric part of the subgrid flux $\boldsymbol{\tau}^r$ is related to the filtered rate of strain $\bar{s}_{ij} = 1/2(\partial\bar{u}_i/\partial x_j + \partial\bar{u}_j/\partial x_i)$ using the eddy viscosity coefficient ν_r, as

$$\tau^r_{ij}(\boldsymbol{x},t) = -2\nu_r(\boldsymbol{x},t)\bar{s}_{ij}(\boldsymbol{x},t). \tag{3.23}$$

Similarly, the subgrid density flux $\boldsymbol{h}$ is modelled by

$$h_j(\boldsymbol{x},t) = -\frac{2}{Pr_t}\nu_r(\boldsymbol{x},t)\frac{\partial}{\partial x_j}\bar{\rho}(\boldsymbol{x},t), \tag{3.24}$$

where Pr_t is the turbulent Prandtl number. Smagorinsky (1963) suggested a model for eddy viscosity coefficient for which ν_r is related to the grid spacing Δ and the characteristic filtered rate of strain $\bar{S} = (2\bar{s}_{ij}\bar{s}_{ij})^{1/2}$, through the relation

$$\nu_r(\boldsymbol{x},t) = (c_s\Delta)^2\bar{S}(\boldsymbol{x},t), \tag{3.25}$$

where c_s is the Smagorinsky coefficient. Lilly (1967) has shown that (3.25) is an applicable model for LES of three dimensional turbulence. An estimate of $c_s \approx 0.17$ was made (Lilly, 1967; Pope, 2000; Meneveau &, Katz 2000) for a Kolmogorov isotropic inertial subrange with a sharp spectral filter.

The Kraichnan model (wavenumber space)

Kraichnan (1976) suggested the spectral eddy viscosity idea to model the nonlinear subgrid term $\boldsymbol{F}^s$ as (using the notation of Pope, 2000)

$$F^s_j(\boldsymbol{k},t) = -\nu_e(k|k_c)k^2\hat{\bar{u}}_j(\boldsymbol{k},t), \tag{3.26}$$

where $\nu_e(k|k_c)$ is the spectral eddy viscosity function. Similarly, the subgrid term J^s is related to the filtered Fourier coefficient $\hat{\tilde{\rho}}$ as follows

$$J^s(\boldsymbol{k},t) = -\frac{1}{Pr_t}\nu_e(k|k_c)k^2\hat{\tilde{\rho}}(\boldsymbol{k},t). \tag{3.27}$$

Lesieur & Rogallo (1989) proposed the following equation for $\nu_e(k|k_c)$

$$\nu_e(k|k_c) = (0.15 + 5e^{-3.03k_c/k})\sqrt{\frac{E(k_c,t)}{k_c}}, \tag{3.28}$$

where $E(k_c,t)$ is the kinetic energy spectrum at the cutoff wavenumber k_c. It is important to note that for $k \ll k_c$,

$$\nu_e(k|k_c) \sim 0.15\sqrt{\frac{E(k_c,t)}{k_c}}. \tag{3.29}$$

Hence, the eddy viscosity coefficient $\nu_e(k|k_c)$ is independent of $\boldsymbol{k}$ for small wavenumbers. By contrast with the Smagorinsky approach, the Kraichnan model has the advantage that it preferentially damps small length scales; however, it is only practical for idealized simulations with triply periodic spectral codes.

The turbulent Prandtl number Pr_t is usually assumed to be constant (e.g. Lesieur, 1990; Batchelor et al., 1992; Siegel & Domaradzki, 1994). This assumption along with the assumption of constant buoyancy frequency N (e.g. Riley & de Bruyn Kops, 2003; Waite & Bartello, 2004; Brethouwer et al., 2007; Waite, 2011; Khani & Waite, 2013; Waite, 2014) will also be employed in current study.

3.3 Methodology

LES of forced stratified turbulence is studied in this paper. Idealized simulations of vortically-forced stratified turbulence in a cubic domain with length $L = 2\pi$ is considered. Random forcing of barotropic vortical modes in the wavenumber band $|k_h - k_f| \leq 1$ is applied, where k_f is the forcing wavenumber (following e.g. Herring & Métais, 1989; Waite & Bartello, 2004; Waite, 2011). The forcing is AR(1) red noise, uncorrelated in $\boldsymbol{k}$, and with a correlation time scale of 10 timesteps (as in e.g. Waite & Bartello, 2004). The forcing amplitude is a quadratic function of the horizontal wavenumber k_h centred in the forcing band. The forcing amplitude is the same for all simulations, apart from a factor of $\Delta t^{-1/2}$, which leads to an approximately fixed average forcing power in all cases. The

spectral transform method with cubic truncation is applied for discretization in space. The two-thirds rule (e.g. Durran, 2010) is applied to eliminate aliasing errors, meaning that the cutoff wavenumber k_c is

$$k_c = \pi \frac{2n}{3L}, \tag{3.30}$$

where n is the number of grid points in the x, y, and z directions. We get the effective resolution $\Delta = 1.5L/n$ by using (3.30) in (3.9). The third-order Adams-Bashforth scheme is employed for time stepping.

We compare our LES results with those obtained using hyperviscosity and hyperdiffusivity, which are commonly employed to mimic large Reynolds number flows in place of traditional LES schemes. These dissipation operators are of forms

$$D_u = \nu_m (-1)^{m+1} \nabla^{2m}, \tag{3.31}$$

$$D_b = \kappa_m (-1)^{m+1} \nabla^{2m}, \tag{3.32}$$

respectively, where ν_m and κ_m are the hyperviscosity and hyperdiffusivity coefficients (see e.g. Waite & Bartello, 2004). We set $\nu_m = \kappa_m$, and use $m = 4$ (as in e.g. Bartello et al., 1996; Waite & Bartello, 2004; Waite, 2011). The modified Kolmogorov wavenumber in the hyperviscosity case is as follows

$$k_d = \left(\frac{\epsilon}{\nu_4^3} \right)^{1/22}. \tag{3.33}$$

For a given resolution, the hyperviscosity coefficient is chosen to be as small as possible while still adequately resolving k_d. The implicit trapezoidal method is applied for time stepping of dissipation term in the hyperviscosity and hyperdiffusivity simulations.

Following previous studies of forced stratified turbulence (e.g. Waite & Bartello, 2004; Waite, 2011) we spin up our simulations with relatively low resolution ($n = 256$) and hyperviscosity from time 0 to 300 (corresponding to around 30 forcing time scales; see below), and then use these low-resolution results as initial conditions for higher-resolution LES from time 300 to 450. Resolutions from $n = 256$ to $n = 768$ are considered.

The buoyancy frequency N ranges from 2 to 6, which are chosen to be strongly stratified; indeed, the corresponding Froude numbers ranges from 0.0024 to 0.014, as will be presented in the next section. Similar ranges for Froude numbers have been considered in previous numerical studies of stratified turbulence (e.g. Riley & de Bruyn Kops, 2003; Hebert & de Bruyn Kops, 2006b,a; Khani & Waite, 2013). These Froude numbers are a little larger than typical values of the atmospheric mesoscale ($\sim 10^{-4}$; e.g. Brune & Becker, 2013) but meet the criteria for strongly stratified turbulence (Lindborg, 2006). The corresponding

Ozmidov scales are not resolved in these experiments; however, previous hyperviscosity simulations have shown and argued that it is sufficient to resolve the buoyancy scale (e.g. Waite & Bartello, 2004; Lindborg, 2006; Brethouwer et al., 2007). The forcing amplitude gives a typical dissipation rate of 10^{-4} which, when combined with the forcing wavenumber k_f, gives a forcing time scale $t_f \sim 10$. We use $\sqrt{\langle E(t) \rangle}$ in place of u_{rms} since the vertical kinetic energy is much smaller than the horizontal. The turbulent Prandtl number $Pr_t = 1$ for LES and the forcing wavenumber $k_f = 3$ are also considered in this study. Tables 3.1 and 3.2 show a list of parameters and averaged variables for hyperviscosity simulations and LES, respectively.

Table 3.1: List of numerical simulations with hyperviscosity.

Hyperviscosity	N	n	ν_4	k_{max}	k_b	k_d	k_o	$\langle\epsilon\rangle$	$\langle E(t)\rangle$	Fr_h	Δt
h7N2	2	768	8.42×10^{-19}	256	30	186	402	5.0×10^{-5}	0.0045	0.0055	0.0060
h7N4	4	768	8.42×10^{-19}	256	58	187	1042	5.9×10^{-5}	0.0048	0.0031	0.0055
h7N6	6	768	8.42×10^{-19}	256	77	191	1565	8.8×10^{-5}	0.0060	0.0024	0.0050
h2N2	2	256	3.18×10^{-15}	85	29	62	325	7.6×10^{-5}	0.0047	0.0080	0.0180
h2N4	4	256	3.18×10^{-15}	85	51	62	771	1.1×10^{-4}	0.0061	0.0044	0.0165
h2N6	6	256	3.18×10^{-15}	85	72	63	1374	1.1×10^{-4}	0.0070	0.0027	0.0150

Table 3.2: List of numerical simulations with LES.

Smagorinsky	N	n	k_b	k_c	k_o	$\langle\epsilon\rangle$	$\langle E(t)\rangle$	Fr_h	k_c/k_b	Δ/L_b	Δt
S7N2	2	768	32	254	286	9.8×10^{-5}	0.0039	0.012	7.94	0.063	0.0060
S7N4	4	768	62	254	773	1.1×10^{-4}	0.0043	0.006	4.10	0.122	0.0055
S7N6	6	768	86	254	1391	1.1×10^{-4}	0.0048	0.004	2.95	0.169	0.0050
S5N2	2	512	31	168	262	1.2×10^{-4}	0.0042	0.014	5.42	0.092	0.0090
S5N4	4	512	57	168	710	1.3×10^{-4}	0.0050	0.006	2.95	0.169	0.0082
S2N2	2	256	32	83	282	1.0×10^{-4}	0.0040	0.013	2.59	0.193	0.0180
Kraichnan	N	n	k_b	k_c	k_o	$\langle\epsilon\rangle$	$\langle E(t)\rangle$	Fr_h	k_c/k_b	Δ/L_b	Δt
K7N2	2	768	30	254	266	1.1×10^{-4}	0.0045	0.012	8.47	0.059	0.0060
K7N6	6	768	82	254	1368	1.2×10^{-4}	0.0053	0.004	3.10	0.161	0.0050
K2N2	2	256	31	83	272	1.1×10^{-4}	0.0042	0.013	2.68	0.186	0.0180
K2N4	4	256	57	83	738	1.2×10^{-4}	0.0050	0.006	1.45	0.345	0.0165
K2N6	6	256	78	83	1270	1.3×10^{-4}	0.0060	0.004	1.06	0.472	0.0150

3.4 Results and discussion

3.4.1 Overview of simulations

Figure 3.1 shows time series of kinetic energy and dissipation rates for the hyperviscosity simulations (a,b), the Smagorinsky LES (c,d), and the Kraichnan LES (e,f), when $0 \leq t \leq 450$. The simulations appear to have reached statistical stationarity for $375 \leq t \leq 450$, which is the time period for averaging of the results that follow. The time series of the kinetic energy dissipation rates $\epsilon(t)$ exhibit a discontinuity at $t = 300$, due to the change in resolution and SGS mechanism at this time. Interestingly, the Smagorinsky and Kraichnan dissipation rates are similar, and are both close to the lower-resolution hyperviscosity case (tables 3.1 and 3.2, where the angle brackets $\langle\cdot\rangle$ denote for time averaging). We will discuss this dependence on SGS scheme in §3.4.2. In addition, increasing the stratification increases kinetic energy and u_{rms} (tables 3.1 and 3.2).

3.4.2 Energy spectra

In this section, we study effects of the grid spacing in different SGS models on the energy and dissipation spectra. In figure 3.2, averaged total, horizontal, and vertical wavenumber kinetic energy are shown for the highest-resolution simulations. Kinetic energy spectra in terms of total, horizontal, and vertical wavenumbers k, k_h, and k_v are computed by binning over wave vectors in the usual way (e.g. Waite & Bartello, 2004; Waite, 2011; Kimura & Herring, 2012; Khani & Waite, 2013). Hyperviscosity simulations (i.e. figures 3.2a,b) have long tails for $k, k_h, k_v \gtrsim 100$, showing the hyperviscous dissipation range. The total wavenumber energy spectra are very similar to the vertical spectra except for the peak around the forcing wavenumber k_f, hence we will focus on $\langle E(k_h)\rangle$ and $\langle E(k_v)\rangle$.

The averaged vertical wavenumber spectra in all cases are peaked at $k_v \approx 20$ for $N = 2$ and $k_v \approx 40$ for $N = 6$, illustrating that the peak location changes with N. This behaviour is consistent with previous results which show that the characteristic vertical wavenumber is the buoyancy wavenumber $k_b = N/u_{rms}$, provided it is not in the dissipation range (e.g. Waite & Bartello, 2004; Waite, 2011, k_b is denoted by arrows in figure 3.2). The averaged vertical wavenumber spectrum is approximately flat up to the wavenumber in which the spectrum is peaked (as also seen in e.g. Herring & Métais, 1989; Waite & Bartello, 2004), beyond which it decays with a slope of around -2.4, -3.4, and -2.8 for the hyperviscosity simulation, the Smagorinsky LES, and the Kraichnan LES, respectively, when $N = 2$. Similarly, the vertical wavenumber spectrum decays with a slope of around -1.2, -3.8,

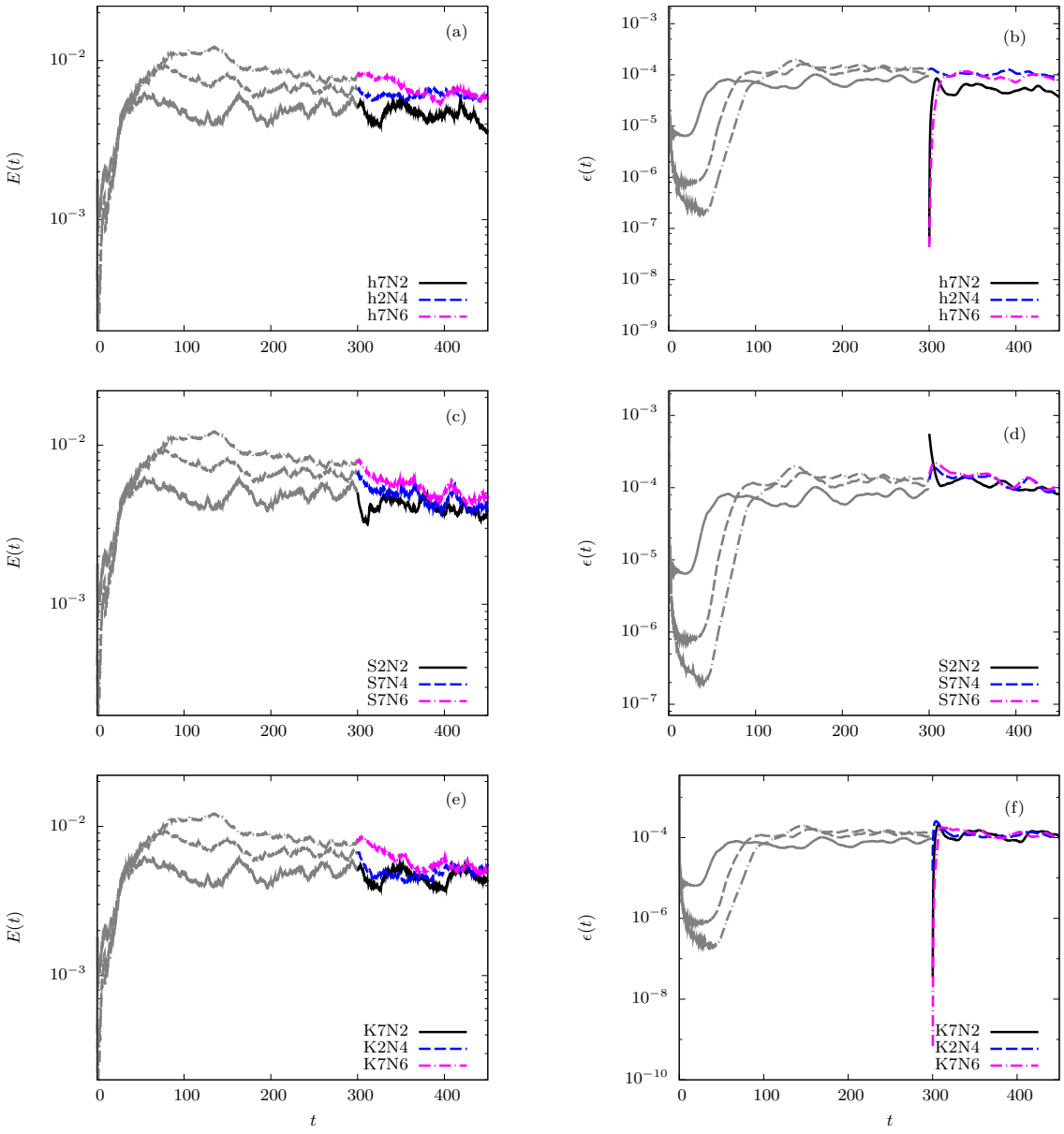

Figure 3.1: Time series of kinetic energy (left) and the kinetic energy dissipation rate (right) for (a,b) the hyperviscosity simulations, (c,d) the Smagorinsky LES, and (e,f) the Kraichnan LES. The gray curves over $0 \leq t \leq 300$ are the low resolution hyperviscosity simulations with the corresponding buoyancy frequency N.

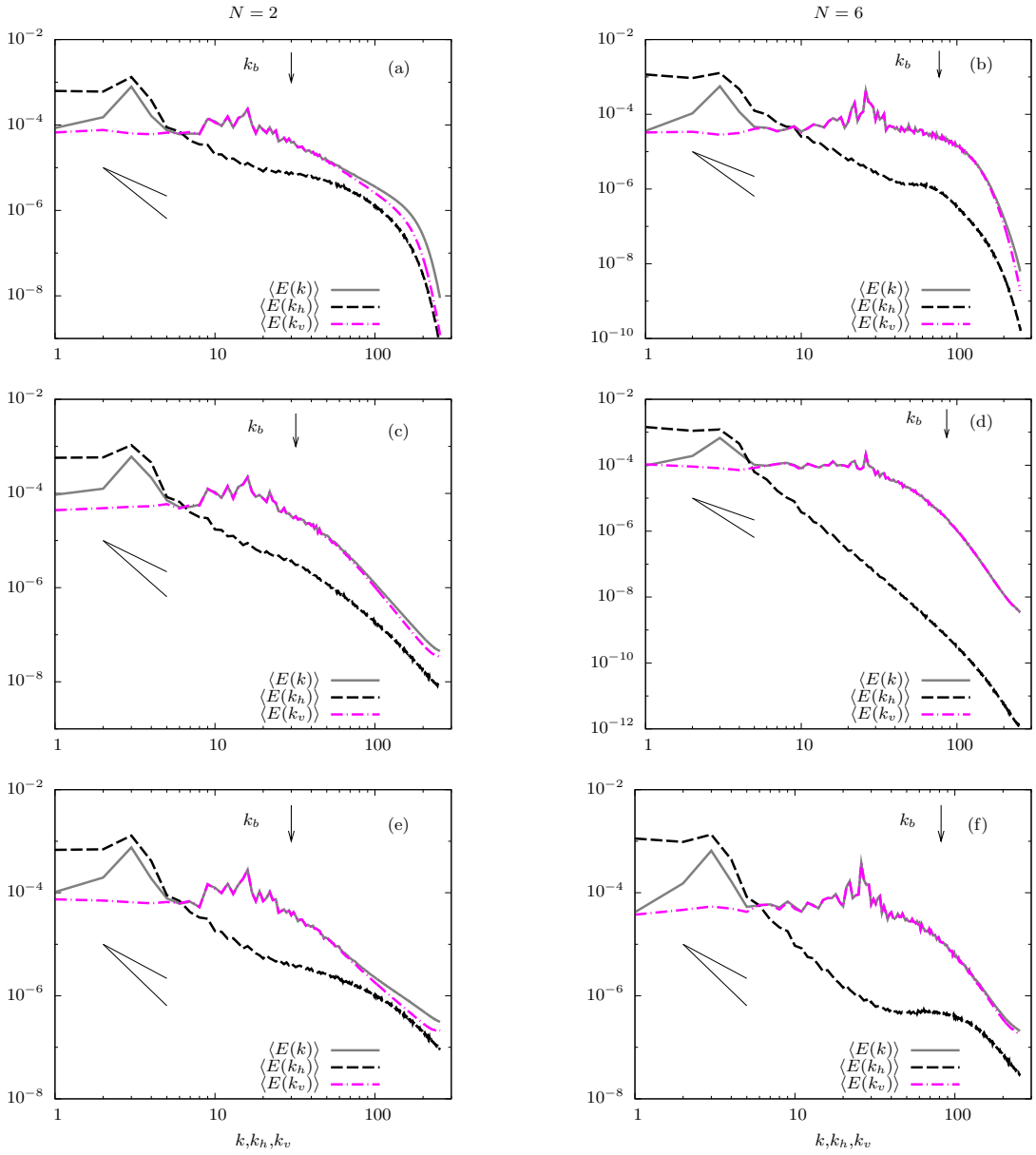

Figure 3.2: The averaged total, horizontal, and vertical wavenumber energy spectra with resolution $n = 768$ for (a,b) the hyperviscosity simulations, (c,d) the Smagorinsky LES, and (e,f) the Kraichnan LES, for $N = 2$ (left) and $N = 6$ (right). Spectra are averaged over $375 \leq t \leq 450$. Arrows correspond to the buoyancy wavenumber k_b and the forcing wavenumber is $k = 3$. The black solid line segments show $-5/3$ and -3 slopes.

and -2 for the hyperviscosity simulation, the Smagorinsky LES, and the Kraichnan LES, respectively, when $N = 6$. We use the least-squares method to measure spectral slopes over $40 \leq k_v \leq 100$.

The averaged horizontal wavenumber energy spectra are peaked around the forcing wavenumber $k_f = 3$. With hyperviscosity, the slope is around -1 for $N = 2$ and -2 for $N = 6$ (over $10 \leq k_h \leq 30$ and $10 \leq k_h \leq 50$, respectively). For the same ranges of k_h, the spectral slopes in the Smagorinsky LES are approximately -1.5 for $N = 2$ and -4 for $N = 6$ (figures 3.2c and d). Similarly, the Kraichnan LES gives slopes of -1.4 and -1.9 for $N = 2$ and $N = 6$, respectively (figures 3.2e and f). As a result, increased stratification steepens the spectra in the hyperviscosity simulations and the LES. In addition, at fixed resolution and N, different SGS models give different slopes; the Smagorinsky simulations are consistently steeper than those using the Kraichnan model. Overall, hyperviscosity and LES give slopes that are shallower than $-5/3$ for $N = 2$. For $N = 6$ however, slopes are steeper than $-5/3$. In addition, the averaged horizontal wavenumber energy spectra exhibit a bump at around the buoyancy wavenumber k_b (see arrows in figure 3.2) except for the Smagorinsky LES with $N = 6$ (figure 3.2d).

Figure 3.3 shows the horizontal and vertical wavenumber spectra of SGS energy transfer, i.e. eddy dissipation spectra (see Appendices B and C), for the low- and high-resolution Kraichnan and Smagorinsky LES at $t = 450$. Interestingly, for both SGS models, the maximum dissipation happens at large horizontal and small vertical scales, which show an anisotropic energy transfer from resolved scales towards SGS motions (similar trends are seen in the stratified SGS energy transfer spectra in DNS of Khani & Waite, 2013). As a result, although the Smagorinsky and Kraichnan eddy viscosities are defined isotropically, the SGS energy transfer spectra inherit the anisotropy of the resolved motions. For both high- and low-resolution cases, the Smagorinsky LES shows a larger peak in the horizontal wavenumber SGS energy transfer spectra, implying that the Smagorinsky model is much more dissipative than the Kraichnan model (figure 3.3). The same conclusions hold for the vertical wavenumber SGS energy transfer spectra as well. Meanwhile, the Kraichnan LES shows a cusp around k_c in the vertical SGS energy spectra and the high-resolution horizontal SGS spectra, implying that the Kraichnan model is more consistent with the DNS of Khani & Waite (2013). In addition, the horizontal and vertical SGS energy transfer spectra for the low-resolution Kraichnan case with $N = 2$ are remarkably similar to those of the corresponding high-resolution Smagorinsky LES far from the cutoff wavenumber k_c. As a result, the non-local horizontal and vertical SGS energy transfers in the high-resolution Smagorinsky LES are very similar to those of the low-resolution Kraichnan model.

To make a quantitative comparison of the SGS terms from the two LES approaches, the effective spectral eddy viscosity of the Smagorinsky LES at $t = 450$ is shown in figure

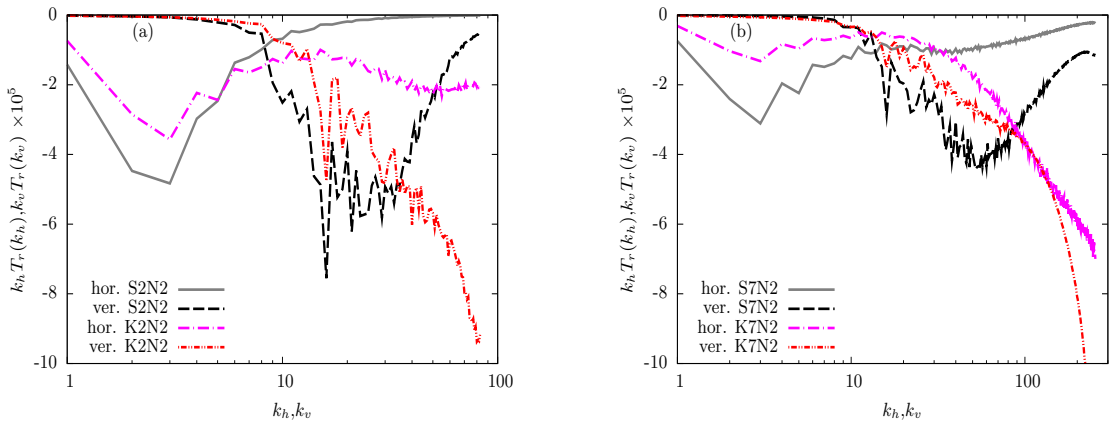

Figure 3.3: The horizontal and vertical wavenumber spectra of SGS energy transfer for the Smagorinsky and Kraichnan LES at $t = 450$. Low- and high-resolution cases are shown in panels (a) and (b), respectively. The spectra are multiplied by wavenumber in order to preserve area on the log-linear axes.

3.4. We compute $\nu_r(k)$ by diving the absolute value of the spherical SGS energy transfer $T_r(k)$ of the Smagorinsky LES by $2k^2E(k)$. There is a broad range of k/k_c with a plateau of almost constant $\nu_r(k)$, and no cusp is seen around $k = k_c$. The effective spectral eddy viscosity from the Smagorinsky model is quite different from actual effective eddy viscosity measured in high-resolution DNS of stratified turbulence, in which a cusp around the cutoff wavenumber k_c is a dominant feature (Khani & Waite, 2013). For comparison, the Kraichnan eddy viscosity $\nu_e(k)$ for the case with $n = 256$ and $N = 2$ is also shown in figure 3.4; it exhibits a lower plateau and a large cusp, in better agreement with DNS of Khani & Waite (2013). The plateau in the low-resolution Smagorinsky case is almost three times larger than the Kraichnan plateau. Interestingly, the low-resolution Kraichnan plateau is very close to the plateaus of the high-resolution Smagorinsky simulations. These results are consistent with the energy and eddy dissipation spectra, which show that the Smagorinsky model is much more dissipative than the Kraichnan model.

Figure 3.5 shows compensated horizontal energy spectra (in which the horizontal spectra are normalized by $k_h^{-5/3}\langle\epsilon\rangle^{2/3}$) for the hyperviscosity simulations and LES when $N = 2$, 4, and 6. As in figure 3.2, arrows show the location of the buoyancy wavenumber k_b. In figure 3.5(a), the compensated horizontal wavenumber energy spectrum for the high-resolution hyperviscosity case is almost constant for $6 \lesssim k_h \lesssim 30$, which is consistent with an inertial subrange with a slope close to $-5/3$. A bump is visible at $k_h \approx 30$, which

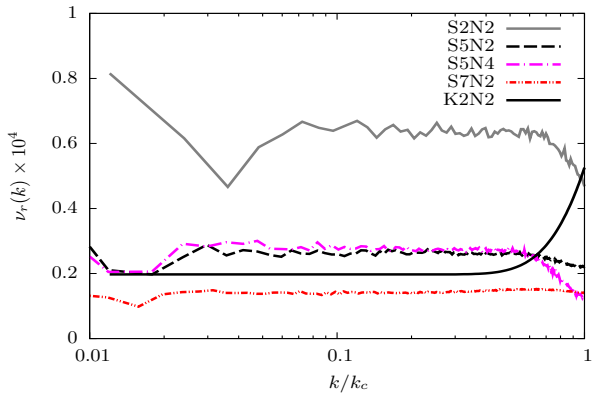

Figure 3.4: Effective spectral eddy viscosity for the Smagorinsky cases along with the Kraichnan eddy viscosity ν_e for the low resolution case with $N = 2$. For computing eddy viscosities, results at $t = 450$ are used; and the horizontal axis is normalized by the cutoff wavenumber k_c.

is around the buoyancy wavenumber k_b. Similar bumps have been investigated in recent hyperviscosity simulations and DNS (Laval et al., 2003; Waite, 2011; Augier et al., 2012; Waite, 2014). A similar constant inertial subrange and bump at $k_h \sim k_b$ are also seen in the other simulations in figure 3.5a except for the low-resolution Smagorinsky LES. Interestingly, the Smagorinsky spectrum with $n = 768$ looks very similar to the Kraichnan spectrum with $n = 256$; the inertial range slope and amplitude, and the bump near k_b, are nearly identical. In other words, the low-resolution Kraichnan simulation reproduces the higher-resolution Smagorinsky simulation, despite having a grid spacing three times as coarse.

The results with higher stratification are similar. For $N = 4$ (figure 3.5b) an almost flat inertial subrange over $6 \lesssim k_h \lesssim 50$ is seen for the high-resolution hyperviscosity case, which is followed by a bump at around $k_h = 60$ (very close to k_b). Other simulations in this panel, except the low-resolution hyperviscosity case (i.e. h2N4) and the middle-resolution Smagorinsky case (i.e. S5N4), show a very short inertial subrange along with a little bump at around k_b. Once again, the high-resolution Smagorinsky spectrum looks like the low-resolution Kraichnan up to $k_h \approx 30$. In figure 3.5(c), the high-resolution hyperviscosity and Kraichnan cases with $N = 6$ show the constant inertial subrange at $6 \lesssim k_h \lesssim 60$ and a bump at $k_h \sim k_b$. However, other simulations in this panel show a very steep compensated spectrum. Like in figures 3.5(a,b), figure 3.5(c) demonstrates that the low-resolution Kraichnan LES looks like the high-resolution Smagorinsky LES. In

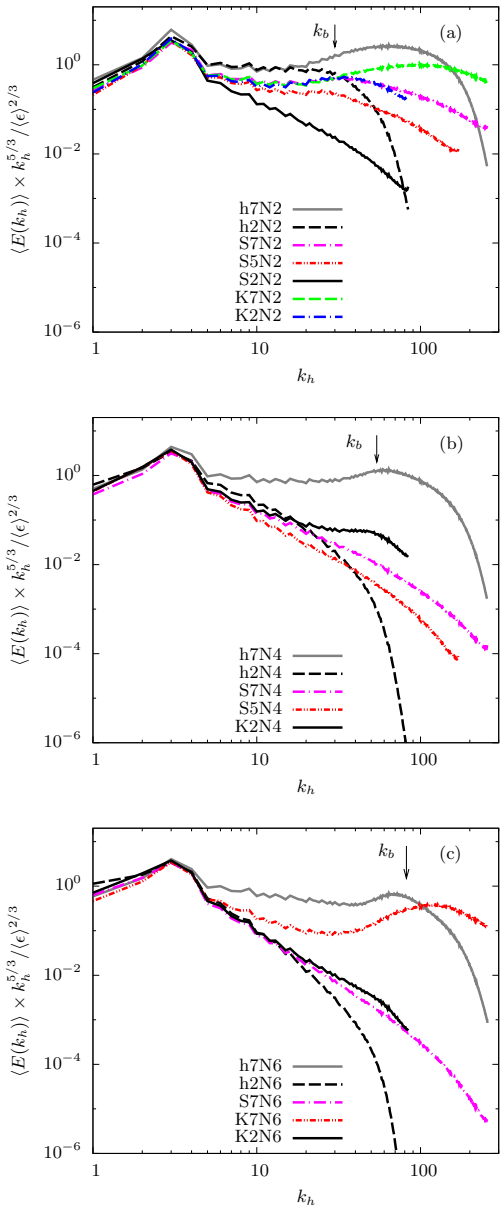

Figure 3.5: The averaged compensated horizontal energy spectra: (a) $N = 2$, (b) $N = 4$, and (c) $N = 6$. Spectra are averaged over $375 \leq t \leq 450$. Arrows correspond to the buoyancy wavenumber k_b and the forcing wavenumber is at $k = 3$.

addition, the hyperviscous simulation is more dissipative than the Kraichnan LES at very large wavenumbers (figure 3.5). At large wavenumbers, i.e. $k \gtrsim 100$, the effective eddy viscosity given by the hyperviscosity $\nu_m k^{2m-2}$ is larger than ν_e, hence the hyperviscosity simulation is more strongly damped at large k. As a result, the Kraichnan LES seems to give more reasonable results compared with hyperviscosity at very large wavenumbers. In addition, the potential energy spectra (not shown here) also show peaks and bumps around k_b in the vertical and horizontal wavenumber spectra, respectively.

3.4.3 KH instabilities and the Richardson number

Figure 3.6 shows the $y-$component of vorticity $\bar{\omega}_y = (\partial\bar{u}/\partial z - \partial\bar{w}/\partial x)$ on the x-z plane at $y = 0.25$ and $t = 450$ for the high-resolution Kraichnan LES. Vortices are lengthened in the horizontal direction and layered in the vertical. For the lower stratification (figure 3.6a), intermittent instabilities and KH billows are visible between the layers. Stronger stratification (figure 3.6b) shows a more strongly layered structure with fewer regions of KH instability. Figure 3.7 shows $\bar{\omega}_y$ for the high-resolution Smagorinsky LES. As in the Kraichnan LES, the lower stratification (figure 3.7a) shows a layered vertical structures with KH instabilities. No instabilities are visible in the more strongly stratified case (figure 3.7b). According to figures 3.6 and 3.7, increased stratification at fixed resolution and SGS scheme inhibits KH instabilities, since the thinner layers in the more strongly stratified case are more influenced by dissipation (Hebert & de Bruyn Kops, 2006a; Brethouwer et al., 2007). In addition, KH instabilities are inhibited in the Smagorinsky simulation relative to the Kraichnan and hyperviscosity cases at the same stratification and resolution, suggesting that the Smagorinsky case is the most dissipative.

The above results suggest that there is a bump around k_b in the horizontal wavenumber energy spectrum only when KH instabilities are visible in the vorticity plots. This hypothesis has been proposed in several studies (Laval et al., 2003; Waite, 2011; Augier et al., 2012; Waite, 2014). To further investigate this relationship in LES and to investigate the influence of different SGS models, we consider the Richardson number in our simulation. The Richardson number shows the competition between stratification, which stabilizes flow, and the vertical shear of horizontal motions, which excites instabilities. The local Richardson number is given as follows

$$Ri = \frac{N^2 - \frac{g}{\rho_0}\frac{\partial\bar{\rho}}{\partial z}}{\left(\frac{\partial\bar{u}}{\partial z}\right)^2 + \left(\frac{\partial\bar{v}}{\partial z}\right)^2}, \tag{3.34}$$

in which the numerator is the buoyancy frequency squared from the total (background plus perturbation) density; and g and ρ_0 are gravity and the reference density, respectively. The

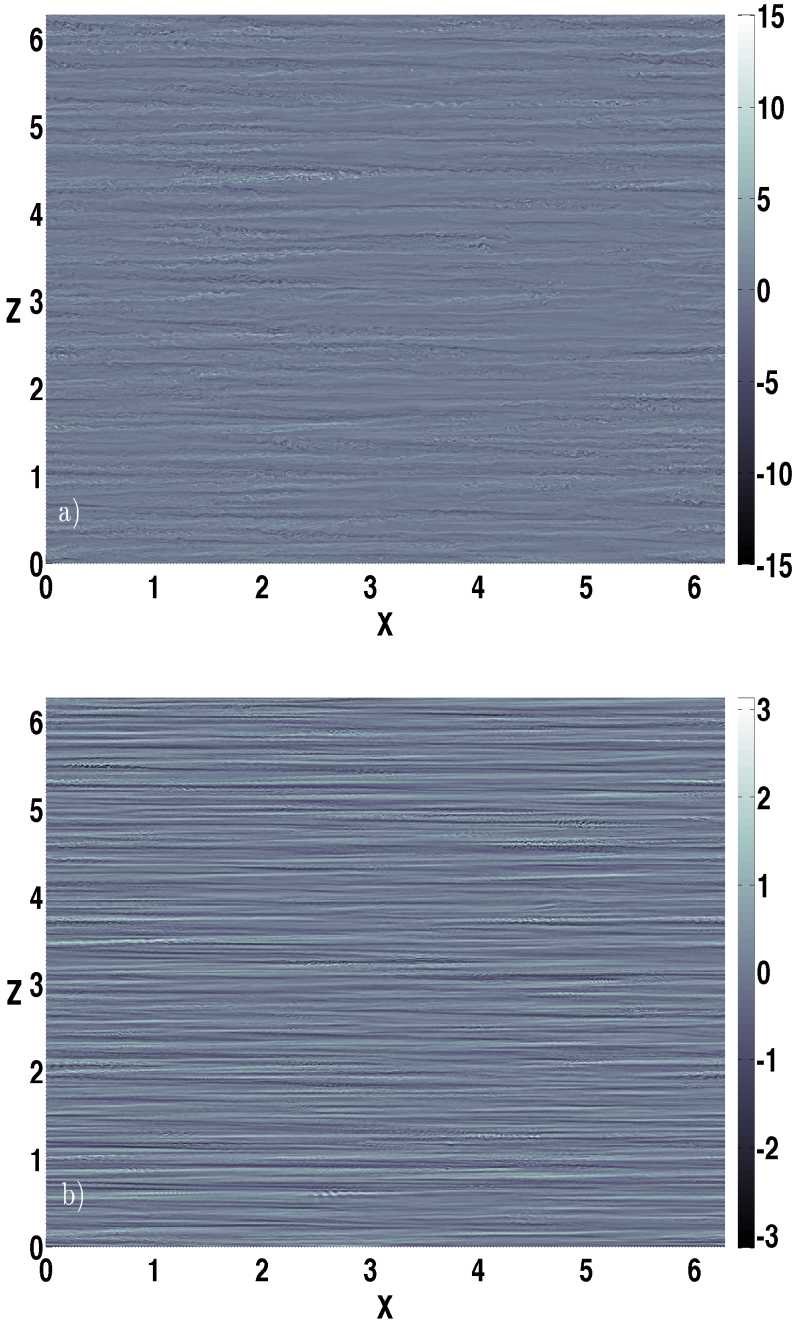

Figure 3.6: Vorticity field in y-direction, $\bar{\omega}_y$, on the x-z plane at $y = 0.25$ and $t = 450$ for the high resolution Kraichnan LES: (a) $N = 2$, and (b) $N = 6$. Vorticity fields are normalized by the corresponding buoyancy frequency N.

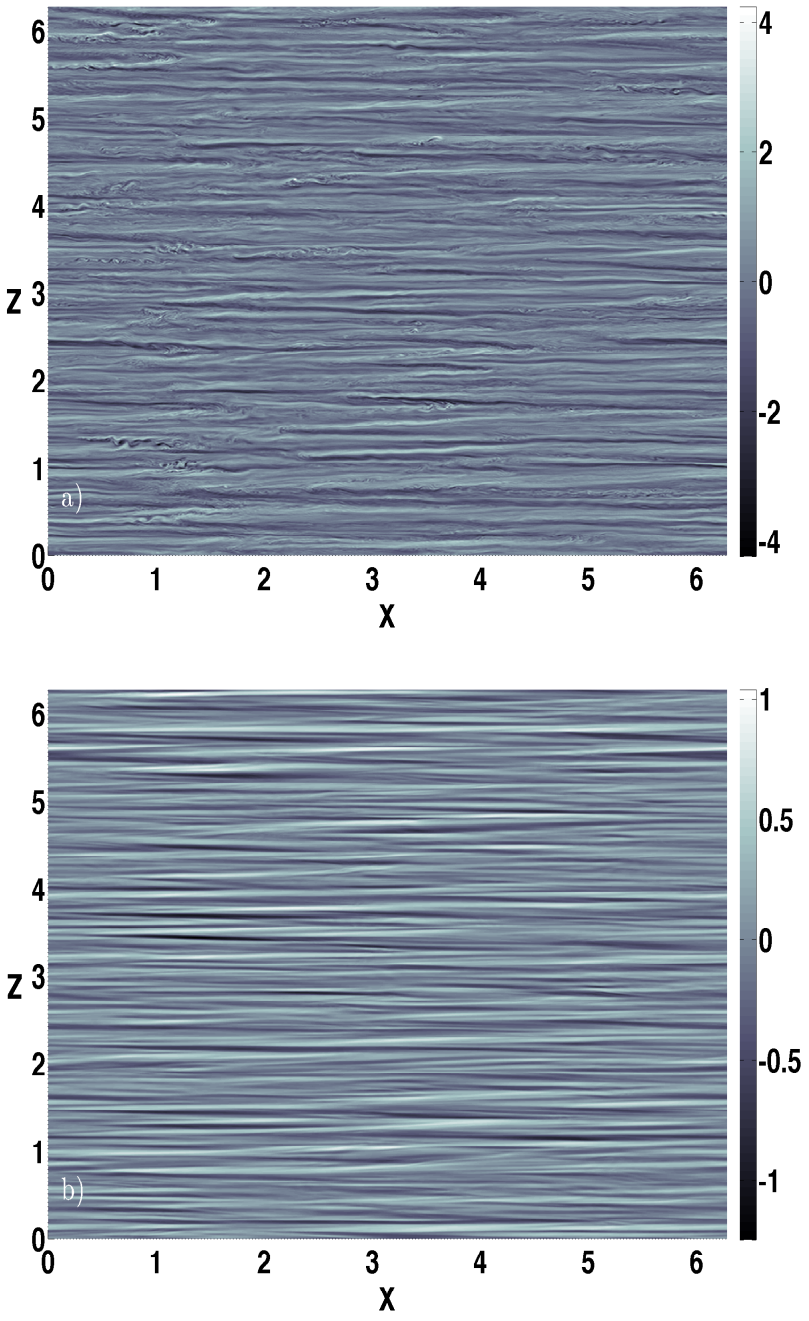

Figure 3.7: Vorticity field in y-direction, $\bar{\omega}_y$, on the x-z plane at $y = 0.25$ and $t = 450$ for the high resolution Smagorinsky LES: (a) $N = 2$, and (b) $N = 6$. Vorticity fields are normalized by the corresponding buoyancy frequency N.

classical necessary condition for instability $Ri < 1/4$ is strictly applicable only for parallel shear flow, but is nevertheless commonly employed to diagnose regions of KH instabilities in more complicated flows (e.g. Riley & de Bruyn Kops, 2003; Augier & Billant, 2011, which considered decaying stratified turbulence and breakdown of vortex, respectively). As a result, we consider the structure and distribution of Ri - with the understanding that more points with $Ri < 1/4$ might suggest more regions with KH instabilities. Furthermore, $Ri < 0$ implies overturning. The vorticity plot shows a large-scale layered structure with intermittent smaller-scale structures (e.g. figure 3.7a). Small-scale vorticity structures correspond to regions with small Ri, < 0.25 and in many cases < 0 (see the Ri field in figure 3.8), consistent with KH instabilities in different stages of evolution, as has been discussed elsewhere (e.g. Riley & de Bruyn Kops, 2003). Figure 3.8 shows the local Richardson number in x-z plane for the high-resolution Smagorinsky simulation with $N = 2$ (where the vorticity plot for that is shown in figure 3.7a). We have shown only Ri values between $-1/4$ to 1. Intermittent spots with red and light-blue colours correspond to regions with $Ri < 1/4$, which show high shear between the layers. This figure shows that the small-scale disturbances in the vorticity field, many of which resemble KH instabilities, are colocated with regions of small $Ri < 1/4$, including many points with $Ri < 0$.

For an overview of the Richardson number in all simulations, figure 3.9 shows histograms of Ri for the LES at $t = 450$. For clarity, only the range $-10 \leq Ri \leq 30$ is shown. Figure 3.9 presents results for different resolutions, SGS models, and buoyancy frequencies. Decreasing the resolution from $n = 768$ to 256 causes the histograms to drop off rapidly for negative Ri and causes the peak around $Ri = 0$ to decrease. In addition, the Richardson number histogram show a long positive tail. Figure 3.9 shows that at fixed resolution, increased stratification reduces the numbers of points with negative Ri and decreases the peak around $Ri = 0$, e.g. see the high-resolution Kraichnan case with $N = 2$ (the solid green line) versus that with $N = 6$ (the solid brown line), or the high-resolution Smagorinsky case with $N = 2$ (the dashed green line) versus that with $N = 6$ (the dash dotted blue line). Furthermore, in the low-resolution Kraichnan case with $N = 6$ (i.e. K2N6), overturning is completely suppressed because there are no points with negative Ri. As a result, by decreasing the resolution or increasing the stratification, the number of points with negative Ri decreases, and regions of small-scale instability and overturning are eliminated (e.g. figure 3.7b). In addition, at fixed resolution and buoyancy frequency, different SGS models result in different Richardson number histograms. For example, the high-resolution Kraichnan case with $N = 2$ has a larger numbers of negative Ri and a smaller numbers of positive Ri compared with the high-resolution Smagorinsky case with $N = 2$, implying that the latter case is more stabilizing than the former one. Similar behaviours are seen in low-resolution cases with $N = 2$ or high-resolution cases with $N = 6$. It is

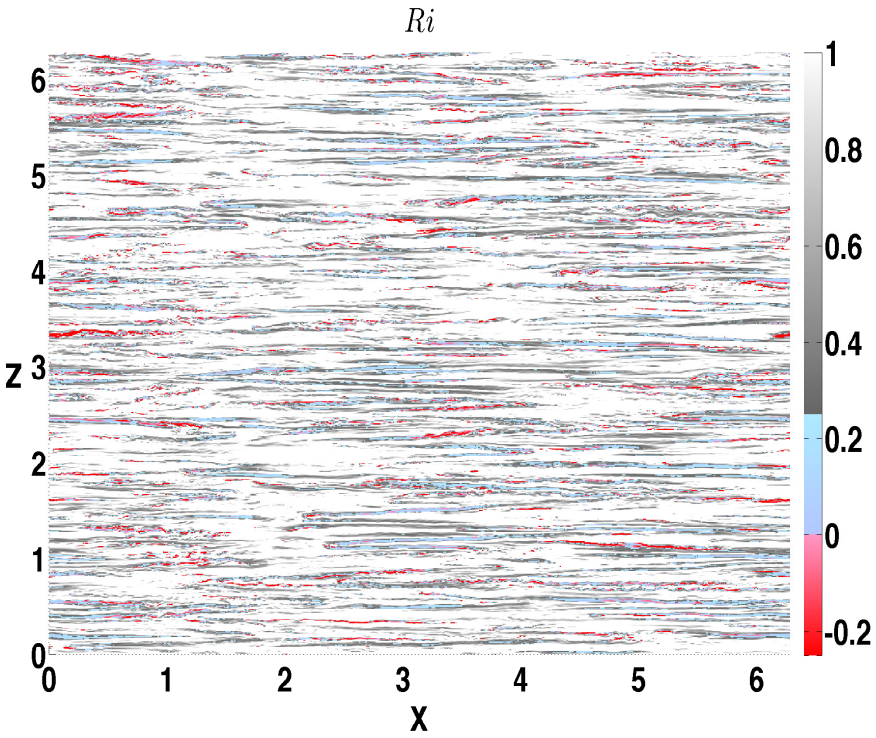

Figure 3.8: The local Richardson number Ri field on the x-z plane at $y = 0.25$ and $t = 450$ for the Smagorinsky case with $N = 2$ and $n = 768$. The Richardson number values are restricted between -0.25 and 1.

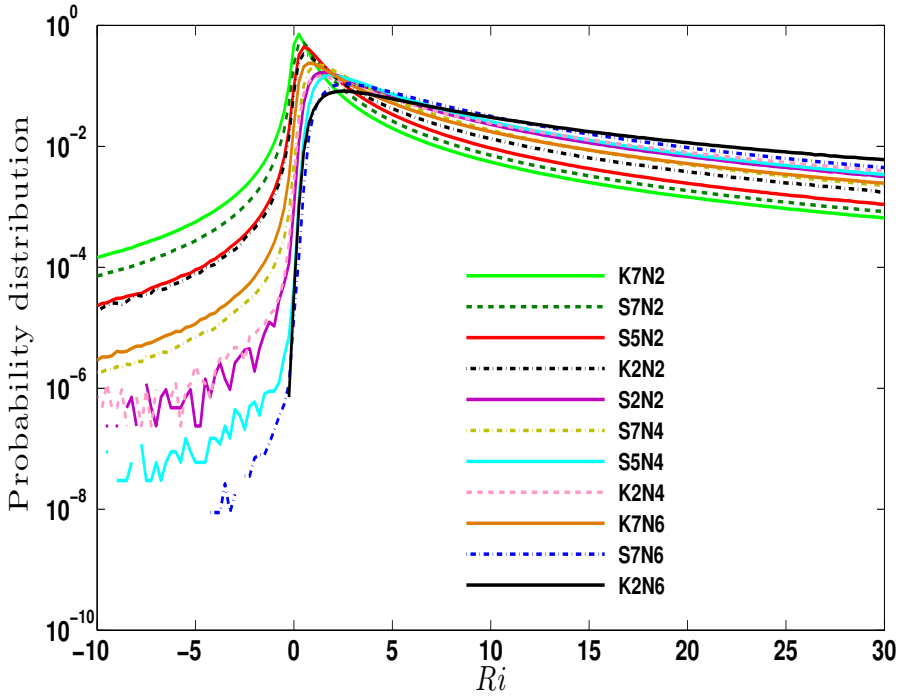

Figure 3.9: Histograms of the local Richardson number Ri at $t = 450$. Only the segment $-10 \leq Ri \leq 30$ is shown. Histograms are normalized by bin size to give probability distributions, and are computed with 1000 bins over $-50 < Ri < 200$ ($\Delta Ri = 0.25$).

interesting to mention that the Ri histograms of the low-resolution Kraichnan case with $N = 2$ and $n = 256$ are very similar to the higher-resolution Smagorinsky cases with $N = 2$ and $n = 512$. Similarly, the Ri histogram of Kraichnan cases with $N = 6$ and $n = 256$ are very close to that of Smagorinsky with $N = 6$ and $n = 768$. Overall, the Smagorinsky LES seems much more dissipative than the Kraichnan model, since small-scale instabilities and overturning is suppressed significantly.

Figure 3.10 shows the fraction of the domain with $Ri < 0$ as a function of k_c/k_b for the Smagorinsky and Kraichnan cases. Increased k_c/k_b at fixed resolution leads to more grid points with negative Richardson numbers (similar trends are also seen for the number of grid points with $0 < Ri < 0.25$; not shown). As a result, increased resolution at fixed stratification or decreased stratification at fixed resolution generates more overturning regions and small-scale instabilities. Even at fixed k_c/k_b, the overturning fractions depends

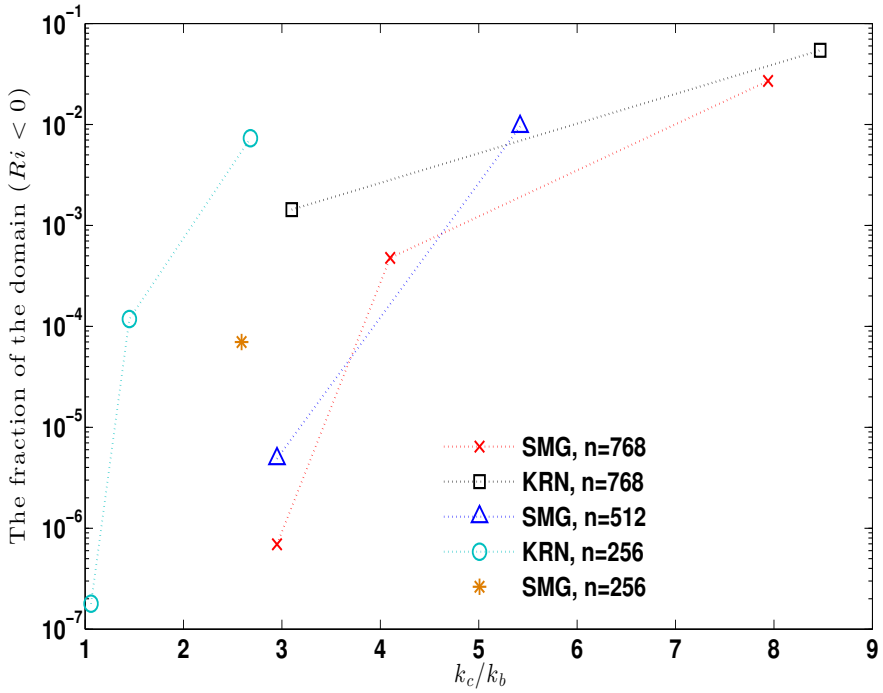

Figure 3.10: The fraction of the domain with $Ri < 0$ as a function of the ratio k_c/k_b for the Smagorinsky and Kraichnan LES at different resolutions.

on resolution, with higher resolution yielding smaller fractions. In addition, figure 3.10 also demonstrates that the fraction of the domain with $Ri < 0$ is higher for the Kraichnan LES comparing with the Smagorinsky case at the same resolution.

3.4.4 Discussion

In this section, we discuss the LES results inferred from §3.4.1, 3.4.2, and 3.4.3. First, we summarize the important points from the previous sections:

- The horizontal vorticity field shows regions of small-scale instabilities and turbulence for the high-resolution Kraichnan and Smagorinsky cases with $N = 2$ (figures 3.6a and 3.7a). Increased stratification stabilizes the flows, such that no instabilities are

seen in for example the high-resolution Smagorinsky simulation with $N = 6$ (figure 3.7b). In addition, these regions of instabilities correspond to regions with small or negative Ri (figure 3.8).

- The compensated horizontal energy spectra show an approximately $-5/3$ inertial subrange along with a bump at $k_h \sim k_b$ in the high-resolution Kraichnan and Smagorinsky simulations with $N = 2$ and the high-resolution Kraichnan case with $N = 2$, but not for the high-resolution Smagorinsky case with $N = 6$ (figure 3.5). Increasing the grid spacing shortens the inertial subrange and seems to suppress the bump at k_b.

- Larger numbers of negative Ri are seen in histograms of the local Richardson number in the high-resolution Kraichnan and Smagorinsky simulations with $N = 2$ (figures 3.9 and 3.10). Increased stratification causes a rapid drop in points with negative Ri, e.g. the high-resolution Smagorinsky case with $N = 6$. Increasing the grid spacing also leads to a significant decrease in the histogram of negative Ri.

Our numerical experiments show that if the grid spacing is fine enough to capture the bump in the horizontal wavenumber spectrum, then KH instabilities and small and negative Ri are more likely to happen in physical space. This critical resolution seems to depend on L_b and is different for the different SGS models. Table 3.2 shows the ratio of k_c/k_b and Δ/L_b for the Smagorinsky and Kraichnan SGS simulations. According to the energy spectra in figures 3.2 and 3.5 and the Ri histograms in figure 3.9, the Smagorinsky LES captures small-scale KH instabilities, indicated by a spectral bump near $k_h \sim k_b$ and points with small and negative Ri, for all cases except for the low-resolution case with $N = 2$, the middle-resolution case with $N = 4$, and the high-resolution case with $N = 6$. By contrast, the Kraichnan simulations capture this behaviour for all cases except the low-resolution case with $N = 6$. For the low-resolution Kraichnan case with $N = 4$, there is a visible bump in figure 3.5(b), but very few points with small and negative Ri are seen in figure 3.9. This discrepancy could be due to sampling, since the spectra in figure 3.5(b) are averaged over $375 \leq t \leq 450$, while this histogram of Ri is instantaneous at $t = 450$. As a result, the minimum resolution for the Smagorinsky simulations is inside the range $0.12L_b \leq \Delta < 0.17L_b$ and for the Kraichnan simulations is inside the range $0.34L_b \leq \Delta < 0.47L_b$. Hence, the Smagorinsky LES needs to have k_c/k_b almost three times larger than Kraichnan to resolve KH instabilities. We emphasize that both SGS models have to resolve L_b to capture the dynamics of stratified turbulence, but the

Smagorinsky model must resolve L_b almost three times better than Kraichnan. Of course, the Kraichnan model only works with spectral methods, but for such simulations, it is a much better choice than the Smagorinsky model.

3.5 Conclusion

LES of forced stratified turbulence with different resolutions, buoyancy frequencies, and SGS models are studied in this paper. The averaged dissipation rates are almost identical for the Smagorinsky and Kraichnan LES, confirming that $\langle\epsilon\rangle$ depends on the large scales. The averaged vertical energy spectra are flat up to a certain vertical wavenumber, which depends on the buoyancy frequency N. The averaged horizontal energy spectra depends on the grid spacing and if Δ is small enough, the spectra have an almost $-5/3$ slope along with a bump at $k_h \sim k_b$. These spectra are in line with previous work on stratified turbulence using regular or hyper- viscosity (e.g. Waite & Bartello, 2004; Lindborg, 2006; Brethouwer et al., 2007; Waite, 2011; Augier et al., 2012; Waite, 2014). Increased resolution or decreased stratification promotes KH instabilities between vertical layers. Stronger stratification or smaller k_c inhibits these instabilities by shrinking the layer thickness towards the dissipation scale or by increasing the dissipation scale, respectively. These findings are reminiscent of the Re_b criterion for DNS: stronger stratification requires higher resolution, and hence larger effective Reynolds number, to fully capture the dynamics of stratified turbulence.

We present a threshold on the grid spacing Δ for which dynamics of stratified turbulence are captured in LES. Our results show that the Smagorinsky LES needs much smaller (three times) Δ/L_b compared with the Kraichnan simulations, in order to reproduce the bump in the horizontal wavenumber spectrum and the associated regions of small and negative Ri. In addition, at large wavenumbers, the hyperviscosity simulation is more dissipative than the Kraichnan LES with the same resolution. Therefore, for k_b close to k_{max} and k_c, the Kraichnan LES seems to get reasonable results compared to hyperviscosity, where the former captures the bump in the horizontal energy spectrum but the latter does not (e.g. low-resolution hyperviscosity with $N = 4$ versus low-resolution Kraichnan with $N = 4$ in figure 3.5b). These SGS models are isotropic and they clearly fail when $\Delta > L_b$ where the turbulence is strongly anisotropic. Interestingly, classical theory predicts isotropy below the Ozmidov scale L_o rather than the buoyancy scale L_b, but nevertheless, these isotropic SGS models work well for Δ sufficiently less than L_b but still greater than L_o.

For future work, the performance of LES models beyond the Smagorinsky and Kraichnan schemes should be investigated for stratified turbulence. In particular, the dynamic Smagorinsky model (Germano et al., 1991) in which c_s is not constant, has the potential to

improve the disappointing performance of the Smagorinsky model seen in this study. Since the dynamics model determines c_s locally and with respect to the dynamics of the structures of flows, it might show better performance than the Smagorinsky model at low resolution, and hence decrease the computational costs. Meanwhile, considering anisotropic eddy viscosity terms, in which the horizontal and vertical deformations are considered separately, is another potential avenue for further work. In addition, we need to ultimately perform very high-resolution DNS of stratified turbulence that resolves a large inertial subrange to obtain a more fundamental understanding of the energy transfer between large and small scales.

3.6 Acknowledgments

Computations were performed on the gpc supercomputer at the SciNet HPC Consortium. SciNet is funded by: the Canada Foundation for Innovation under the auspices of Compute Canada; the Government of Ontario; Ontario Research Fund – Research Excellence; and the University of Toronto. Also, this work was made possible by the facilities of the Shared Hierarchical Academic Research Computing Network (SHARCNET: www.sharcnet.ca) and Compute/Calcul Canada. In addition, computing resources from the Mathematics Faculty Computing Facility of the University of Waterloo are gratefully appreciated. Financial support from the Natural Sciences and Engineering Research Council of Canada is gratefully acknowledged.

Chapter 4

Large eddy simulations of stratified turbulence: the dynamic Smagorinsky model

The dynamic Smagorinsky model for LES of forced stratified turbulence is studied in this chapter. A minimum grid spacing criterion of $\Delta/L_b < 0.24$ is suggested for capturing dynamical features of stratified turbulence using the dynamic Smagorinsky model. Our results show that the dynamic Smagorinsky model needs a grid spacing Δ that is approximately twice as large as the regular Smagorinsky model to reproduce similar results. Statistics of the dynamic Smagorinsky coefficient c_s are also investigated: its distribution is peaked around zero and its standard deviations decrease slightly with increased stratification. In addition, it is shown that regions of increased shear favour smaller c_s values.

This chapter is based on the submitted paper, Khani S. and M. L. Waite. Large eddy simulations of stratified turbulence: the dynamic Smagorinsky model. Submitted to *J. Fluid Mech.* 2014.

4.1 Introduction

An alternative approach to direct numerical simulations (DNS) is large-eddy simulations (LES), in which scales larger than the grid spacing Δ are resolved, but subgrid scale (SGS) effects are parametrized. A common and practical SGS scheme is the Smagorinsky (1963) model, in which the deviatoric part of the SGS momentum tensor $\boldsymbol{\tau}^r$ is expressed in terms of the filtered rate of strain $\bar{s}_{ij} = 1/2(\partial\bar{u}_i/\partial x_j + \partial\bar{u}_j/\partial x_i)$, as follows (using the notation of Pope, 2000)

$$\tau^r_{ij}(\boldsymbol{x}, t) = -2\nu_r(\boldsymbol{x}, t)\bar{s}_{ij}(\boldsymbol{x}, t), \tag{4.1}$$

where $\bar{\boldsymbol{u}} = (\bar{u}, \bar{v}, \bar{w})$ is the filtered velocity field. The eddy viscosity coefficient $\nu_r(\boldsymbol{x}, t)$ is defined by the following model

$$\nu_r = c_s\Delta^2\bar{S}, \tag{4.2}$$

where c_s is the Smagorinsky coefficient, and $\bar{S} = (2\bar{s}_{ij}\bar{s}_{ij})^{1/2}$. (Here, we define c_s without the squared power as in e.g. Germano, 1992; Ghosal et al., 1995; Pope, 2004) A constant value of $c_s \approx (0.17)^2$, which was suggested by Lilly (1967), did not work particularly in complex turbulent flows; as a result, Siegel & Domaradzki (1994) investigated various ranges of c_s from $(0.13)^2$ to $(0.24)^2$ for different turbulent flows. Indeed, there is not a clear approach for selecting c_s in complex turbulent flows. The dynamic Smagorinsky model is a method proposed by Germano et al. (1991), in which a time- and spatially-varying c_s is computed by applying a second filter $\tilde{\Delta}$ and assuming a self-similar inertial subrange between two filter scales. An improvement by Lilly (1992) yielded a method to find c_s using the resolved fields.

In the last few years, due to the high cost of DNS (e.g. Almalkie & de Bruyn Kops, 2012; Bartello & Tobias, 2013), there has been increased interest in using LES for computational studies of stratified turbulence (e.g. Remmler & Hickel, 2012; Paoli et al., 2013; Khani & Waite, 2014a). In stratified turbulence, we also need to model the SGS density flux $\boldsymbol{h}$, which is related to the filtered perturbation density $\bar{\rho}(\boldsymbol{x}, t)$ as

$$h_j(\boldsymbol{x}, t) = -\frac{2}{Pr_t}\nu_r(\boldsymbol{x}, t)\frac{\partial\bar{\rho}(\boldsymbol{x}, t)}{\partial x_j}, \tag{4.3}$$

where Pr_t is the turbulent Prandtl number. Khani & Waite (2014a) have investigated the performance of two classical LES approaches, the Smagorinsky (1963) and Kraichnan (1976) models, in LES of stratified turbulence where the filter width Δ is larger than the

Ozmidov scale. This study found a necessary criteria on Δ for LES to capture the fundamental dynamics of stratified turbulence, including a cascade to small scales (Lindborg, 2006), and a breakdown of the layerwise structure into Kelvin-Helmholtz (KH) instabilities (Laval et al., 2003; Waite, 2011; Khani & Waite, 2014a). These criteria are related to the buoyancy scale

$$L_b = 2\pi \frac{u_{rms}}{N}, \tag{4.4}$$

where u_{rms} is the root-mean-square velocity and N is the buoyancy frequency. As concluded by Khani & Waite (2014a), the performance of the Smagorinsky model in LES of stratified turbulence is disappointing since it requires three times the resolution compared to the Kraichnan model in order to adequately capture the dynamics of stratified turbulence ($\Delta/L_b < 0.17$ for the Smagorinsky LES versus 0.47 for the Kraichnan LES). On the other hand, the applicability of the Kraichnan LES in limited to idealized periodic boundary conditions, which might not be appropriate for turbulent flows near boundaries or in complex geometries.

Despite its popularity for geophysical flows, problems with the Smagorinsky model, including excessive dissipation near the filter scale, are widely known (Germano et al., 1991; Ghosal et al., 1995; Meneveau &, Katz 2000; Pope, 2000). In other fields like engineering flows, wall turbulence and boundary layers, the dynamic Smagorinsky model is much more widely used (e.g. Meneveau &, Katz 2000; Pope, 2000; Jiménez & Moser, 2000), but its applicability to stratified turbulence has not been investigated. In this paper, we perform and analyze LES of stratified turbulence using the dynamic Smagorinsky model, in which the main goal is to decrease the computational costs of the Smagorinsky model in resolving the dynamics of stratified turbulence. We investigate the maximum filter scale Δ that captures the fundamental dynamics of stratified turbulence, including a cascade to small scales and breakdown of layers into KH instabilities. Also, we investigate the anisotropy of the SGS energy transfer, the statistics c_s at different buoyancy frequencies and numerical resolutions, and the relationship between c_s and the resolved dynamics.

In §4.2, background on stratified turbulence and the dynamic Smagorinsky model are reviewed. The numerical approach and methodology are described in §4.3. Section 4.4 presents results, and conclusions are given in §4.5.

4.2 Background

The non-dimensional filtered Navier-Stokes equations under the Boussinesq approximation are

$$\frac{\partial \bar{u}_i}{\partial t} + \frac{\partial}{\partial x_j}(\bar{u}_i \bar{u}_j) = -\frac{\partial \bar{p}}{\partial x_i} - \frac{1}{{Fr_\ell}^2}\bar{\rho}\boldsymbol{e}_z - \frac{\partial \tau^r_{ij}}{\partial x_j} + \bar{f}_i, \tag{4.5}$$

$$\frac{\partial \bar{u}_j}{\partial x_j} = 0, \tag{4.6}$$

$$\frac{\partial \bar{\rho}}{\partial t} + \frac{\partial}{\partial x_j}(\bar{\rho}\bar{u}_j) - \bar{w} = -\frac{\partial h_j}{\partial x_j}, \tag{4.7}$$

where p and $\boldsymbol{f}$ are the perturbation pressure and velocity forcing fields, respectively; and the Froude number $Fr_\ell = u/N\ell$ is defined based on a velocity scale u and a length scale ℓ. We neglect the molecular viscosity and diffusion because of the assumption of large Reynolds number.

The dynamic Smagorinsky model applies a second test filter $\tilde{\Delta} > \Delta$ to the momentum equation (4.5). It is common to choose $\tilde{\Delta} = 2\Delta$ (e.g. Meneveau &, Katz 2000; Pope, 2000). The test-filtered momentum equation is given by (e.g. Pope, 2000)

$$\frac{\partial \tilde{\bar{u}}_i}{\partial t} + \frac{\partial}{\partial x_j}(\tilde{\bar{u}}_i \tilde{\bar{u}}_j) = -\frac{\partial \tilde{\bar{p}}}{\partial t} - \frac{1}{{Fr_\ell}^2}\tilde{\bar{\rho}}\boldsymbol{e}_z - \frac{\partial T^r_{ij}}{\partial x_j} + \tilde{\bar{f}}_i, \tag{4.8}$$

where $T^r_{ij} = T_{ij} - 1/3 T_{rr}\delta_{ij}$, and

$$T_{ij} = \widetilde{\overline{u_i u_j}} - \tilde{\bar{u}}_i \tilde{\bar{u}}_j, \tag{4.9}$$

is the sub-test-filter-scale momentum tensor, which needs to be modelled due to the unknown term $\widetilde{\overline{u_i u_j}}$. Similar to $\boldsymbol{\tau}^r$ in (4.1), a closure model for $\boldsymbol{T}^r$ using the Smagorinsky approach could be defined as follows

$$T^r_{ij} = -2c_s \widetilde{\Delta}^2 \widetilde{\overline{S}} \tilde{\bar{s}}_{ij}, \tag{4.10}$$

where the Smagorinsky coefficient c_s, which is now allowed to depend on position and time, should be the same as that in (4.2) because of self-similarity and the scale-independent assumption (see e.g. Porté-Agel et al., 2000, for the scale-dependent dynamic SGS model). Applying the test filter $\tilde{\Delta}$ to the SGS momentum tensor τ_{ij} and its Smagorinsky model

in (4.1), and then subtracting them from the test SGS momentum tensor T_{ij} and its Smagorinsky model (4.10), respectively, yield (e.g. Pope, 2000; Meneveau &, Katz 2000)

$$L_{ij} = T_{ij} - \tilde{\tau}_{ij} = \widetilde{\bar{u}_i \bar{u}_j} - \tilde{\bar{u}}_i \tilde{\bar{u}}_j, \tag{4.11}$$

$$M_{ij} = \Delta^2 \widetilde{\bar{S}\bar{s}_{ij}} - \widetilde{\Delta}^2 \widetilde{\bar{S}} \tilde{\bar{s}}_{ij}, \tag{4.12}$$

which are the resolved stress tensor and the Germano rate of strain tensor, respectively, and are related by the following equation

$$L^r_{ij} = 2 c_s M_{ij}. \tag{4.13}$$

Since L^r_{ij} and M_{ij} are known from (4.11,4.12), the only unknown in (4.13) is c_s and as a result, the system of equation is extremely overdetermined. Lilly (1992) suggests a least square approach to get c_s, which gives

$$c_s = \frac{1}{2} \frac{L^r_{ij} M_{ij}}{M_{ij} M_{ij}}. \tag{4.14}$$

It is valuable to note the physical interpretation of (4.14), which is that c_s is characterized by amount of dissipation that is generated by projection of the resolved stress L^r_{ij} on the Germano rate of strain M_{ij} (e.g. Jiménez & Moser, 2000; Meneveau, 2012).

When L^r_{ij} and M_{ij} are not coaxial, c_s is negative, which might be interpreted as backscatter (e.g. Germano et al., 1991). In this situation, any attempts to model the stress tensor as proportional to the rate of the strain tensor will fail (e.g. Jiménez & Moser, 2000). Indeed, negative eddy viscosity and diffusivity coefficients in (4.5) and (4.7), respectively, inevitably lead to numerical instabilities (e.g. Domaradzki et al., 1993; Ghosal et al., 1995; Pope, 2000; Meneveau &, Katz 2000; Remmler & Hickel, 2012). There are two common approaches for avoiding negative c_s: clipping c_s by setting negative values to a non-negative threshold (e.g. 0) and averaging c_s over homogeneous directions (e.g. Lilly, 1992; Ghosal et al., 1995; Lesieur & Métais, 1996; Piomelli, 1999; Meneveau &, Katz 2000; Porté-Agel et al., 2000; Pope, 2000; Lu & Porté-Agel, 2014). In this study, we apply the first approach: negative c_s values are set to zero, but otherwise c_s^+ is fully time and space dependent, i.e.

$$c_s^+(\boldsymbol{x}, t) = \begin{cases} c_s(\boldsymbol{x}, t) & : c_s(\boldsymbol{x}, t) \geq 0 \\ 0 & : c_s(\boldsymbol{x}, t) < 0 \end{cases}. \tag{4.15}$$

For comparison, we will also investigate the performance of the volume averaged c_s in our simulations.

In this work, we consider strongly stratified turbulence, i.e. with $Fr_\ell \ll 1$, in which the large-scale dynamics are dominated by quasi-horizontal vortical motions rather than gravity waves (Riley & de Bruyn Kops, 2003; Waite & Bartello, 2004; Lindborg, 2006). Such flows are known to have a layered structure with layer thickness around L_b (Waite & Bartello, 2004) and a direct cascade of energy to small scales (Lindborg, 2006). Simulations with isotropic resolution of L_b show that the layers break up into KH instabilities on the buoyancy scale (Laval et al., 2003; Waite, 2011); as a result, the horizontal wavenumber kinetic energy spectrum has an approximately $-5/3$ power law (Lindborg, 2006) with possibly a bump at L_b (Waite, 2011). In order to capture the downscale cascade in DNS, the buoyancy Reynolds number $Re_b = Fr_h^2 Re$ must be $\gg 1$, where $Fr_h = u_{rms}/Nl_h$ is the horizontal Froude number and Re is the Reynolds number (Brethouwer et al., 2007; Almalkie & de Bruyn Kops, 2012; Bartello & Tobias, 2013). Here, l_h is the horizontal scale that is obtained from the Taylor hypothesis. For classical LES models (Smagorinsky, 1963; Kraichnan, 1976), it seems only necessary that L_b be sufficiently resolved (Khani & Waite, 2014a).

4.3 Methodology

Forced stratified turbulence is studied in this paper, where the forcing term is applied to the rotational part of the horizontal velocity field (i.e. vortically forced stratified turbulence, see Herring & Métais, 1989; Waite & Bartello, 2004; Waite, 2011; Khani & Waite, 2014a, for more details). Idealized simulations in a cubic box of side $L = 2\pi$ are considered. The sharp spectral filter is employed, where the relationship between the cutoff wavenumber k_c and the grid spacing Δ is given by

$$\Delta = \frac{\pi}{k_c}. \tag{4.16}$$

Spatial derivatives are discretized using the spectral transform method, where the two-thirds rule (e.g. Durran, 2010) is applied in each direction for the elimination of aliasing errors. Hence, the cutoff wavenumber k_c is related to the resolution as

$$k_c = \pi \frac{2n}{3L}, \tag{4.17}$$

where n is the number of grid points in x, y, and z directions. We can use (4.17) in (4.16) to get the effective grid spacing $\Delta = 3L/2n$, which is used in the eddy viscosity equations. For time advancement, the explicit third-order Adams-Bashforth scheme is employed.

Simulations are initialized with low-level random noise and spun up at low resolution ($n = 256$) and with hyperviscosity to $t = 300$. Simulations are then continued at low

($n = 256$) and high ($n = 512$) resolution with the dynamic Smagorinsky subgrid scale model (a similar approach is considered in e.g. Waite & Bartello, 2004; Waite, 2011; Khani & Waite, 2014a). Additional simulations with the regular Smagorinsky model (described in Khani & Waite, 2014a) are also considered for comparison. Four different buoyancy frequencies of $N = 2$, 4, 6 and 12, along with an unstratified case ($N = 0$), are considered. Froude numbers vary from 0.001 to ∞ to cover both strongly stratified (as in e.g. Riley & de Bruyn Kops, 2003; Waite & Bartello, 2004; Lindborg, 2006; Hebert & de Bruyn Kops, 2006b; Brethouwer et al., 2007; Waite, 2011; Khani & Waite, 2013, 2014a) and unstratified turbulence. The typical kinetic energy dissipation rate ϵ is around 10^{-4}, which gives a forcing time scale $t_f \sim 10$, when combined with the forcing wavenumber $k_f = 3$. The turbulent Prandtl number $Pr_t = 1$ and $u_{rms} = \sqrt{\langle E(t) \rangle}$ (e.g. Khani & Waite, 2014a), where the angle bracket $\langle \cdot \rangle$ denotes time averaging over $375 \leq t \leq 450$. Table 4.1 shows parameters and averaged quantities for the dynamic Smagorinsky LES in this paper, where k_o is based on $\langle \epsilon \rangle$ and k_b is based on u_{rms}.

4.4 Results and Discussion

4.4.1 Buoyancy scale effects on the dynamic Smagorinsky model.

The compensated horizontal wavenumber energy spectra, in which the horizontal spectra are normalized by $k_h^{-5/3} \langle \epsilon \rangle^{2/3}$, are shown in figure 4.1. The advantage of using the compensated spectra is that constant horizontal spectra at intermediate wavenumbers suggest an inertial subrange with the spectral slope of $-5/3$. The high resolution case with $N = 2$ shows an almost constant normalized spectrum over $6 \lesssim k_h \lesssim 30$ along with a wide bump around $k_b \sim 30$. The lower resolution simulation with the same stratification exhibits a steeper spectrum, in which the bump around the buoyancy scale is weakly resolved. Increased stratification steepens the compensated horizontal wavenumber energy spectra, to the extent that the high resolution cases with $N = 4$ and 6 do not clearly show constant inertial subranges but resolve (small) bumps around $k_b \sim 60$ and 80, respectively. In addition, the low-resolution LES with larger stratification do not seem to capture any inertial subrange or bumps. In agreement with LES of stratified turbulence in Khani & Waite (2014a), these results suggest that resolving a clear constant inertial subrange in the compensated horizontal wavenumber spectrum depends on the resolution and buoyancy frequency. As a result, stronger stratification may need higher resolution in LES to capture an inertial subrange.

Table 4.1: List of numerical simulations.

Dynamic Smagorinsky	N	n	k_b	k_c	k_o	$\langle\epsilon\rangle$	$\langle E(t)\rangle$	Fr_h	k_c/k_b	Δ/L_b	Δt
d5N0	0	512		168		1.5×10^{-4}	0.0058	∞			0.006
d5N2	2	512	31	168	271	1.1×10^{-4}	0.0043	0.013	5.42	0.092	0.009
d5N4	4	512	57	168	756	1.1×10^{-4}	0.0049	0.006	2.95	0.169	0.008
d5N6	6	512	80	168	1352	1.2×10^{-4}	0.0056	0.003	2.10	0.239	0.007
d2N0	0	256		83		1.4×10^{-4}	0.0053	∞			0.018
d2N2	2	256	30	83	273	1.1×10^{-4}	0.0044	0.012	2.77	0.180	0.018
d2N4	4	256	54	83	777	1.1×10^{-4}	0.0055	0.005	1.53	0.327	0.016
d2N6	6	256	72	83	1327	1.2×10^{-4}	0.0070	0.003	1.15	0.435	0.015
d2N12	12	256	127	83	3679	1.3×10^{-4}	0.0090	0.001	0.65	0.763	0.010
Smagorinsky	N	n	k_b	k_c	k_o	$\langle\epsilon\rangle$	$\langle E(t)\rangle$	Fr_h	k_c/k_b	Δ/L_b	Δt
S7N2	2	768	32	254	286	9.8×10^{-5}	0.0039	0.012	7.94	0.063	0.006
S5N2	2	512	31	168	262	1.2×10^{-4}	0.0042	0.014	5.42	0.092	0.009
S2N2	2	256	32	83	282	1.0×10^{-4}	0.0040	0.013	2.59	0.193	0.018

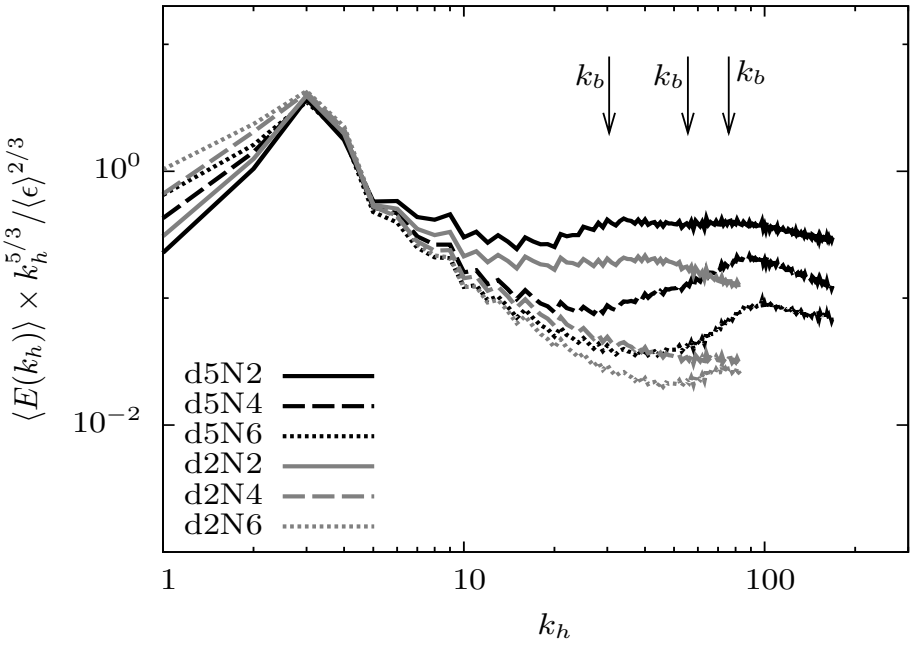

Figure 4.1: The averaged compensated horizontal energy spectra. The spectra are averaged over $375 \leq t \leq 450$. From left to right, arrows show buoyancy wavenumbers k_b that correspond to buoyancy frequencies $N = 2$, 4, and 6, respectively.

Khani & Waite (2014a) have shown that in the Kraichnan and Smagorinsky LES, capturing dynamics of stratified turbulence depends on the ratio Δ/L_b. Only for sufficiently small values of Δ/L_b - below 0.47 for Kraichnan and 0.17 for Smagorinsky - were the small-scale features of stratified turbulence, including KH instabilities and locally small values of the Richardson number, captured. To evaluate the relevance of this criterion for the dynamic Smagorinsky model, we consider the horizontal vorticity fields as well as distributions of the local Richardson number in our stratified simulations.

Figure 4.2 shows the y component of the vorticity $\bar{\omega}_y$ in the x-z plane for the high-resolution simulations with different buoyancy frequencies at $y = 0.25$ and $t = 450$. Unlike the unstratified case (figure 4.2a), the stratified cases are layered in the vertical direction. KH instabilities are clearly visible in figure 4.2(b), but less so in figures 4.2(c) and (d); indeed, the increased stratification in figure 4.2(c) and (d) leads to decreasing KH billows. For stratified simulations, increased stratification inhibits KH instabilities as the layer thickness decreases towards the eddy dissipation scale (as in e.g. Hebert & de Bruyn Kops, 2006a; Brethouwer et al., 2007; Khani & Waite, 2014a).

There is an apparent connection between cases with no inertial subrange in figure 4.1, and cases with no KH instabilities in figure 4.2. This connection has been noted previously in DNS (Waite, 2014) and other kinds of LES (Khani & Waite, 2014a). To further investigate this connection with the dynamic Smagorinsky model, we consider the local Richardson number. The Richardson number shows the ratio of total (ambient plus perturbation) buoyancy frequency over the square of the vertical shears of horizontal motions, written as

$$Ri = \frac{N^2 - \frac{g}{\rho_0}\frac{\partial \bar{\rho}}{\partial z}}{\left(\frac{\partial \bar{u}}{\partial z}\right)^2 + \left(\frac{\partial \bar{v}}{\partial z}\right)^2}, \tag{4.18}$$

where ρ_0 and g are the gravity and reference density, respectively. Small Richardson numbers including negative values correspond to overturning and KH instabilities. Figure 4.3 shows the time-averaged histograms of the local Richardson number Ri for the high- and low-resolution LES with different buoyancy frequencies. Histograms show long tails for positive Ri and also rapid drops for negative Ri. It appears that by increasing the resolution and decreasing the buoyancy frequency, the peaks in the Ri histograms move towards negative values, i.e. more of the domain is subject to KH and gravitational instabilities. In addition, the high resolution case with $N = 2$ (the black solid line) shows the largest number of points with negative values and the smallest number of points with positive Ri. However, the low-resolution case with $N = 6$ (the grey dot line) shows the largest histograms for positive Ri and maybe just a few points with negative Ri. Consistent with the Smagorinsky and Kraichnan LES of Khani & Waite (2014a), increased resolution at fixed buoyancy

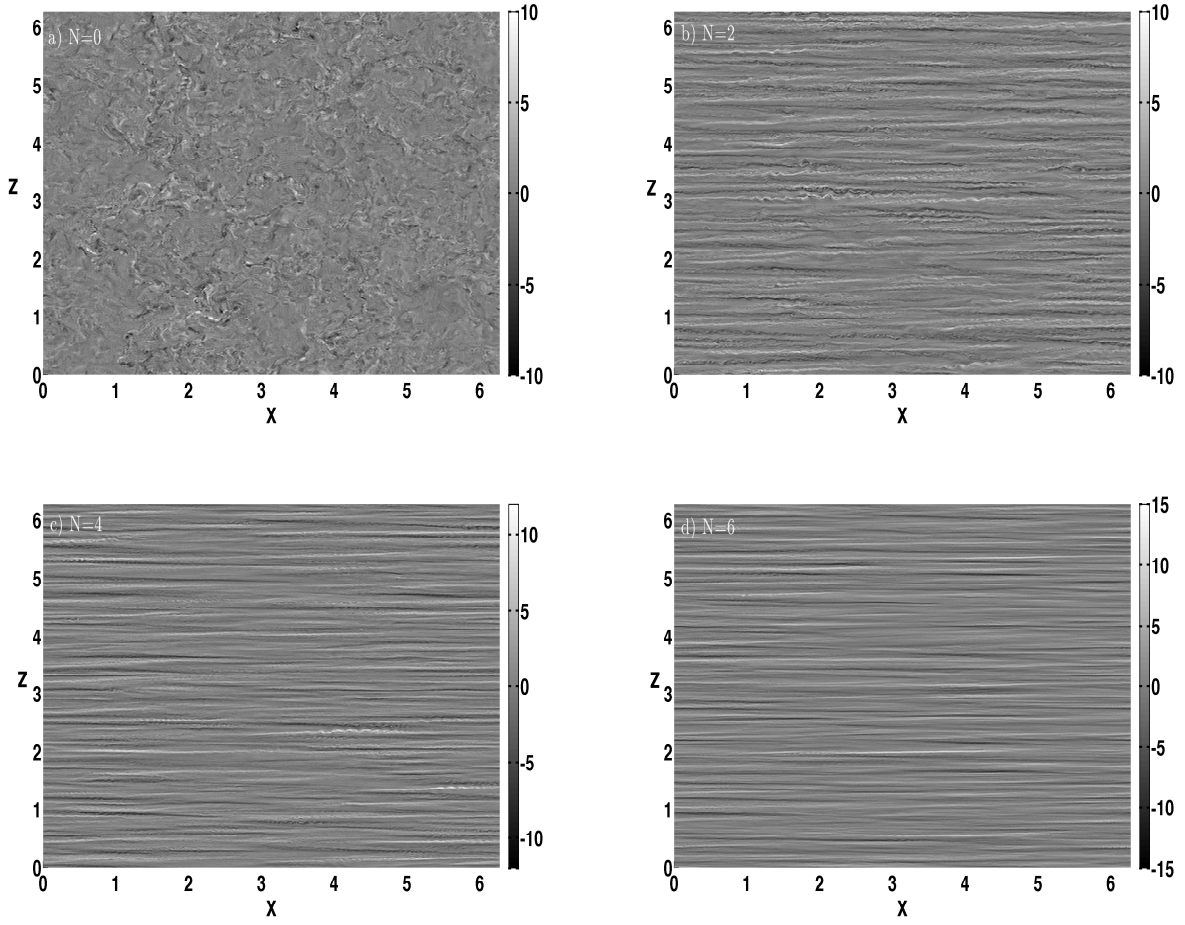

Figure 4.2: Vorticity field in y-direction, $\bar{\omega}_y$, on the x-z plane at $y = 0.25$ and $t = 450$ for the high resolution case with (a) $N = 0$, (b) $N = 2$, (c) $N = 4$, and (d) $N = 6$.

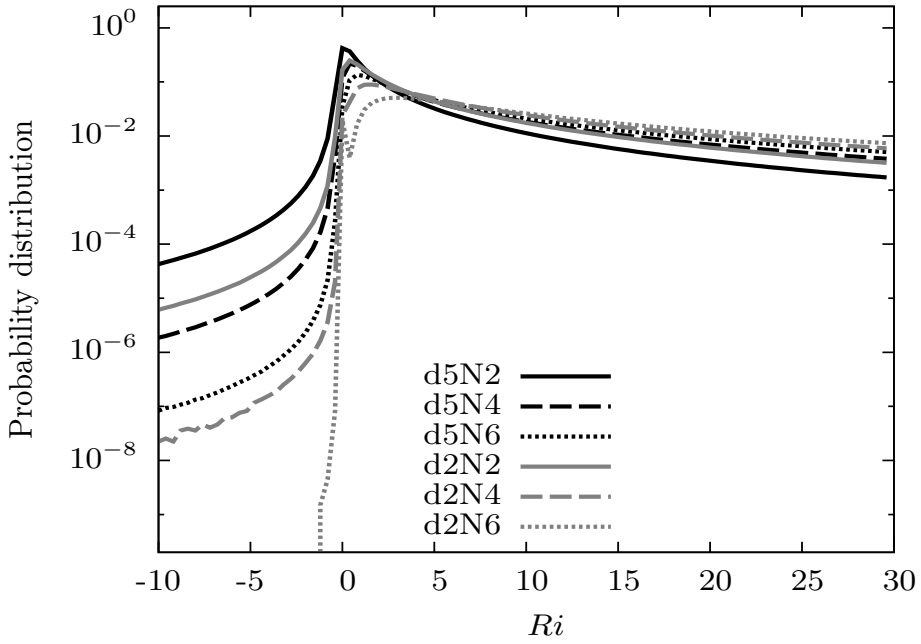

Figure 4.3: The averaged histograms of local Richardson number Ri. Only the segment $-10 \leq Ri \leq 30$ is shown. Histograms are normalized by bin size to give probability distributions, and are computed with 100 bins over the given segment ($\Delta Ri = 0.4$).

frequency or decreased stratification at fixed resolution, increases the number of points with small and negative Ri. As a result, figure 4.3 demonstrates that increased resolution or decreased stratification more likely leads to generation of KH instabilities and overturning (consistent with the results of figure 4.2).

Considering these findings, we can now attempt to find a threshold for Δ/L_b which guarantees that the breakdown of the layers into KH instabilities is captured (see Khani & Waite, 2014a, for similar thresholds in the Kraichnan and Smagorinsky LES). According to table 4.1 and figure 4.3, if we consider cases with $\Delta < 0.24L_b$ (i.e. $k_c > 2.1k_b$), the averaged Ri histograms for $-10 \leq Ri \leq 30$ are above 10^{-6}. On the other hand, if $\Delta > 0.24L_b$, only very few points with small and negative Ri appear. These findings suggest that the maximum grid spacing for the dynamic Smagorinsky model should be between $0.18L_b < \Delta < 0.24L_b$. By contrast, threshold for the regular Smagorinsky LES is in the range $0.12L_b \leq \Delta < 0.17L_b$ (see Khani & Waite, 2014a). While the dynamic

Smagorinsky values are larger – i.e. lower resolution is able to capture the basic dynamics of stratified turbulence – these ranges nearly overlap, suggesting that the criteria for the regular and dynamic Smagorinsky are close. In the next section, we compare these two SGS models and show that the dynamic Smagorinsky model is clearly better.

4.4.2 The dynamic Smagorinsky model versus the Smagorinsky model

To get a better understanding of how well the dynamic Smagorinsky model performs in stratified turbulence simulations, we compare to results obtained with the regular Smagorinsky model for the same stratifications and resolutions (results from Khani & Waite, 2014a, these simulations are labeled with 'S' in table 4.1). Figure 4.4 shows the horizontal wavenumber energy spectra at different resolution and fixed buoyancy frequency for both SGS models. Clearly, the dynamic version is less dissipative than the regular Smagorinsky model with the same resolution at large horizontal wavenumbers: at the same resolutions, the dynamic and regular Smagorinsky results agree fairly well at large scales but diverge at small scales, where the regular Smagorinsky exhibit a much broader and steeper dissipation range. This is particularly pronounced at the lower resolution ($n = 256$), where the regular Smagorinsky spectrum is much steeper than the dynamic model over most wavenumbers. It is interesting that the dynamic case with $n = 512$ is very similar to the Smagorinsky LES with $n = 768$; nevertheless, the Smagorinsky model is still more dissipative for $k_h \gtrsim 60$. In addition, the low resolution dynamic Smagorinsky case with $N = 2$ is very close to the regular Smagorinsky LES with $n = 512$ and $N = 2$. This trend implies that the dynamic Smagorinsky LES looks like the regular Smagorinsky case with twice the resolution. As a result, the low resolution dynamic Smagorinsky model yields similar results to the high resolution Smagorinsky model at fixed buoyancy frequency. It is worthwhile to mention that at the same resolution, the dynamic and regular Smagorinsky models are almost identical at large scales: for the case with $n = 256$, they are very similar for $k_h < 6$, and for the case with $n = 512$, they are almost identical up to $k_h = 20$.

Figure 4.5 shows the horizontal and vertical wavenumber spectra of SGS energy transfer (i.e. eddy dissipation spectra) for the stratified and unstratified dynamics model at $t = 450$. For comparison, the eddy dissipation spectra of the Smagorinsky LES for the case with $n = 768$ and $N = 2$ (see Khani & Waite, 2014a) are also shown. For unstratified cases, the maximum eddy dissipation occurs at small scales for both the horizontal and vertical wavenumber spectra. These trends are consistent with the isotropic dissipation picture, in

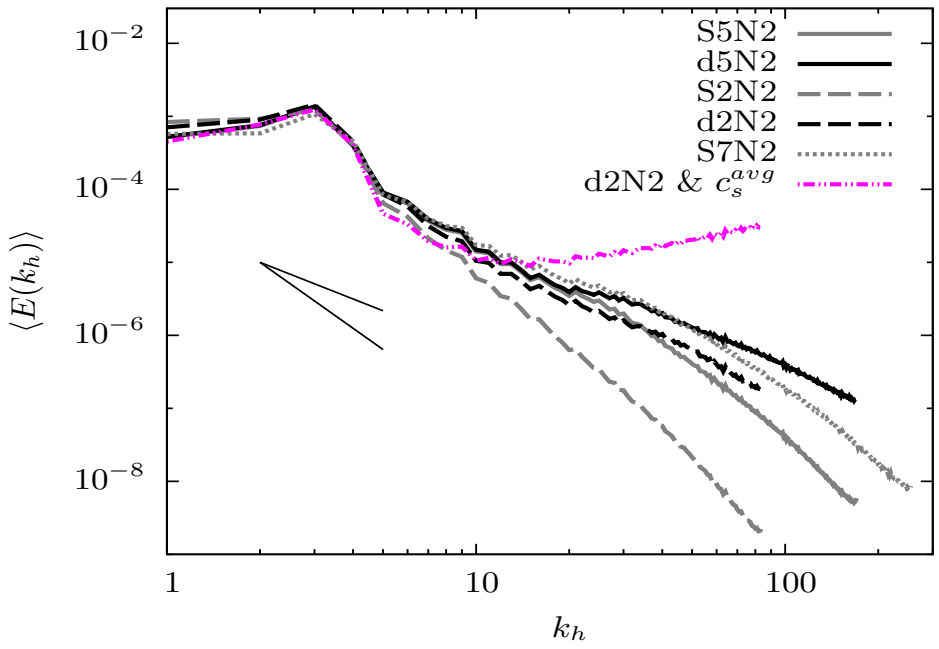

Figure 4.4: The averaged horizontal wavenumber energy spectra for the dynamic Smagorinsky cases that are compared with the Smagorinsky cases at different resolutions with fixed buoyancy frequency $N = 2$. The dash double-dot magenta curve shows the averaged horizontal wavenumber energy spectra over $300 \leq t \leq 356$ for dynamic Smagorinsky simulation, in which c_s values are space averaged instead of clipping negative values. The black solid line segments show $-5/3$ and -3 slopes.

which the kinetic energy is damped mainly at small scales. For stratified cases, however, the eddy dissipation spectra are very different in the horizontal and vertical directions. According to figure 4.5(a), the horizontal wavenumber spectra of SGS energy transfer peaks at large scales.

Unlike the horizontal wavenumber spectra, the vertical wavenumber spectra of eddy dissipation for the stratified cases peaks at small scales (figure 4.5b). Increased stratification or decreased resolution increases the vertical SGS energy transfer spectra due to contracting the thickness of vertical layers towards the dissipation scale or increasing dissipation scales, respectively (as seen in previous hyperviscosity simulations and DNS, e.g. Waite & Bartello, 2004; Hebert & de Bruyn Kops, 2006a; Brethouwer et al., 2007). As a result, for an isotropic eddy viscosity model, increased stratification leads to anisotropic eddy dissipation spectra due to strongly anisotropic resolved scales (see also Khani & Waite, 2014a, for the Kriachnan and Smagorinsky models). It is worthwhile to mention that the horizontal and vertical eddy dissipation spectra of the dynamic Smagorinsky LES with $n = 512$ and $N = 2$ are very similar to their counterparts in the Smagorinsky LES with higher resolution $n = 768$ and the corresponding buoyancy frequency, especially when $k_{h,v} \lesssim 60$ (figures 4.5). As a result, the low resolution dynamic Smagorinsky model generates almost the same eddy dissipation as the high resolution Smagorinsky model in LES of stratified turbulence.

In conclusion, this section shows that the maximum criterion on Δ/L_b for resolving KH instabilities in the dynamic Smagorinsky model is definitely larger than that for the regular Smagorinsky model. Even with half the resolution, the dynamic Smagorinsky model gives similar results to the regular Smagorinsky model (figure 4.4).

4.4.3 The dynamic Smagorinsky coefficient c_s

In this section, a detailed analysis on the dynamic coefficient c_s is presented. Figure 4.6(a) shows a snapshot of the c_s^+ field in the x-z plane along with a few contours of the characteristic rate of strain $\bar{S} = (2\bar{s}_{ij}\bar{s}_{ij})^{1/2}$ at $y = 0.25$ and $t = 450$ for the high resolution case with $N = 4$. The vertical axis is zoomed in to show around 13 vertical layers of length $2\pi/k_b$. It is interesting that the presence of stratification leads to vertical layers in the c_s^+ field. Black contours of $\bar{S}$ indicate low values $\bar{S} = 1$ and 1.5. The magenta contours on the other hand show higher values $\bar{S} = 6$ and 8. Interestingly, regions with high straining in figure 4.6 are generally associated with zero or very small values of c_s^+, while regions with low straining correspond with larger values of c_s^+. This behaviour, which has been investigated elsewhere in unstratified turbulence (e.g. Kleissl et al., 2006; Wan &

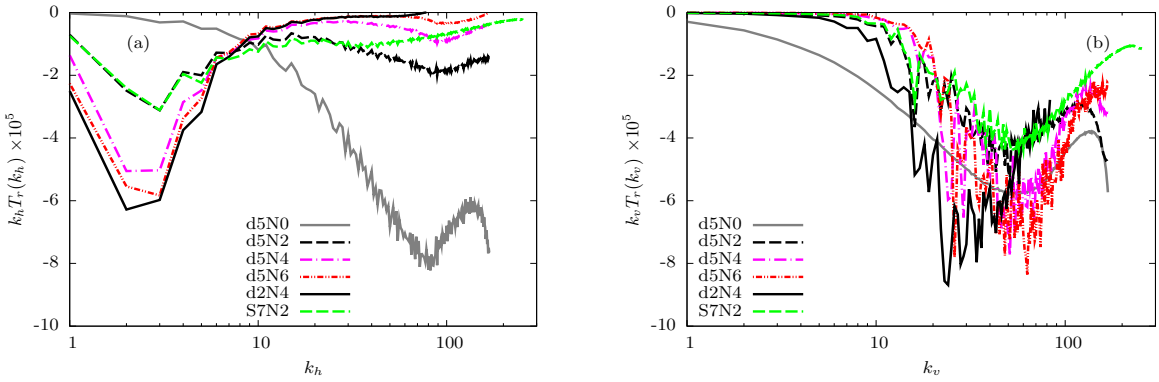

Figure 4.5: The horizontal (a) and vertical (b) wavenumber spectra of SGS energy transfer for the low resolution and high resolution cases at $t = 450$. The spectra are multiplied by wavenumber in order to preserve area on the log-linear axes. For comparison, the results of high resolution Smagorinsky LES are also shown (Khani & Waite, 2014a).

Porté-Agel, 2011), suggests that the dynamic Smagorinsky coefficient c_s decreases as shear increases in order to preserve the small-scale instabilities between vertical layers.

Figure 4.6(b) shows the probability distributions of c_s^+ on gridpoints restricted to different ranges of $\bar{S}$ at $t = 450$. It is clear that increased straining is associated with smaller values of c_s^+. With weak straining, distributions of the dynamic Smagorinsky coefficient c_s^+ show both small and large c_s^+ values. However, for large straining, these distributions show small c_s^+ values. For example, for $\bar{S} \geq 7$ – the solid black line in figure 4.6(b) – c_s^+ values are smaller than $(0.14)^2$. This trend is consistent with the suggestion of Deardorff (1971) that the presence of shear implies small c_s^+ values. In addition, looking at c_s^+ fields at different stratifications shows that increased stratification at fixed resolution leads to vertical layers that are not fully resolved, consistent with failure to the criterion on Δ/L_b (see figure 4.7).

The time-averaged histograms of c_s at different resolutions and buoyancy frequencies are shown in figure 4.8(a). Increased stratification leads to decreasing standard deviations, i.e. c_s values tend to get smaller (consistent with figure 4.6). Interestingly, the distribution of negative c_s (before clipping is applied) is very similar to that of positive c_s (similar trends are seen in Kang et al., 2003; Meneveau et al., 1996, for probability distributions of local SGS dissipation, and probability distributions of c_s, respectively). Since we remove negative c_s values at every timestep due to numerical stabilities, figure 4.8(a) indicates

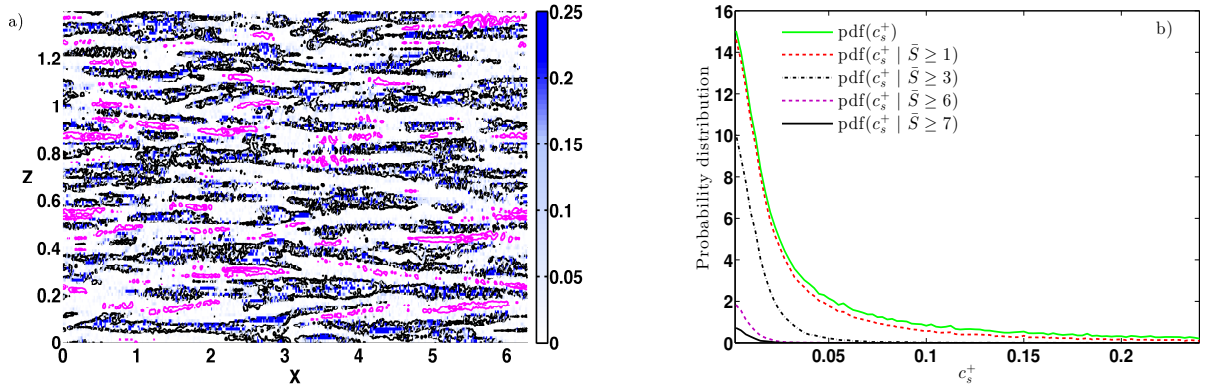

Figure 4.6: (a) The Smagorinsky coefficient field c_s^+ on the x-z plane and (b) the conditional distribution of c_s^+, for the high resolution case with $N = 4$ at $y = 0.25$ and $t = 450$. In the panel (a), contours of constant $\bar{S} = (2\bar{s}_{ij}\bar{s}_{ij})^{1/2}$ are overlayed on the c_s^+ field where the vertical axis is zoomed in to $80/k_b$ that includes around $13L_b$. The magenta contours present high values $\bar{S} = 6$ and 8 and the black contours show those of low values $\bar{S} = 1$ and 1.5.

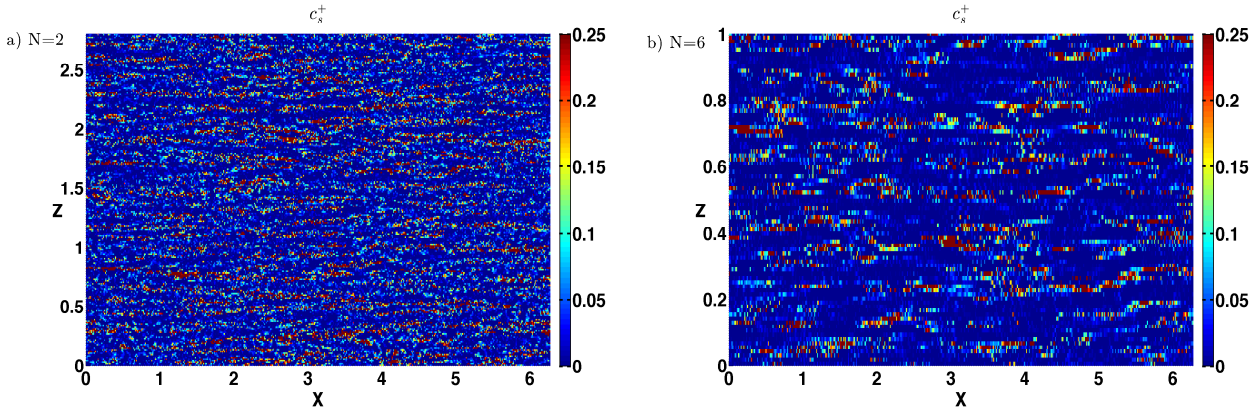

Figure 4.7: The Smagorinsky coefficient field c_s^+ on the x-z plane for the high resolution cases with (a) $N = 2$ and (b) $N = 6$ at $y = 0.25$ and $t = 450$, where the vertical axes are zoomed in to $80/k_b$ to include around $13L_b$.

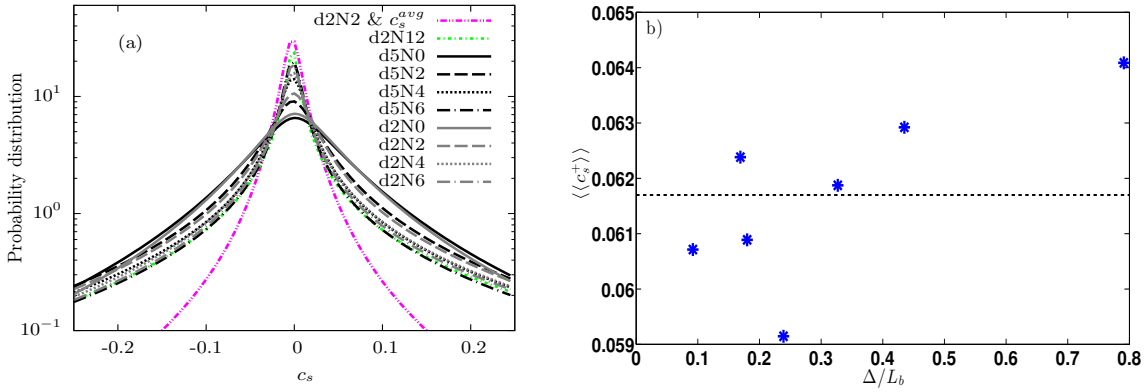

Figure 4.8: (a) The averaged histograms of Smagorinsky coefficient c_s and (b) the time-space averaged c_s versus Δ/L_b. In panel (a) only the segment $-0.25 \leq c_s \leq 0.25$ is shown. Histograms are normalized by bin size to give probability distributions, and are computed with 100 bins over the given segment ($\Delta c_s = 0.005$). The dashed line in panel (b) shows the average of all $\langle\langle c_s^+\rangle\rangle$ values.

that we lose some local information about the nature of energy transfer in the dynamic Smagorinsky model. In addition, this plot shows that the volume averaged c_s values are very close to zero. Figure 4.8(b) shows the time-and-space average (denoted by double angle bracket $\langle\langle\cdot\rangle\rangle$) of c_s^+ versus Δ/L_b. It is interesting that the time-space averaged c_s^+ for stratified cases are around $\langle\langle c_s^+\rangle\rangle = (0.25)^2$ (the dashed-black line in figure 4.8b) which is only slightly larger than that of the non-stratified case with $\langle\langle c_s^+\rangle\rangle = (0.23)^2$, and also larger than the regular Smagorinsky constant $c_s = (0.17)^2$. This behaviour might suggest that the presence of stratification decreases straining in turbulent flows and so the dynamic Smagorinsky model implies larger c_s in stratified turbulence to correspond with the changes in flow dynamics as stratification appears (see also figure 4.6).

An alternative to clipping negative c_s values is to use spatial averaging of c_s over the homogeneous directions, as is often done in boundary layer simulations (e.g. Pope, 2000; Meneveau &, Katz 2000; Porté-Agel et al., 2000). Here, since we are considering homogeneous stratified turbulence, this approach amounts to taking a spatial average of c_s before evaluating the eddy viscosity (4.2). We have evaluated this approach by performing an additional simulation with $n = 256$ and $N = 2$, in which c_s values are averaged over the entire domain instead of clipping negative c_s values. Because of the lack of sufficient dissipation at small scales, the simulation in this case blew up at around $t = 356$ (see the magenta curve in figure 4.4, which clearly shows an artificial pileup of energy at large

wavenumbers). The averaged probability distribution of c_s for this simulation over $300 \leq t \leq 356$ is also shown in figure 4.8(a), in which shorter tails and a larger peak are seen. For this case, the standard deviation is half of that in the case with clipped negative c_s values.

4.5 Conclusions

A systematic analysis on the performance of the dynamic Smagorinsky model in stratified turbulence has been studied in this paper. Our results show that if $\Delta/L_b < 0.24$, KH instabilities and overturning are more likely fully captured in LES of stratified turbulence using the dynamic Smagorinsky model. These criteria on Δ/L_b depend on the particular SGS model. For example, Khani & Waite (2014a) argued that for the Smagorinsky and Kraichnan model Δ/L_b should be less than 0.17 and 0.47, respectively, to ensure capturing KH instabilities in stratified turbulence. As a result, the resolution limit on Δ in the dynamic Smagorinsky model is 40% larger than that of the Smagorinsky model (see figure 4.4). In addition, this study show that spectra of SGS energy transfers in stratified simulations are significantly different in the horizontal and vertical directions, in line with other LES models (Khani & Waite, 2014a). The maximum eddy dissipation spectra in stratified cases occur at large horizontal and small vertical scales. This behaviour suggests that spectra of SGS energy transfer are anisotropic in stratified turbulence. Overall, the eddy dissipation from the dynamic Smagorinsky LES with $N = 2$ and $n = 512$ looks similar to the regular Smagorinsky LES at the same buoyancy frequency with $n = 768$.

The dynamic eddy viscosity coefficient c_s^+ shows a layerwise field in the presence of stratification, consistent with the familiar layered structure of stratified turbulence. This finding implies that the dynamic Smagorinsky model can make a connection between the SGS model and stratification and that this relation is an improvement on performance of traditional SGS models like the Smagorinsky model in stratified turbulence. It is interesting that large values of c_s^+ correspond to regions with weak straining. Consistently, regions with large shears (strong vertical straining), the values of c_s^+ are very small. This behaviour explains why the dynamic Smagorinsky model is overall less dissipative than the regular Smagorinsky model. Also, the overall relationship between c_s^+ and shear $\bar{S}$ is similar to what has been discussed in the literature on unstratified turbulence. In addition, local distributions of negative c_s are very close to positive c_s, implying that local negative dissipation (i.e. backscatter) might be important in the dynamic Smagorinsky model. Nevertheless, negative values of c_s are clipped in this study to stabilize the simulations and ensure sufficient small-scale dissipation.

At the same resolution, the dynamic Smagorinsky model is much more expensive than

the regular Smagorinsky model; wall clock run times are approximately twice longer. This increase in run time is due to the significant increase in the number of fast Fourier transforms (FFTs) required to compute c_s. On the other hand, the dynamic Smagorinsky model can be run at lower resolution and still give similar results to the regular Smagorinsky model. Decreasing the resolution by 33% (i.e. from $n = 768$ to $n = 512$) cuts the run time by a factor of 5. Halving the resolution (i.e. from $n = 512$ to $n = 256$) cuts the run time by a factor of 16, and still gives dynamic Smagorinsky results similar to regular Smagorinsky. Despite the increase in FFTs, the ability to run at lower resolution implies that dynamic Smagorinsky approach is clearly more efficient than the regular Smagorinsky.

We have now looked at three SGS models: Kraichnan, Smagorinsky and dynamic Smagorinsky. Despite the fact that these models were designed for unstratified turbulence, they work well for stratified turbulence when L_b is sufficiently well resolved. The interpretation of "sufficiently" depends on the model. The Kraichnan model is clearly the best – i.e. it requires the lowest resolution to give the same results – but it only works for triply periodic spectral models. Otherwise, the dynamic Smagorinsky model is better than the regular Smagorinsky. However, none of these models work well when L_b is not resolved. Eliminating this barrier, i.e. running LES without fully resolving L_b, would require a major rework. For future work, performing LES of stratified turbulence with anisotropic eddy viscosity terms could be considered. In addition, considering local backscatter in the dynamic SGS models is another potential avenue in studying stratified turbulence. Ultimately, we need to perform a high resolution DNS of stratified turbulence to study the dynamics of energy transfer around the buoyancy scale L_b and maybe the Ozmidov scale L_o.

4.6 Acknowledgments

Computations were performed on the gpc supercomputer at the SciNet HPC Consortium. SciNet is funded by: the Canada Foundation for Innovation under the auspices of Compute Canada; the Government of Ontario; Ontario Research Fund – Research Excellence; and the University of Toronto. Also, This work was made possible by the facilities of the Shared Hierarchical Academic Research Computing Network (SHARCNET: www.sharcnet.ca) and Compute/Calcul Canada. Financial support from the Natural Sciences and Engineering Research Council of Canada is gratefully acknowledged.

Chapter 5

Effects of the buoyancy Reynolds number on the dynamics of energy transfer in stratified turbulence

In this chapter, kinetic and potential energy transfer in DNS of decaying stratified turbulence are studied in both the physical and spectral domains. It is shown that the effective SGS energy transfer in physical space is a net downscale cascade, which is a combination of large upscale and downscale energy transfers. Our results suggest that backscatter in stratified turbulence depends on resolution, buoyancy frequency and the buoyancy Reynolds number Re_b. When $Re_b \lesssim O(1)$, the kinetic energy transfer spectra show negative values at intermediate scales, as reported elsewhere. We argue that this backscatter is due to viscous effects at the test filter scale. The effective turbulent Prandtl number spectra demonstrate that the assumption $Pr_t \approx 1$ is reasonable for local energy transfer.

5.1 Introduction

Large eddy simulations (LES) is an alternative numerical approach for decreasing the computational costs of direct numerical simulations (DNS). In LES, the large energy-containing eddies are directly resolved but subgrid scale (SGS) eddies are parametrized. Most SGS models such as the Smagorinsky (1963) and Kraichnan (1976) models are designed based on the Richardson (1922) energy-cascade hypothesis, which argued that the turbulent kinetic energy is generated at large scales and dissipated at small scales. Richardson's prediction could be valid for the average kinetic energy cascade, but might not be accurate in the local sense. Locally, the energy cascade is the net outcome of the forward scatter, i.e. the energy transfer from large to small scales, and the backscatter, which is the reverse energy transfer from the small to large scales. For example, Piomelli et al. (1991) and Domaradzki et al. (1993) have shown that the forward- and backscatter are of the same order of magnitude in turbulent channel flow and isotropic decaying turbulence, respectively.

In principal, the dynamic SGS scheme, proposed by Germano et al. (1991), has been designed to improve the performance of purely dissipative SGS schemes such as the Smagorinsky (1963) model by considering backscatter through the negative dynamic Smagorinsky coefficient c_s, which is a time- and space-dependent function. However, averaging c_s over a homogeneous direction is often required to avoid numerical instabilities (e.g. Ghosal et al., 1995; Pope, 2000; Meneveau &, Katz 2000). In this sense, some information about the dynamics of the local energy transfer is lost, and in practice, the averaging procedure removes the local effect of backscatter, because the averaged c_s is usually positive (e.g. Ghosal et al., 1995; Pope, 2000; Wan & Porté-Agel, 2011; Remmler & Hickel, 2012; Khani & Waite, 2014b).

Stratified turbulence occurs at the atmospheric mesoscale and oceanic sub-mesoscale, or on scales for which fluid motions are strongly affected by stratification but weakly affected by the Earth's rotation (e.g. Riley & Lelong, 2000). The presence of stratification leads to the generation of anisotropic features such as pancake vortices. These in turn leads to the development of different length scales and spectral slopes in the horizontal and vertical directions and so forth (see e.g. Billant & Chomaz, 2001; Waite & Bartello, 2004; Lindborg, 2006; Brethouwer et al., 2007). Recently, the dynamics of energy transfer in stratified turbulence has been studied in wavenumber space (Khani & Waite, 2013; Remmler & Hickel, 2014). Using DNS of decaying stratified turbulence, Khani & Waite (2013) studied the dynamics of horizontal and vertical energy transfer around the Ozmidov scale. It was shown that the presence of stratification leads to a non-local horizontal energy transfer (Khani & Waite, 2013). In addition, the spectral eddy viscosity based on the vertical kinetic energy shows negative values when the flow is subjected to very stable

stratification, and negative turbulent Prandtl numbers have also been reported (Remmler & Hickel, 2014).

In physical space, backscatter can be calculated by filtering velocity fields in DNS, and directly measuring the sub-filter scale (henceforth referred to as SGS) momentum tensor τ_{ij}. Following Piomelli et al. (1991), backscatter may be defined by negative values of the effective SGS dissipation rates ϵ_{SGS} and ε_{SGS}, written as

$$\epsilon_{SGS} = -2\tau_{ij}\bar{S}_{ij}, \tag{5.1}$$

$$\varepsilon_{SGS} = -h_j\frac{\partial\bar{\rho}}{\partial x_j}, \tag{5.2}$$

where $\bar{S}_{ij}$ is the filtered rate of strain. A similar procedure was used recently to analyze SGS backscatter in DNS of reacting turbulence (O'Brien et al., 2014). Importantly, it is shown that backscatter depends on the dynamics of reacting flows and hence is not just a random and intermittent process (O'Brien et al., 2014). The dynamics of backscatter has not been studied for stratified turbulence. Indeed, the physical mechanisms underlying the dynamics of energy transfer are not completely understood in this context.

In this paper, the dynamics of forward and inverse energy transfer around the Ozmidov scale in DNS of stratified turbulence is studied at different buoyancy Reynolds numbers and using different test filters. In addition, the spectral kinetic and potential energy transfer, and the effective turbulent Prandtl number subjected to different test cutoffs and buoyancy Reynolds numbers are analyzed. The governing equations of motion and formulations for analyzing DNS diagnoses are presented in §5.2. Section 5.3 presents the methodology used, and §5.4 presents the results and discussion. Conclusions are given in §5.5.

5.2 Governing equations

For the DNS approach, the non-dimensional Navier-Stokes equations subjected to the Boussinesq approximation are

$$\frac{\partial\boldsymbol{u}}{\partial t} + \boldsymbol{u}\cdot\nabla\boldsymbol{u} = -\nabla p - \frac{1}{{Fr_\ell}^2}\rho\boldsymbol{e}_z + \frac{1}{Re_\ell}\nabla^2\boldsymbol{u}, \tag{5.3}$$

$$\nabla\cdot\boldsymbol{u} = 0, \tag{5.4}$$

$$\frac{\partial\rho}{\partial t} + \boldsymbol{u}\cdot\nabla\rho - w = \frac{1}{Re_\ell Pr}\nabla^2\rho, \tag{5.5}$$

where $\boldsymbol{u} = (u, v, w)$ is the velocity vector, ρ and p are the density and pressure perturbations, respectively; Re_ℓ, Fr_ℓ, and Pr are the initial Reynolds and Froude numbers, and

the Prandtl number, respectively. We can define the test-filtered variables by applying a filtering operator to the DNS results, written as

$$\bar{\boldsymbol{u}}(\boldsymbol{x},t)=\int_D G(\hat{\boldsymbol{x}},\boldsymbol{x})\boldsymbol{u}(\hat{\boldsymbol{x}},t)\mathrm{d}\hat{\boldsymbol{x}}, \tag{5.6}$$

where G is the filtering function and D is the spatial domain. Hence, the governing equations (5.3-5.5) can be rewritten for the test-filtered variables as follows

$$\frac{\partial\bar{u}_i}{\partial t}+\frac{\partial}{\partial x_j}(\bar{u}_i\bar{u}_j)=-\frac{\partial p}{\partial x_j}-\frac{1}{{Fr_\ell}^2}\bar{\rho}\boldsymbol{e}_z+\frac{1}{Re_\ell}\frac{\partial^2\bar{u}_i}{\partial x_j\partial x_j}-\frac{\partial\tau_{ij}}{\partial x_j}, \tag{5.7}$$

$$\frac{\partial\bar{u}_i}{\partial x_i}=0, \tag{5.8}$$

$$\frac{\partial\bar{\rho}}{\partial t}+\frac{\partial}{\partial x_j}(\bar{\rho}\bar{u}_j)-\bar{w}=\frac{1}{Re_\ell Pr}\frac{\partial\bar{\rho}}{\partial x_j\partial x_j}-\frac{\partial h_j}{\partial x_j}, \tag{5.9}$$

where

$$\tau_{ij}=\overline{u_iu_j}-\bar{u}_i\bar{u}_j, \tag{5.10}$$

$$h_j=\overline{\rho u_j}-\bar{\rho}\bar{u}_j, \tag{5.11}$$

are the SGS momentum and density fluxes that are known since DNS resolves both the test-filtered and sub-test-filter scales. Using the measured SGS momentum flux τ_{ij}, we can calculate the SGS dissipation ϵ_{SGS} through equation (5.1), which gives the rate of energy transfer between the test-filtered scales and the sub-test-filter motions. Following Piomelli et al. (1991), if ϵ_{SGS} is positive, then the kinetic energy transfers from the test-resolved to the SGS motions (forward scatter), i.e.

$$\epsilon^+=\frac{1}{2}(\epsilon_{SGS}+|\epsilon_{SGS}|). \tag{5.12}$$

However, if ϵ_{SGS} is negative, kinetic energy is transferred in the opposite direction (backscatter), i.e.

$$\epsilon^-=\frac{1}{2}(\epsilon_{SGS}-|\epsilon_{SGS}|). \tag{5.13}$$

Similar definitions could be applied for the forward- and backscatter of the potential energy transfer as follows

$$\varepsilon^+=\frac{1}{2}(\varepsilon_{SGS}+|\varepsilon_{SGS}|), \tag{5.14}$$

$$\varepsilon^-=\frac{1}{2}(\varepsilon_{SGS}-|\varepsilon_{SGS}|). \tag{5.15}$$

In the wavenumber domain, assuming periodic boundary conditions and a test filter cutoff wavenumber k_c, we can use the measured SGS fluxes in (5.10,5.11) to calculate the kinetic and potential effective SGS energy transfer spectra as follows (using the notation of Pope, 2000)

$$T_k(k|k_c,t) = \frac{1}{2}\langle F_j \hat{\bar{u}}_j^* + F_j^* \hat{\bar{u}}_j \rangle_k, \tag{5.16}$$

$$T_p(k|k_c,t) = \frac{1}{2}\langle J \hat{\bar{\rho}}^* + J^* \hat{\bar{\rho}} \rangle_k, \tag{5.17}$$

where F_j and J are the Fourier coefficients of the SGS fluxes $\partial\tau_{ij}/\partial x_j$ and $\partial h_j/\partial x_j$, respectively. The complex conjugate is shown by $*$ symbol, and the angle bracket $\langle\cdots\rangle_k$ denotes binning of the Fourier modes over spheres of constant radius k. Here, $k = |\boldsymbol{k}|$ and $\boldsymbol{k} = (k_x, k_y, k_z)$ is the three dimensional wavevector. In addition, the effective eddy viscosity $\nu_e(k|k_c,t)$ and the effective eddy diffusivity $D_e(k|k_c,t)$ are defined (as in Chapter 2) as

$$\nu_e(k|k_c,t) = \frac{T_k(k|k_c,t)}{2k^2 E(k,t)}, \tag{5.18}$$

$$D_e(k|k_c,t) = \frac{T_p(k|k_c,t)}{2k^2 E_p(k,t)}, \tag{5.19}$$

where $E(k,t)$ and $E_p(k,t)$ are the kinetic and potential energy spectra. Meanwhile, the effective turbulent Prandtl number can be written as

$$Pr_t(k|k_c,t) = \frac{\nu_e(k|k_c,t)}{D_e(k|k_c,t)}. \tag{5.20}$$

Stratified turbulence is characterized by large Reynolds number $Re = u_{rms} l_h/\nu$ and small horizontal Froude number $Fr_h = u_{rms}/N l_h$ such that the buoyancy Reynolds number

$$Re_b = ReFr_h^2, \tag{5.21}$$

is also large (e.g. Brethouwer et al., 2007). Here, u_{rms} and l_h are the root-mean-square velocity and horizontal length scale, respectively; N is the buoyancy frequency and ν is the molecular viscosity. The dissipation length scale is given by

$$k_d = \left(\frac{\epsilon}{\nu^3}\right)^{1/4}, \tag{5.22}$$

where ϵ is the kinetic dissipation rate. For decaying turbulence, the maximum k_d happens at the time for which ϵ is maximum.

5.3 Methodology

An idealized case study for decaying stratified turbulence is designed in a cubic domain with triply periodic boundary conditions, as employed in Chapter 2, and the side length $L = 2\pi$. Taylor-Green (TG) vortices, which include the horizontal structures with the vertical variations

$$\boldsymbol{u}(\boldsymbol{x}, 0) = \cos(z)[\cos(x)\sin(y), -\sin(x)\cos(y), 0], \tag{5.23}$$

are considered as the initial conditions, i.e. TG vortices with period π. Also, approximately 10% of the initial energy in the form of low-level noise perturbs the initial TG vortices isotropically. Noise is restricted to small wavenumbers $k < 10$. We have chosen to shrink the domain from that used in chapter 2 to allow for higher effective spatial resolution, which leads to a decrease in computation at time (as in e.g. Domaradzki et al., 1993).

The spectral transform method is employed for computing spatial derivatives, along with the two-thirds rule to eliminate aliasing errors from x, y and z directions. The number of grid points is given by n, and so the effective grid spacing is $\Delta = 1.5L/n$. The explicit third-order Adams-Bashforth scheme is used for time-stepping of all terms except the diffusion terms, for which the implicit trapezoidal method is employed. Simulations with four different initial Reynolds number $Re_\ell = 1351$, 3030, 6400 and 10900, and a range of the initial Froude number Fr_ℓ from 0.08 to ∞ are considered. Two different test cutoffs $k_c = 20$ and 40 are employed to study the spectral energy transfer between scales. The horizontal length scale l_h is calculated using the Taylor hypothesis, and $u_{rms} = \sqrt{E(t)}$ and $Pr_t = 1$. Table 5.1 shows the simulations parameters and identifiers.

Table 5.1: List of numerical simulations

Identifier	Re_ℓ	Fr_ℓ	n	Re_b	Fr_h	k_{max}/k_d	k_b	k_o	Δt_{avg}
R109F0.1	10900	0.16	768	$0.81 - 1.45$	0.009	$0.9 - 1.0$	$20.8 - 28.1$	$217.4 - 290.6$	$20 \leq t \leq 24$
R64F0.6	6400	0.64	384	$4.15 - 10.13$	$0.028 - 0.034$	$0.7 - 0.9$	$5.5 - 9.1$	$31.5 - 49.2$	$13 \leq t \leq 17$
R64F0.08	6400	0.08	512	$0.08 - 0.17$	0.004	$0.9 - 1.1$	$42.6 - 62.3$	$694.3 - 1012.4$	$29 \leq t \leq 33$
R30F0.5	3030	0.5	512	$1.30 - 2.47$	$0.023 - 0.035$	$1.7 - 2.0$	$7.8 - 12.5$	$50.7 - 69.8$	$15 \leq t \leq 19$
R30F0.2	3030	0.24	512	$0.33 - 1.00$	$0.015 - 0.021$	$1.5 - 2.0$	$15.9 - 24.2$	$113.0 - 197.5$	$18 \leq t \leq 22$
R30F0.1	3030	0.12	512	$0.12 - 0.19$	0.007	$1.6 - 1.8$	$29.5 - 37.6$	$367.0 - 468.5$	$25 \leq t \leq 29$
R30F0.08	3030	0.08	512	$0.04 - 0.07$	$0.003 - 0.004$	$1.7 - 2.0$	$45.1 - 55.8$	$735.3 - 1026.1$	$33 \leq t \leq 37$
R13F0.5	1351	0.5	256	$0.70 - 1.13$	$0.033 - 0.041$	$1.5 - 1.7$	$9.0 - 12.8$	$50.0 - 63.5$	$20 \leq t \leq 24$
R30	3030	∞	512			$1.2 - 2.1$			$7 \leq t \leq 11$

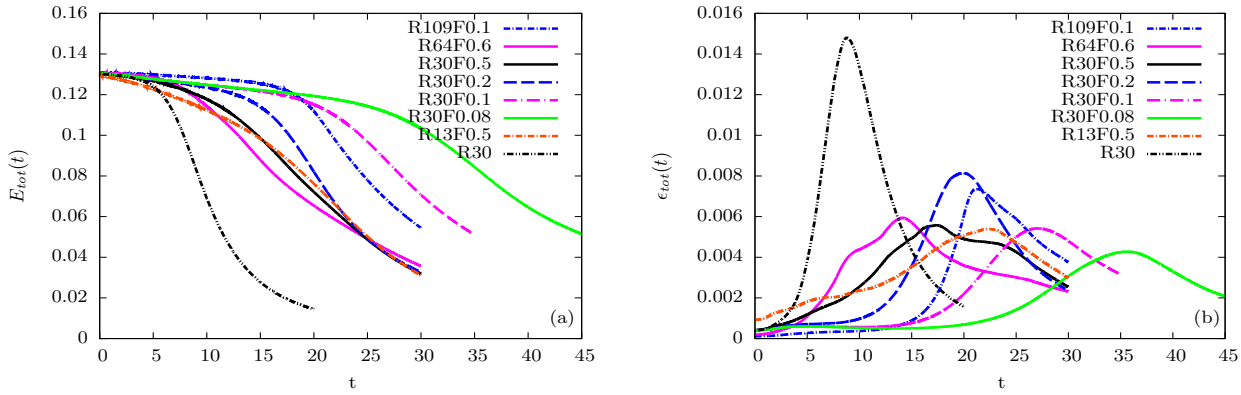

Figure 5.1: Time series of (a) total energy and (b) total dissipation rate.

5.4 Results & discussion

5.4.1 Overview of simulations

Figure 5.1 shows time series of the total energy and dissipation rates, in panels (a) and (b), respectively. For the unstratified case, a quick drop in the total energy level and a maximum in the total dissipation rate are visible at $t \approx 9$. Increased stratification or decreased resolution postpones the time of the energy drops and maximum dissipation. For example, the case with $Re_\ell = 3030$ and $Fr_\ell = 0.08$ has only a small decrease in energy up to $t \approx 27$, while the maximum dissipation rate occurs around $t = 36$. These trends suggest that by increasing stratification or decreasing the resolution, the occurrence of turbulence is postponed (in line with Riley & de Bruyn Kops, 2003; Khani & Waite, 2013).

Figure 5.2(a) shows the horizontal component of the vorticity ω_y on the x-z plane for the high resolution case with $Re_\ell = 10900$ and $Fr_\ell = 0.16$ at $t = 22$, which is around the time that maximum dissipation occurs. Layerwise structures along with Kelvin-Helmholtz (KH) instabilities are visible. In addition, small-scale features are present, which seem to correspond to the breakdown of KH billows into smaller-scale turbulence (figure 5.2a). The time-averaged probability distribution of the local Richardson number over $20 \leq t \leq 24$ for the high resolution simulation with $Fr_\ell = 0.16$ is shown in figure 5.2(b). The histogram is peaked around 0 and presents a long tail for $Ri > 0$ and a rapid drop off for negative Ri. The points with small and negative Richardson number suggest generation of KH instabilities and overturning, respectively, (in line with figure 5.2a).

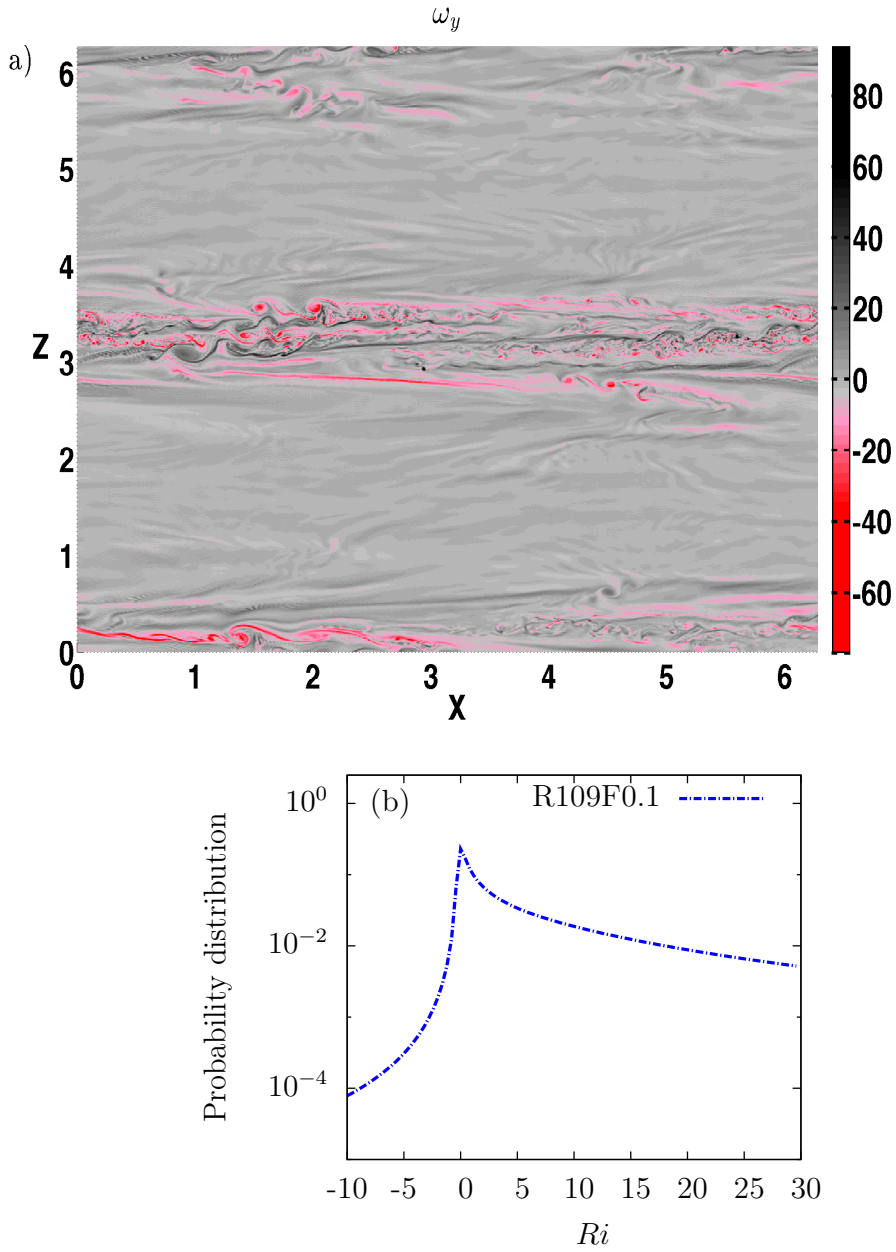

Figure 5.2: (a) The horizontal component of vorticity field ω_y in the x-z plane at $y = 0.25$ and $t = 22$, for the high resolution case with $Re_\ell = 10900$ and $Fr_\ell = 0.16$. (b) Averaged probability distribution of the local Richardson number Ri over $20 \leq t \leq 24$. Only the segment $-10 \leq Ri \leq 30$ is shown. Histograms are normalized by bin size to get the probability distribution: 100 bins over $-10 \leq Ri \leq 30$ ($\Delta Ri = 0.4$).

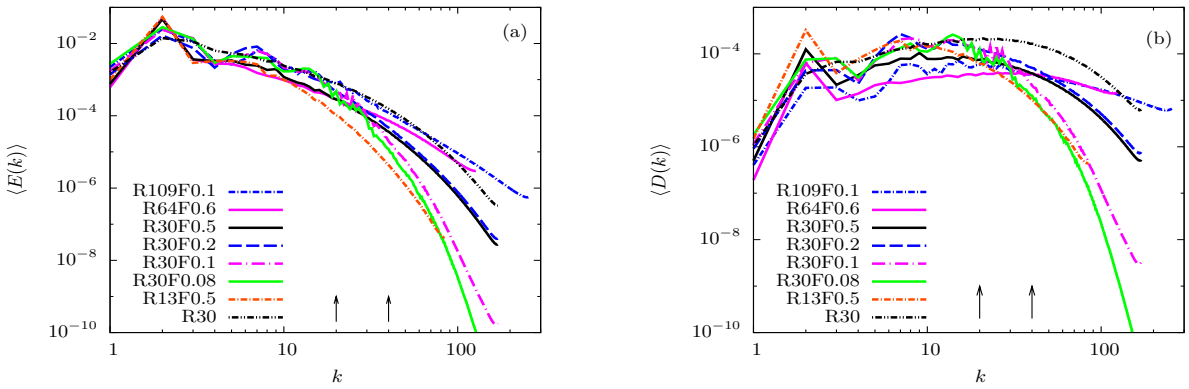

Figure 5.3: (a) Time-averaged kinetic energy spectra and (b) time-averaged dissipation spectra $D(k) = 2\nu k^2 E(k)$. Arrows indicate the location of the test cutoff $k_c = 20$ and 40.

The time-averaged kinetic energy and dissipation spectra are shown in figure 5.3. The time averaging is performed over periods that $\epsilon_{tot}(t)$ is peaked (as shown in table 5.1). Similar to previous studies (e.g. Riley & de Bruyn Kops, 2003; Khani & Waite, 2013), increased stratification or decreased resolution steepens the slope of the spectra (figure 5.3). As a result, decreasing the buoyancy Reynolds number Re_b leads to a delay in the onset of turbulence and steepens the spectral power law. Arrows in figure 5.3 indicate locations of the test cutoff $k_c = 20$ and 40, which are used in the next sections for measuring the energy transfer between scales.

5.4.2 Energy transfer in physical space

The forward- and backscatter components of the effective SGS kinetic and potential dissipation rates ϵ_{SGS} and ε_{SGS} for $k_c = 40$ are shown in figure 5.4. The maximum forward- or backscatter happens around the time when the total dissipation rate ϵ_{tot} is peaked. Increased stratification or decreased resolution decreases the amount of forward- and backscatter, and also postpones the peaks. As a result, decreased Re_b reduces forward- and backscatter, and weakens their peak values (figure 5.4). These results demonstrate that the presence of stratification decreases energy transfer between scales, i.e. both up- and downscale energy transfers are reduced by increasing stratification. Figure 5.5 shows the net kinetic and potential effective SGS energy transfers (i.e. ϵ_{SGS} and ε_{SGS}) subject to the test cutoff $k_c = 40$. Since all values in figure 5.5 are positive, this figure demonstrates that the effective SGS energy transfer is downscale, and ϵ_{SGS} and ε_{SGS} are peaked

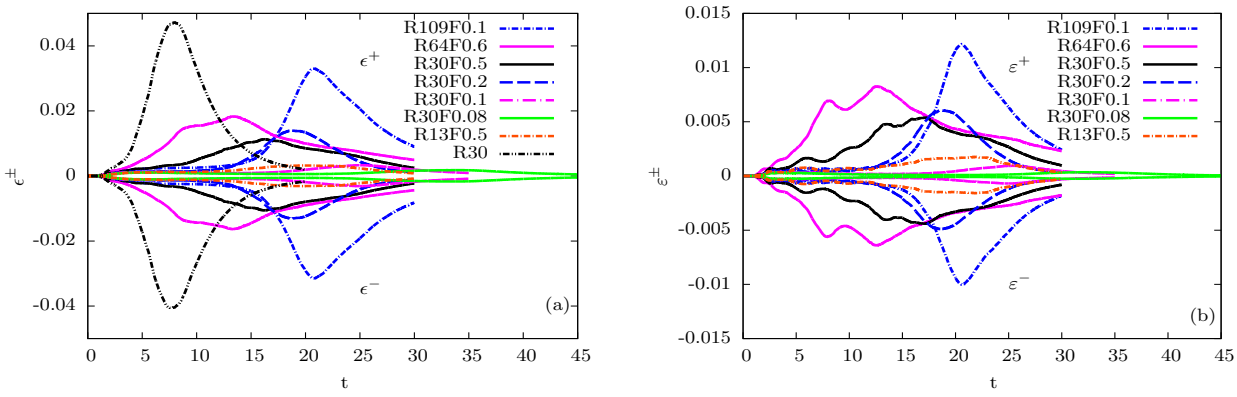

Figure 5.4: Time series of forward- and backscatter components of the effective SGS dissipation rate for $k_c = 40$: (a) kinetic and (b) potential.

around the time that the total dissipation rate ϵ_{tot} is peaked. It is interesting that the effective SGS energy transfer results from the superposition of two processes: forward- and backscatter, for which the net values of SGS transfer are much smaller than those for $\epsilon^{\pm}$ by almost one order of magnitude (figures 5.4 and 5.5). Similar findings have been reported for unstratified turbulence (e.g. Piomelli et al., 1991). In addition, our results show that the domain fraction for backscatter is very close to forward scatter (around 50% for each) for the high resolution case with $Re_\ell = 10900$ and $Fr_\ell = 0.16$. This trend suggests that the local volume fraction of backscatter is as important as that in forward scatter in stratified turbulence (in line with the results for isotropic turbulence, e.g. Piomelli et al., 1991).

Effects of changing the test cutoff k_c

Figure 5.6 shows the effects of using different test cutoffs on the up- and downscale energy transfer. Results from a smaller cutoff wavenumber $k_c = 20$ (black) are compared to results for the larger cutoff $k_c = 40$ (grey). For early times, the forward- and backscatter are slightly larger for $k_c = 20$ compared to those for $k_c = 40$. However, as time evolves towards the turbulence commencement, the up- and downscale transfers get slightly larger for the larger cutoff wavenumber $k_c = 40$. Overall, the effects of changing the test cutoff k_c are negligible on time series of the forward- and backscatter in the physical space (figure 5.6). These trends might be a sign of self similarity of energy transfer in the physical space in the spherical direction k. Similar trends in which forward- and backscatter are almost independent to the filter width is are reported for unstratified turbulence (Piomelli et al.,

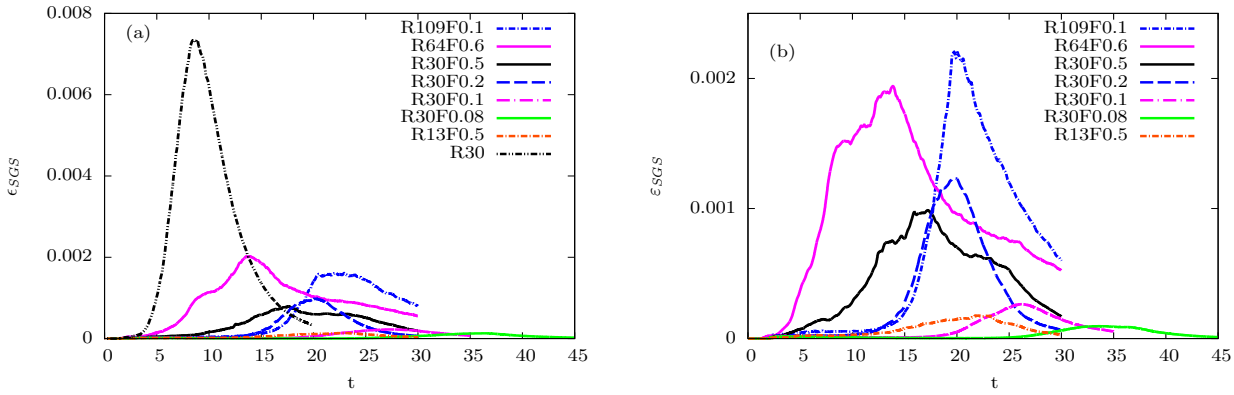

Figure 5.5: Time series of the effective SGS dissipation rate for $k_c = 40$: (a) kinetic and (b) potential.

1991).

5.4.3 Energy transfer in wavenumber space

The averaged effective SGS kinetic and potential energy transfer spectra for $k_c = 40$ are shown in figures 5.7(a) and (b), respectively. According to our definitions in equations (5.16,5.17) from the filtered equations of motion (5.7-5.9), positive values of $\langle T_k(k|k_c,t)\rangle$ and $\langle T_p(k|k_c,t)\rangle$ present downscale energy transfer from above to below the filter scale, and negative values denote backscatter. For the unstratified simulation and the stratified case with $Re_\ell = 6400$ and $Fr_\ell = 0.64$, no signs of backscatter are observed. However, increased stratification along with decreased resolution results in the upscale transfer of kinetic energy over $0.1 \lesssim k/k_c \lesssim 0.7$ (figure 5.7a). These trends suggest that by reducing the buoyancy Reynolds number Re_b to be around 1 or even smaller, backscatter emerges in stratified turbulence over an intermediate range of wavenumbers. Such behaviours are not seen in the effective SGS potential energy transfer spectra (figure 5.7b).

The averaged horizontal and vertical effective SGS kinetic and potential energy transfer spectra for the case with $Re_\ell = 3030$ and $Fr_\ell = 0.24$ are shown in figure 5.8. It is interesting that the upscale kinetic energy transfer, which was shown in figure 5.7(a), happens at large horizontal and small vertical scales (figure 5.8a). To further examine this backscatter, and in particular its dependence on Reynolds number, we have performed a series of simulations in which the initial Reynolds number is increased at fixed initial Froude number, thereby increasing the buoyancy Reynolds number. In particular, we consider cases with $Fr_\ell \approx 0.1$

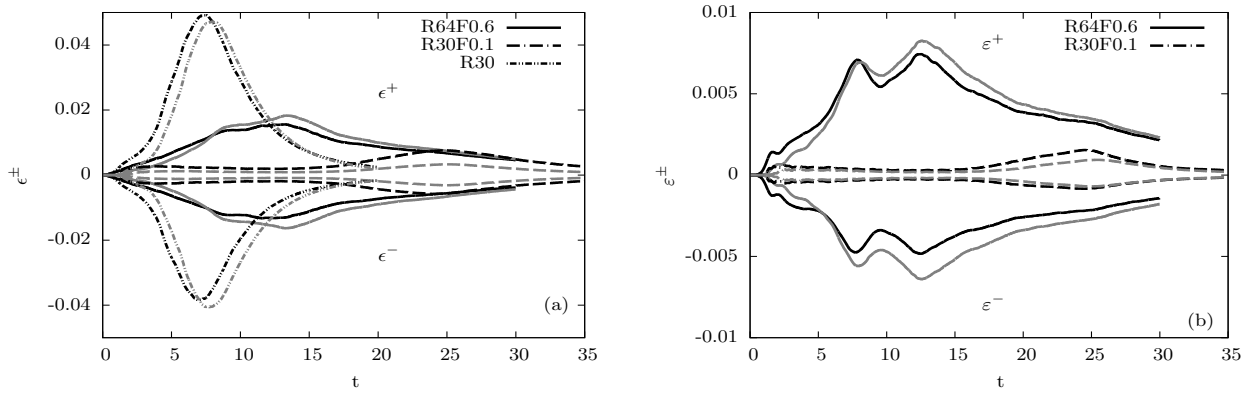

Figure 5.6: Time series of forward- and backscatter components of the effective SGS dissipation rate for $k_c = 20$ (black colour) and $k_c = 40$ (grey colour): (a) kinetic and (b) potential.

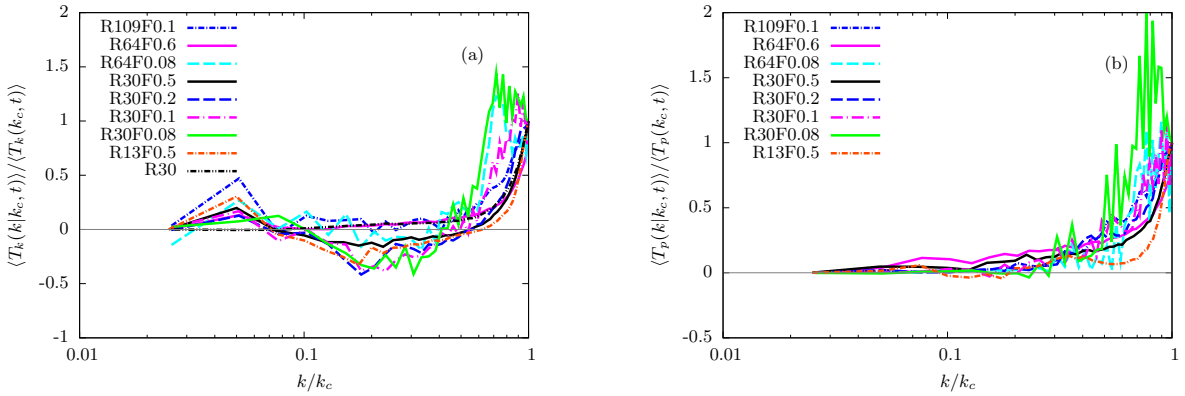

Figure 5.7: Averaged effective SGS (a) kinetic and (b) potential energy transfer spectra for $k_c = 40$. The solid grey line indicates zero.

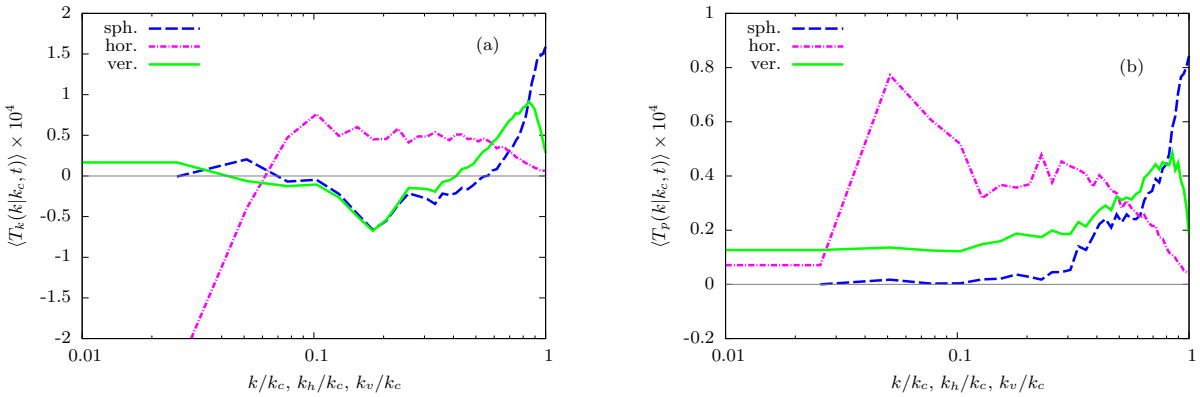

Figure 5.8: Averaged horizontal and vertical wavenumber effective SGS (a) kinetic and (b) potential energy transfer spectra for the case with $Re_\ell = 3030$ and $Fr_\ell = 0.24$, when $k_c = 40$. The spherical labels show those corresponding curves that were shown in figure 5.7.

and $Re_\ell = 3030$, 6400 and 10900. Interestingly, increased Reynolds number leads to decreasing, and finally an elimination, of the backscatter (see solid green, dashed cyan and dot-dashed blue lines in figure 5.7a). In addition, the horizontal and vertical effective SGS potential energy transfer spectra do not show an upscale energy transfer (figure 5.8b).

At low $Re_b \lesssim 1$, stratified turbulence has a viscously layered structure, with vertical layer thickness of $L_{visc} = l_h/\sqrt{Re}$, below which viscous effects are important (e.g. Brethouwer et al., 2007). In these three simulations $L_{visc} \approx 0.04$, 0.06 and 0.83 when $Re_\ell = 10900$, 6400 and 3030, respectively. As a result, test filter scales are clearly affected by viscosity at the smaller Re, less so at the larger Re. If we compare L_{visc} with the test-filter width $\Delta_{test} \sim 1/k_c$, which is 0.025 for $k_c = 40$, it is clear that as L_{visc} decreases towards Δ_{test} with increasing Re, backscatter is eliminated. We speculate that there may be a similar relation for the viscous scale and test-filter width in DNS of Remmler & Hickel (2014), who have also reported backscatter in DNS of stratified turbulence. Using $l_h = 2\pi$ in their strongly stratified case, we can get $L_{visc} \approx 0.03$, which is very close to the test-filter width in their simulation (see Remmler & Hickel, 2014). As a result, the upscale energy transfer in wavenumber space could be due to viscous effects rather than a turbulent mechanism. These findings suggest that the presence of upscale energy transfer, which is reported by Remmler & Hickel (2014), could be due to effects of the low Reynolds number.

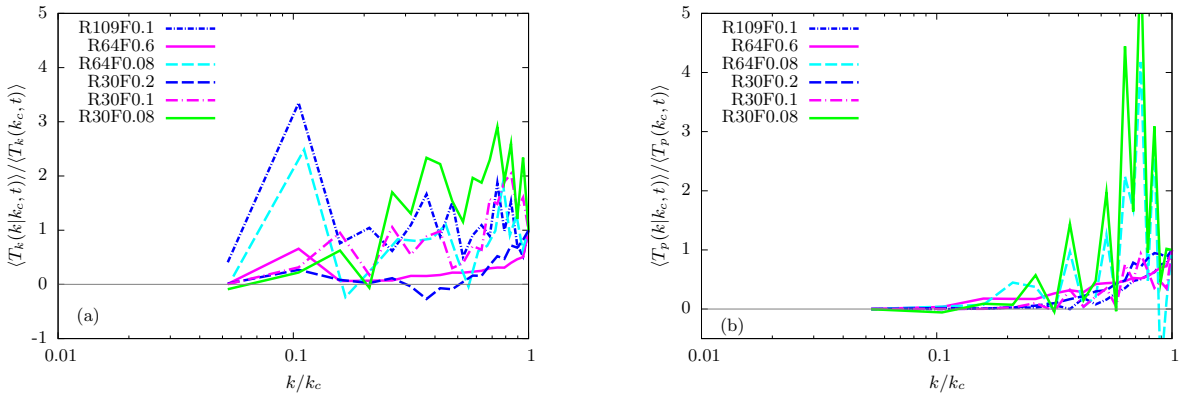

Figure 5.9: Averaged effective SGS (a) kinetic and (b) potential energy transfer spectra for $k_c = 20$. The solid grey line indicates zero.

Effects of changing the test cutoff k_c

By changing the location of the test cutoff wavenumber k_c from 40 to 20, effective SGS kinetic and potential energy transfers change dramatically (figure 5.9). The magnitudes of effective SGS energy transfers are increased using smaller k_c. In addition, the effective SGS kinetic energy transfer presents no or very small backscatter. As a result, by moving the test cutoff k_c towards small wavenumbers, the upscale energy transfer is reduced or avoided. For example, stratified cases with $Re_\ell = 3030$ and $Fr_\ell = 0.1$, 0.08, present no backscatter when $k_c = 20$, in contrast with the corresponding results when $k_c = 40$ (figure 5.7a). These trends suggest that the upscale energy transfer happens from sub-test-filter scales towards the smaller test-resolved scales (see figures 5.7 and 5.9).

5.4.4 The effective turbulent Prandtl number

Figure 5.10 shows the averaged effective turbulent Prandtl number $\langle Pr_t(k|k_c,t)\rangle$ spectra at different test cutoffs k_c. The case with $Re_\ell = 6400$ and $Fr_\ell = 0.64$ shows positive values that are between 0 and 1, for both test cutoff $k_c = 20$ and 40 (solid purple lines in figures 5.10a,b). However, all other cases show negative $\langle Pr_t(k|k_c,t)\rangle$ spectra over the intermediate range $0.1k_c \lesssim k \lesssim 0.6k_c$. By moving k_c from 40 to 20, negative $\langle Pr_t(k|k_c,t)\rangle$ values are decreased for cases with $Re_\ell = 3030$ and $Fr_\ell = 0.24$, 0.12 (figures 5.10a,b). Nevertheless, cases with $Fr_\ell = 0.08$ and $Re_\ell = 6400$, 3030 still show large negative values of $\langle Pr_t(k|k_c,t)\rangle$. It is interesting that for all cases, the averaged effective turbulent Prandtl

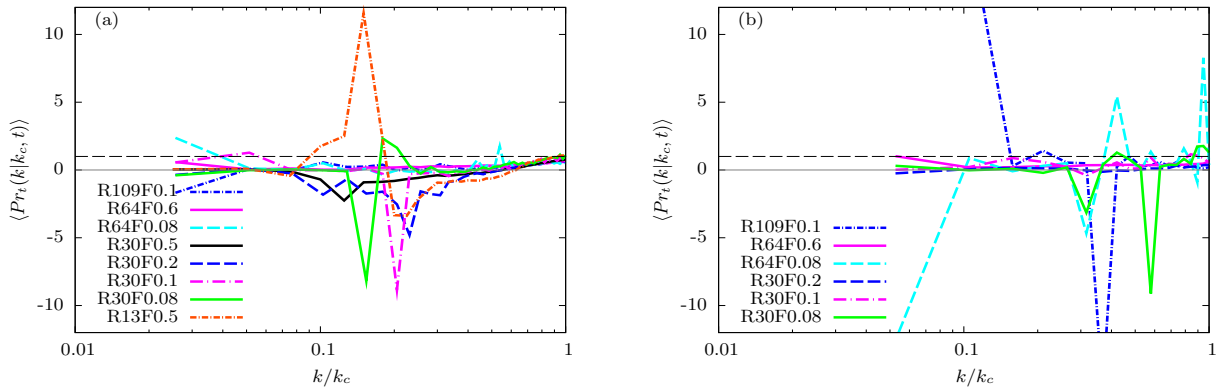

Figure 5.10: Averaged effective turbulent Prandtl number spectra for (a) $k_c = 40$ and (b) $k_c = 20$. The solid grey line and dashed black line indicate values of zero and 1, respectively.

number is positive and fairly close to 1 around the test cutoff $k \approx k_c$. This trend might suggest that the assumption of $Pr_t \approx 1$ is reasonable for the local energy transfer at all regimes of Re_b (as is assumed in e.g. Siegel & Domaradzki, 1994; Khani & Waite, 2014a). However, by decreasing Re_b to be of order ~ 1 or $\ll 1$, this assumption might not be valid for the nonlocal energy transfer (similar behaviours are investigated by Remmler & Hickel, 2014).

5.5 Conclusion

The dynamics of kinetic and potential energy transfer in both physical and wavenumber space for decaying stratified turbulence is studied in this chapter. The effective SGS energy transfer ϵ_{SGS} is a small net energy transfer from large to small scales that is deduced from the combination of two large energy transfer mechanisms: downscale ϵ^+ and upscale ϵ^- (in line with results for unstratified simulations, e.g. Piomelli et al., 1991). Increased buoyancy Reynolds number Re_b leads to an increase in the upscale and downscale kinetic and potential energy transfer, and hence increasing effective SGS energy transfer in physical space. As a result, upscale energy transfer might not be just a random and stochastic process that is independent of the flow dynamics, as is considered for modelling backscatter in the literature (e.g. Lesieur, 1990; Chasnov, 1991; Marstorp et al., 2007; Weinbrecht & Mason, 2008). Our results show that backscatter depends on the parameters of stratified turbulence such as buoyancy frequency, resolution and the buoyancy Reynolds number.

A similar idea is suggested by O'Brien et al. (2014), in which backscatter in reacting turbulence depends on the dynamics of the flow such as the SGS Mach number and high-speed compressibility.

In wavenumber space, the effective kinetic and potential energy transfer spectra are positive (i.e. forward scatter) when $Re_b \sim O(10)$. However, for $Re_b \sim O(1)$ or smaller, the kinetic energy transfer spectra show negative values (i.e. backscatter) when the Reynolds number is small. We found that this behaviour occurs when the test filter scale falls below the scale of the viscous layers that are present at small Re_b. These trends suggest that the effective kinetic energy transfer spectra are contaminated by viscous effects in the small Reynolds number regime, for which the non-local backscatter are seen in the effective kinetic energy transfer spectra. The effective turbulent Prandtl number spectra suggest that the assumption of $Pr_t = 1$ is reasonable for the local energy transfer. For the nonlocal energy transfer, however, the effective $\langle Pr_t \rangle$ is negative when $Re_b \sim O(1)$ or smaller.

Performing DNS of stratified turbulence for large and small Re_b, when the Reynolds number is very large is a potential direction for future work, so that the dynamics of energy transfer around the buoyancy and Ozmidov scales could be studied in detail, and away from the effects of molecular viscosity.

Chapter 6

Conclusion

6.1 Concluding remarks

In Chapter 2, we performed an *a priori* test on DNS of stratified turbulence to study the dynamics of actual small-scale motions and the energy transfer around the Ozmidov length scale. Transfers between scales larger and smaller than a test filter scale were analyzed, and filters were applied separately in the horizontal and vertical directions. This systematic analysis allows one to directly compare the isotropic Kraichnan eddy viscosity with the effective eddy viscosity in stratified turbulence. Due to the layerwise structures of turbulent flows that are subjected to strong stratification, an anisotropic framework, involving horizontal and vertical eddy viscosities, is outlined in this chapter. It is shown that the horizontal and vertical eddy viscosities are fairly similar in the non-stratified case, as expected. However, the presence of stratification changes the shape of directional effective eddy viscosity significantly, when the test cutoff k_c is around or smaller than k_o. The energy transfer spectra also change in the presence of strong stratification. In particular, the horizontal energy transfer shows a non-local contribution from large to small horizontal scales and a short cusp. This non-local energy transfer in the horizontal direction of stratified turbulence occurs at large vertical wavenumbers (i.e. local in the total wavenumber direction) and is not seen in the vertical direction or in the non-stratified cases. Changing the test cutoff wavenumber k_c has a significant effect on the effective eddy viscosity. By increasing k_c towards the dissipation scale, the non-local horizontal energy transfer decreases while the local energy transfer around k_c increases. The results of chapter 2 suggest that the current isotropic SGS models might not be a proper choice for LES of stratified turbulence when $k_c \lesssim k_o$. For the next two chapters we evaluate current

SGS models in the physical and wavenumber space.

Chapter 3 investigated the performance of two common isotropic SGS models (i.e. the Smagorinsky and Kraichnan models) in LES of stratified turbulence when $k_c < k_o$. It is shown that when the grid spacing Δ is small enough, the horizontal wavenumber spectra have an almost $-5/3$ slope along with a bump near k_b. In this situation, increased stratification or decreased resolution prohibits KH instabilities by shrinking the thickness of vertical layers towards the dissipation range or by increasing the dissipation scale, respectively. A threshold on Δ is presented for which the dynamics of stratified turbulence are captured when $k_c < k_o$. This threshold depends on the buoyancy scale L_b and changes with different SGS models. The Smagorinsky model needs $\Delta < 0.17L_b$ while the Kraichnan model requires $\Delta < 0.47L_b$. As a result, the Smagorinsky model is significantly more expensive than the Kraichnan model since the former model requires grid spacing Δ which is three times smaller than the latter one to give the same results.

The results of chapter 3 show that, not surprisingly, isotropic SGS model definitely fail to resolve the dynamics of stratified turbulence when $\Delta > L_b$. However, it is interesting to note that these SGS models perform well if the buoyancy scale is resolved even when $k_c < k_o$. In other words, the isotropic SGS models successfully capture the dynamics of stratified turbulence when the cutoff wavenumber k_c is larger than k_b. This criteria has significant implications for the computational costs, especially for large buoyancy frequency N since it implies that resolving k_b and not k_o may be sufficient for LES of stratified turbulence. Nevertheless, LES of stratified turbulence is expensive since it still requires resolution of L_b, which is the layer thickness and therefore may be many times smaller than the energy-containing scale. The question here is then: how can we improve the disappointing performance of Smagorinsky LES, which is a common choice in applications, in stratified turbulence? It is worthwhile to recall that the applicability of the Kraichnan model is limited to idealized cases with triply periodic boundary conditions.

In chapter 4, the performance of the Smagorinsky model was improved using a dynamic subgrid scale approach. In this approach, the Smagorinsky coefficient c_s is not assumed to be constant and is determined using the dynamics at resolved scales. Results show that the criterion $\Delta/L_b < 0.24$ is sufficient for the dynamic Smagorinsky model to capture the basic dynamical features of stratified turbulence. This criterion suggests a larger grid spacing may be used for the dynamic model compared to the regular Smagorinsky model. It was shown in figure 4.4 that the dynamic SGS model improves the performance of the Smagorinsky model by increasing the maximum grid spacing by almost a factor of two. In addition, our results demonstrate that the c_s fields show layerwise structures in the presence of stratification. In addition, larger values of c_s are corresponding to regions with smaller shears, and also c_s values are very small at regions with large shears.

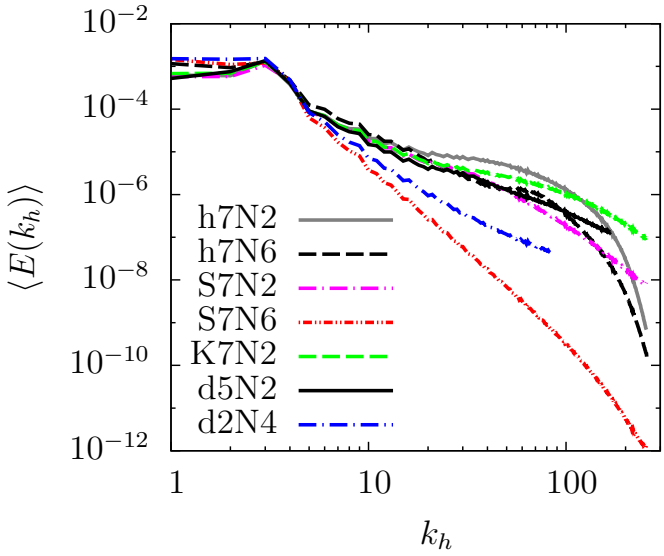

Figure 6.1: The averaged horizontal wavenumber energy spectra at different resolutions and buoyancy frequencies for all SGS models.

The performance of all the SGS models considered here are summarized in figure 6.1, where the horizontal wavenumber spectra at different buoyancy frequencies and resolutions are shown. As already known, the high resolution Smagorinsky LES with $N = 6$ shows the steepest slope, which is even steeper than the low resolution dynamic Smagorinsky LES with $N = 4$. At the large horizontal wavenumbers (i.e. $k_h \gtrsim 100$), the Kraichnan LES is less dissipative than the hyperviscosity simulation. For large horizontal scales (i.e. $k_h \lesssim 40$), the dynamic Smagorinsky LES with $n = 512$ and $N = 2$ is very similar to the high resolution Kraichnan LES with the same buoyancy frequency. All the high resolution cases with buoyancy frequency $N = 2$ show an inertial subrange with a slope close to $-5/3$ along with a bump around k_b. As the buoyancy frequency N increases or resolution decreases, significant differences in small resolved scales appear. It is worthwhile to recall that large scales seem to be robust to the choice of SGS models.

In chapter 5, we analyzed DNS results of stratified turbulence to directly measure forward- and backscatter in both physical and wavenumber spaces. Increased stratification or decreased resolution decreases the effective upscale and downscale SGS energy transfer in physical space. The effects of changing the test cutoff k_c are negligible on forward- and backscatter. This trend might be a sign of self-similar up- and downscale energy transfer

in physical space. The effective SGS kinetic energy transfer spectra may get contaminated by viscous effects for small Reynolds numbers. As a result, the effective spectral turbulent Prandtl number at intermediate length scales might become negative for small Reynolds numbers. Also, our results show that the assumption of $Pr_t = 1$ is reasonable for local energy transfer.

In summary, this thesis includes both *a priori* and *a posteriori* tests in numerical simulations of stratified turbulence. The presence of stratification has important effects on turbulent eddies at both resolved and sub-grid scales. LES of stratified turbulence requires resolution of the buoyancy scale to capture dynamical features of turbulent motions. Although the SGS models considered here are isotropic, the eddy dissipation spectra show anisotropic behaviours due to anisotropy in the rate of strain $\bar{s}_{ij}$, which is used in modelling SGS motions. Upscale energy transfer depends on the flow parameters such as the buoyancy Reynolds number.

6.2 Future work

DNS and LES of stratified turbulence in idealized cases are studied in this thesis where the buoyancy frequency is constant. It would be interesting to investigate performance of LES in conditions where N varies with height, e.g. the atmospheric boundary layer. We might need higher resolution in the regions with larger N. Also, it is interesting to consider other phenomena in the atmosphere and ocean such as clouds, topography and urban canopies.

In addition, resolving the buoyancy scale L_b may not be possible in some cases (at least in the horizontal direction) because of computational expense. For example, a typical L_b in the atmosphere is order of $\mathcal{O}(100)$ m (e.g. Waite, 2014), which is almost impossible to be resolved in the horizontal direction when the domain is large. As a result, designing an anisotropic SGS model for LES of stratified turbulence seems to be a necessary step in reducing the computational costs of simulating more complex flows in the atmosphere and ocean. The results of chapter 4 suggest that the dynamic SGS model could be a solid basis for addressing the anisotropic behaviours of stratified turbulence.

Ultimately, while it is known that DNS is an expensive approach for studying stratified turbulence, high resolution DNS are required to learn more about the dynamics of energy transfer between large and small scales subjected to a large inertial subrange. Of course, the *a priori* testing on such a high resolution DNS would be very helpful in designing a robust anisotropic SGS model for LES of stratified turbulence.

Appendices

Appendix A

Energy budget in DNS

Let us consider the momentum and energy equations (2.11,2.13) subjected to equations (2.14,2.15) as follows

$$(\frac{\partial}{\partial t}+\frac{k^2}{Re_\ell})\hat{u}_j(\boldsymbol{k},t)+\frac{1}{{Fr_\ell}^2}\hat{\rho}(\boldsymbol{k},t)\boldsymbol{e}_z=F_j(\boldsymbol{k},t), \tag{A.1}$$

$$(\frac{\partial}{\partial t}+\frac{k^2}{Re_\ell Pr})\hat{\rho}(\boldsymbol{k},t)-\hat{w}(\boldsymbol{k},t)=J(\boldsymbol{k},t), \tag{A.2}$$

multiply equations (A.1,A.2) by the complex conjugate of velocity and density fields, respectively to get

$$\hat{u}_j^*(\boldsymbol{k},t)(\frac{\partial}{\partial t}+\frac{k^2}{Re_\ell})\hat{u}_j(\boldsymbol{k},t)+\frac{1}{{Fr_\ell}^2}\hat{w}^*(\boldsymbol{k},t)\hat{\rho}(\boldsymbol{k},t)=\hat{u}_j^*(\boldsymbol{k},t)F_j(\boldsymbol{k},t), \tag{A.3}$$

$$\hat{\rho}^*(\boldsymbol{k},t)(\frac{\partial}{\partial t}+\frac{k^2}{Re_\ell Pr})\hat{\rho}(\boldsymbol{k},t)-\hat{\rho}^*(\boldsymbol{k},t)\hat{w}(\boldsymbol{k},t)=\hat{\rho}^*(\boldsymbol{k},t)J(\boldsymbol{k},t). \tag{A.4}$$

Similarly, we can multiply $\hat{u}_j(\boldsymbol{k},t)$ and $\hat{\rho}(\boldsymbol{k},t)$ by the complex conjugate of (A.1,A.2), respectively, and add them to (A.3,A.4), respectively, yielding

$$(\frac{\partial}{\partial t}+\frac{2k^2}{Re_\ell})\hat{u}_j\hat{u}_j^*+\frac{1}{{Fr_\ell}^2}(\hat{w}^*\hat{\rho}+\hat{w}\hat{\rho}^*)=\hat{u}_j^*F_j+\hat{u}_j^*F_j, \tag{A.5}$$

$$(\frac{\partial}{\partial t}+\frac{2k^2}{Re_\ell Pr})\hat{\rho}\hat{\rho}^*-(\hat{\rho}^*\hat{w}+\hat{\rho}\hat{w}^*)=\hat{\rho}^*J+\hat{\rho}J^*, \tag{A.6}$$

where we have suppressed the dependence on $\boldsymbol{k}$ and t for clarity. Let us define the kinetic and potential energy spectrum respectively by

$$E_k(\boldsymbol{k},t) = \frac{1}{2}\hat{u}_j(\boldsymbol{k},t)\hat{u}_j^*(\boldsymbol{k},t), \tag{A.7}$$

$$E_p(\boldsymbol{k},t) = \frac{1}{2Fr_\ell{}^2}\hat{\rho}(\boldsymbol{k},t)\hat{\rho}^*(\boldsymbol{k},t), \tag{A.8}$$

therefore, equations (A.5,A.6) can be rewritten as follows

$$(\frac{\partial}{\partial t} + \frac{2k^2}{Re_\ell})Ek(\boldsymbol{k},t) + B(\boldsymbol{k},t) = T(\boldsymbol{k},t), \tag{A.9}$$

$$(\frac{\partial}{\partial t} + \frac{2k^2}{Re_\ell Pr})Ep(\boldsymbol{k},t) - B(\boldsymbol{k},t) = Tp(\boldsymbol{k},t), \tag{A.10}$$

where $B = 1/(2Fr_\ell^2)(\hat{w}^*\hat{\rho} + \hat{w}\hat{\rho}^*)$ is the buoyancy flux and $T(\boldsymbol{k},t)$ and $Tp(\boldsymbol{k},t)$ show the kinetic and potential energy transfer between scales. Since DNS resolves all scales from large energy containing scale k_i down to the Kolmogorov scale k_d, we can conclude that

$$\sum_{k=k_i}^{k_d} T(\boldsymbol{k},t)d\boldsymbol{k} = 0, \tag{A.11}$$

$$\sum_{k=k_i}^{k_d} Tp(\boldsymbol{k},t)d\boldsymbol{k} = 0, \tag{A.12}$$

because they transfer kinetic and potential energy conservatively between scales.

Appendix B

Energy budget in LES

Let us consider the momentum and energy equations (3.16,3.18) along with equations (3.19-3.22), written as

$$\frac{\partial}{\partial t}\hat{\bar{u}}_j(\boldsymbol{k},t) + \frac{1}{{Fr_\ell}^2}\hat{\bar{\rho}}(\boldsymbol{k},t)\boldsymbol{e}_z = \bar{F}_j(\boldsymbol{k},t) + F^s_j(\boldsymbol{k},t) + \hat{\bar{f}}_j, \tag{B.1}$$

$$\frac{\partial}{\partial t}\hat{\bar{\rho}}(\boldsymbol{k},t) - \hat{\bar{w}}(\boldsymbol{k},t) = \bar{J}(\boldsymbol{k},t) + J^s(\boldsymbol{k},t). \tag{B.2}$$

If we multiply (B.1) and (B.2) by the complex conjugate of velocity and density fields, respectively, we get (suppressing dependence on $\boldsymbol{k}$ and t for clarity)

$$\hat{\bar{u}}^*_j\frac{\partial}{\partial t}\hat{\bar{u}}_j + \frac{1}{{Fr_\ell}^2}\hat{\bar{u}}^*_j\hat{\bar{\rho}}\boldsymbol{e}_z = \hat{\bar{u}}^*_j\bar{F}_j + \hat{\bar{u}}^*_j F^s_j + \hat{\bar{u}}^*_j\hat{\bar{f}}_j, \tag{B.3}$$

$$\hat{\bar{\rho}}^*\frac{\partial}{\partial t}\hat{\bar{\rho}} - \hat{\bar{\rho}}^*\hat{\bar{w}} = \hat{\bar{\rho}}^*\bar{J} + \hat{\bar{\rho}}^* J^s. \tag{B.4}$$

Let us multiply velocity and density fields to the complex conjugate of (B.1,B.2), respectively, and then add them to (B.3,B.4), respectively, as follows

$$\frac{\partial(\hat{\bar{u}}^*_j\hat{\bar{u}}_j)}{\partial t} + \frac{1}{{Fr_\ell}^2}(\hat{\bar{w}}^*\hat{\bar{\rho}} + \hat{\bar{w}}\hat{\bar{\rho}}^*) = (\hat{\bar{u}}^*_j\bar{F}_j + \hat{\bar{u}}_j\bar{F}^*_j) + (\hat{\bar{u}}^*_j F^s_j + \hat{\bar{u}}_j F^{s*}_j) + (\hat{\bar{u}}^*_j\hat{\bar{f}}_j + \hat{\bar{u}}_j\hat{\bar{f}}^*_j), \tag{B.5}$$

$$\frac{\partial(\hat{\bar{\rho}}^*\hat{\bar{\rho}})}{\partial t} - (\hat{\bar{\rho}}^*\hat{\bar{w}} + \hat{\bar{\rho}}\hat{\bar{w}}^*) = (\hat{\bar{\rho}}^*\bar{J} + \hat{\bar{\rho}}\bar{J}^*) + (\hat{\bar{\rho}}^* J^s + \hat{\bar{\rho}}J^{s*}). \tag{B.6}$$

If we define the kinetic energy spectrum and the potential energy spectrum as in (A.7,A.8), then equations (B.5,B.6) can be written as

$$\frac{\partial EK(\boldsymbol{k},t)}{\partial t} + B(\boldsymbol{k},t) = T_r(\boldsymbol{k},t) + T_s(\boldsymbol{k},t) + P_w(\boldsymbol{k},t), \tag{B.7}$$

$$\frac{\partial EP(\boldsymbol{k},t)}{\partial t} - B(\boldsymbol{k},t) = TP_r(\boldsymbol{k},t) + TP_s(\boldsymbol{k},t). \tag{B.8}$$

where

$$B(\boldsymbol{k},t) = \frac{1}{2Fr_\ell{}^2}(\hat{\bar{w}}^*\hat{\bar{\rho}} + \hat{\bar{w}}\hat{\bar{\rho}}^*), \tag{B.9}$$

$$\tag{B.10}$$

is the buoyancy flux and

$$T_r(\boldsymbol{k},t) = \frac{1}{2}(\hat{\bar{u}}_j^*\bar{F}_j + \hat{\bar{u}}_j\bar{F}_j^*), \tag{B.11}$$

$$T_s(\boldsymbol{k},t) = \frac{1}{2}(\hat{\bar{u}}_j^*F_j^s + \hat{\bar{u}}_jF_j^{s*}), \tag{B.12}$$

are the resolved kinetic energy flux and the energy transfer to dissipation scales, respectively. Similar results hold for $Tp_r(\boldsymbol{k},t)$ and $Tp_s(\boldsymbol{k},t)$ in the potential energy budget. In appendix C, we show how we can compute the eddy dissipation spectra and the spectral effective eddy viscosity when $T_s(\boldsymbol{k},t)$ is modelled using the eddy-viscosity hypothesis (see chapter 3).

Appendix C

Eddy dissipation spectra

Let us consider $\hat{\boldsymbol{m}}(\boldsymbol{k},t)$ as the Fourier transform of the eddy dissipation term $-\nabla\cdot\boldsymbol{\tau}^r(\boldsymbol{x},t)$ as follows

$$-\nabla\cdot\boldsymbol{\tau}^r(\boldsymbol{x},t)=\sum_{\boldsymbol{k}}\hat{\boldsymbol{m}}(\boldsymbol{k},t)e^{i\boldsymbol{k}\cdot\boldsymbol{x}}. \tag{C.1}$$

We can multiply $\hat{\boldsymbol{m}}(\boldsymbol{k},t)$ with the complex conjugate of velocity coefficient $\hat{\boldsymbol{u}}(\boldsymbol{k},t)$ and add the result to the product of the complex conjugate of $\hat{\boldsymbol{m}}(\boldsymbol{k},t)$ with $\hat{\boldsymbol{u}}(\boldsymbol{k},t)$ as follows

$$T_s(\boldsymbol{k},t)=\hat{m}_i(\boldsymbol{k},t)\hat{u}_i^*(\boldsymbol{k},t)+\hat{m}_i^*(\boldsymbol{k},t)\hat{u}_i(\boldsymbol{k},t), \tag{C.2}$$

where $T^r(\boldsymbol{k},t)$ is the eddy dissipation in the kinetic energy budget and also shows the amount of energy that transfers from resolved scales to the subgrid scales. The eddy dissipation term $T^r(\boldsymbol{k},t)$ may be divided by twice the energy spectrum to get the effective spectral eddy viscosity for LES as follows

$$\nu(\boldsymbol{k},t)=-\frac{T_s(\boldsymbol{k},t)}{2E(\boldsymbol{k},t)}. \tag{C.3}$$

Equation (C.3) could be binned over constant k or k_h or k_v and averaged over time to get the one dimensional effective spectral eddy viscosities

$$\nu(k)=\frac{\sum_{|\boldsymbol{k}|=k}\langle\nu(\boldsymbol{k},t)\rangle}{k^2}, \tag{C.4}$$

$$\nu(k_h)=\frac{\sum_{|\boldsymbol{k}|=k_h}\langle\nu(\boldsymbol{k},t)\rangle}{k_h^2}, \tag{C.5}$$

$$\nu(k_v)=\frac{\sum_{|\boldsymbol{k}|=k_v}\langle\nu(\boldsymbol{k},t)\rangle}{k_v^2}, \tag{C.6}$$

where subscripts h and v denote the horizontal and vertical directions. Similarly, we get the one dimensional horizontal and vertical eddy dissipation spectra $\langle T_s(k_h)\rangle$ and $\langle T^s(k_v)\rangle$ by binning the eddy dissipation spectra $T_s(\boldsymbol{k}, t)$ over constant k_h and k_v, respectively.

Copyright Permission

Copyright permits have been attached here.

CAMBRIDGE UNIVERSITY PRESS

(Doc.JCT.T&C.STM.14.1)

Terms and Conditions for authors to Scientific, Technological and Medical journals published by Cambridge University Press.

By completing, signing and returning the Copyright Transfer form (Form JCT.14.1) you have agreed to abide by the following Terms and Conditions. Please retain this document for future reference.

Definitions[37]

Author's Original (AO)	Any version of the article that is considered by you to be of sufficient quality to be submitted for formal peer review by a second party. Content and layout as set out by you.
Submitted Manuscript Under Review (SMUR)	Any version of the article that is under formal review for inclusion in the journal. Content and layout follow the journal's stated submission requirements.
Accepted Manuscript (AM)	The version of the article that has been accepted for publication in the journal. This version may have been revised following peer review but may be subject to further editorial input by Cambridge University Press.
Version of Record (VoR)	The fixed version of the article that has been made available. This includes an "early release" article as long as it is citable via some permanent identifier(s). This does **not** include any "early release" article that has not yet been "fixed" by processes that are still to be applied, such as copy-editing or proof corrections. The VoR includes any corrected or enhanced VoR.
Personal Website	A non-commercial website maintained solely or in part by you.
Departmental / Institutional Repository	The online archive of intellectual output of the institution at which you were based when the article was written as well the repository of any future institution at which you are based.
Non-commercial Subject Repository	A repository relating to the subject area of your article which does not allow the content to be used commercially.
Commercial Repository	A repository which permits the content to be used for commercial gain.
Social Media Sites	Websites and computer programs that allow people to communicate and share information on the internet using a computer or mobile phone[38]

Re-use of your article.

All postings shall include a prominent bibliographical reference and statement of copyright ownership. Where possible all postings should include a link to the published article on Cambridge Journals Online. In relation to the posting of the AO or SMUR, a statement that such version has been accepted for publication and will appear in a revised form subsequent to peer

[37] Adapted from NISO RP-8-2008, Copyright © 2008 by the National Information Standards Organization
[38] http://dictionary.cambridge.org/dictionary/british/social-media?q=social+media&utm_medium=widget_searchbox&utm_source=widget_searchbox_source&utm_campaign=widget_tracking

review and / or editorial input by Cambridge University Press and / or the journal's proprietor ,as well as a link to the journal's site on Cambridge Journals Online, should be included.

Cambridge does not permit full articles in AM or VOR form to be posted on Commercial Repositories or Social Media Sites including, but not limited to, Social Science Research Network ('SSRN'), ResearchGate, Academia.edu, Mendeley or LinkedIn.

Notwithstanding the assignment of copyright or grant of licence in your article, you retain the following non-transferable rights to deposit versions of your article, (subject to appropriate permission having been cleared for any third-party material):

	Personal Website	**Departmental / Institutional Repository**	**Non-commercial Subject Repository**	**Commercial Repository and Social Media Sites**
AO	At any time	At any time	At any time	At any time
SMUR	At any time	At any time	At any time	At any time
AM	On acceptance of publication.	Six months after first publication.	Six months after first publication	Abstract only in PDF or HTML format no sooner than first publication of the full article.
VOR	Abstract only in PDF or HTML format no sooner than first publication of the full article.	Abstract only in PDF or HTML format no sooner than first publication of the full article.	Abstract only in PDF or HTML format no sooner than first publication of the full article.	Abstract only in PDF or HTML format no sooner than first publication of the full article.

Other

You may make hard copies of the article or an adapted version for your own purposes, including the right to make multiple copies for course use by your students, provided no sale is involved.

You may reproduce the article or an adapted version of it in any volume of which you are editor or author subject to normal acknowledgement.

If your reuse is not covered by the above please follow the 'Rights and Permissions' quick link on the Cambridge website for your region via www.cambridge.org.

Cambridge University Press co-operates in various licensing schemes that allow material to be photocopied within agreed restraints (e.g. the CCC in the USA and the CLA in the UK). Any proceeds received from such licences, together with any proceeds from sales of subsidiary rights in the Journal, directly support its continuing publication.

Cambridge University Press acts in accordance with the UK Bribery Act 2010 and the Data Protection Act 1998. Please refer to the Press's relevant policies, (http://www.cambridge.org/policy/privacy/), (http://www.cambridge.org/policy/abc_policy/) which may be revised from time to time.

Search: GO

Taylor & Francis
Author Services

Page content

View the page content by selecting any of the links below

You are in: Home > Copyright > Copyright and you

Copyright and you

Skip to navigation

What is copyright?

Copyright gives the copyright holder exclusive rights over how others use their work.

As an author, this means that which copyright option you choose defines how researchers, scientists, policy makers, journalists, corporations, or anyone else who has an interest in your research can use your work.

Copyright has a time limit (usually life of the author plus 50–70 years for a journal article) and the level and type of protection offered varies between countries. Local and international laws and conventions mean that the copyright is recognized and protected, to varying degrees, in almost every country in the world.

In a digital world, how others want to read and reuse content is evolving rapidly. Understanding what your copyright options are is becoming ever more important, especially with the growth of open access publishing.

back to top

What does it mean for you?

Copyright allows you to protect your original material and stop others from using your work without your permission. It means others will generally need to credit you and your work properly, increasing its impact.

back to top

Copyright at Taylor & Francis

When publishing in a subscription journal published by Taylor & Francis, we ask you to assign copyright to us. Alternatively, any author publishing with us can also opt to retain their own copyright and sign a License to Publish (sample).

If you choose to assign copyright to us, as part of the publication process, you will be asked to sign a publishing agreement. This will be after your manuscript has been through the peer review process, has been accepted, and moves into production. Details will be sent to you via email, from the journal's Production Editor.

Sample publishing agreement

Find out more about what defines a conflict of interest and how to declare it

back to top

Why do we ask you to assign copyright to us?

Asking you to assign copyright means we are showing our commitment to:

- Act as **stewards** of the scholarly record of your work
- **Defend** your article against plagiarism and copyright infringement
- Enable you to **share** your article (using your free eprints and Green Open Access at Taylor & Francis)
- Assure attribution of your work, by making sure you are **identified** as the author

We encourage you to:

- **Share** your work
- Make **printed copies** of your article to use for lecture or classroom purposes
- Include your article in a thesis or dissertation
- **Present your article at a meeting or conference** and distribute printed copies of the article
- Republish the article (making sure you cite the original article)
- Adapt and expand your published journal article to make it suitable for your thesis or dissertation

Alternatively, any author publishing with us can opt to retain their own copyright and sign a License to Publish.

back to top

Useful definitions

Version of Record (VoR)

"A fixed version of a journal article that has been made available by ... a publisher by formally and exclusively declaring the article 'published.'

This includes any 'early release' article that is formally identified as being published even before the compilation of a volume issue and assignment of associated metadata, as long as it is citable via some permanent identifier(s).

This does not include any 'early release' article that has not yet been 'fixed' by processes that are still to be applied, such as copy-editing, proof corrections, layout, and typesetting."

(Defined by National Information Standards Organization, in partnership with the Association of Learned and Professional Society Publishers.)

back to top

Useful links

- Creative Commons licenses
- UK Intellectual Property Office's What is copyright?" guide

Bibliography

Almalkie, S. & de Bruyn Kops, S. M., 2012 Kinetic energy dynamics in forced, homogeneous, and axisymmetric stably stratified turbulence. *J. Turbul.* **13** 1-32.

Augier, P. & Billant, P., 2011 Onest of secondary instabilities on the zigzag instability in stratified fluids. *J. Fluid Mech.* **682**, 120-131.

Augier, P., Chomaz, J.-M. & Billant, P., 2012 Spectral analysis of the transition to turbulence from a dipole in stratified fluid. *J. Fluid Mech.* **713**, 86-108.

Bartello, P., Métais, O. & Lesieur, M., 1996 Geostrophic versus wave eddy viscosities in atmospheric models. *J. Atmos. Sci.* **53**, 564-571.

Bartello, P. & Tobias, S. M., 2013 Sensitivity of stratified turbulence to the buoyancy Reynolds number. *J. Fluid Mech.* **725**, 1-22.

Batchelor, G. K., Canuto, V. M. & Chasnov, J. R., 1992 Homogeneous buoyancy-generated turbulence. *J. Fluid Mech.* **235**, 349-378.

Billant, P. & Chomaz, J.-M., 2000 Experimental evidence for a new instability of a vertical columnar vortex pair in a strongly stratified fluid. *J. Fluid Mech.* **418**, 167-188.

Billant, P. & Chomaz, J.-M., 2001 Self-similarity of strongly stratified inviscid flows. *Phys. Fluids* **13(6)**, 1645-1651.

Brethouwer, G., Billant, P., Lindborg, E. & Chomaz, J.-M., 2007 Scaling analysis and simulation of strongly stratified turbulent flows. *J. Fluid Mech.* **585**, 343-368.

Briscolini, M. & Santangelo, P., 1994 The non-Gaussian statistics of the velocity field in low-resolution large-eddy simulations of homogeneous turbulence. *J. Fluid Mech.* **270**, 199-218.

Brune, S. & Becker, E., 2013 Indications of stratified turbulence in a mechanistic GCM. *J. Atmos. Sci.* **70**, 231-247.

Cerutti, S., Meneveau, C. & Knio, O. M., 2000 Spectral and hyper viscosity in high-Reynolds-number turbulence. *J. Fluid Mech.* **421**, 307-338.

Carnevale, G. F., Briscolini, M. & Orlandi, P., 2001 Buoyancy- to inertial-range transition in forced stratified turbulence *J. Fluid Mech.* **427**, 205-239.

Chasnov, J. R., 1991 Simulation of the Kolmogorov inertial subrange using an improved subgrid model. *Phys. Fluids A* **3(1)**, 188-200.

Chollet, J.-P. & Lesieur, M., 1981 Parametrization of small scales of three-dimensional isotropic turbulence utilizing spectral closures *J. Atmos. Sci.* **38**, 2747-2757.

Chung, D. & Matheou, G., 2012 Direct numerical simulation of stationary homogeneous stratified sheared turbulence. *J. Fluid Mech.* **696**, 434-467.

Deardorff, J. W., 1971 On the magnitude of the subgrid scale eddy coefficient. *J. Comp. Phys.* **7** 120-133.

Deloncle, A., Billant, P. & Chomaz, J.-M., 2008 Nonlinear evolution of the zigzag instability in stratified fluids: a shortcut on the route to dissipation. *J. Fluid Mech.* **599**, 229-239.

Dewan, E. M., 1997 Saturated-cascade similitude theory of gravity wave spectra. *J. Geophys. Res.* **102**, D25, 29 799-29 817.

Domaradzki, A. J., Metcalfe, R. W., Rogallo, R. S. & Riley, J. J., 1987 Analysis of subgrid-scale eddy viscosity with use of results from direct numerical simulations. *Phys. Rev. Lett.* **58**, 547-550.

Domaradzki, A. J., Liu, W. & Brachet, M. E., 1993 An analysis of subgrid-scale interactions in numerically simulated isotropic turbulence. *Phys. Fluids A* **5**, 1747-1759.

Domaradzki, A. J. & Radhakrishnan, S., 2005 Effective eddy viscosities in implicit modelling of decaying high Reynolds number turbulence with and without rotation. *Fluid Dynamics Research* **36**, 385-406.

Durran, D., R. 2010 Numerical methods for fluid dynamics with application to geophysics. *Springer*, New York.

Gage, K. S., 1979 Evidence for a $k^{-5/3}$ law inertial range in mesoscale two-dimensional turbulence. *J. Atmos. Sci.* **36**, 1950-1954.

Germano, M., 1992 Turbulence: the filtering approach. *J. Fluid Mech.* **238**, 325-336.

Germano, M., Piomelli, U., Moin, P. & Cabot, W. H., 1991 A dynamic subgrid-scale eddy viscosity model. *Phys. Fluids A* **3(7)**, 1760-1765.

Ghosal, S., Lund, T. S., Moin, P. & Akselvoll, K., 1995 A dynamic localization model for large-eddy simulation of turbulent flows. *J. Fluid Mech.* **286**, 229-255.

Hebert, D. A. & de Bruyn Kops, S. M., 2006a Relationship between vertical shear rate and kinetic energy dissipation rate in stably stratified flows. *Geophys. Research Lett.* **33**, L06602.

Hebert, D. A. & de Bruyn Kops, S. M., 2006b Predicting turbulence in flows with strong stable stratification. *Phys. Fluids* **18**, 066602.

Herring, J. R. & Métais, O., 1989 Numerical experiments in forced stably stratified turbulence. *J. Fluid Mech.* **202**, 97-115.

Jiménez, J. R. & Moser, R. D., 2000 Large-eddy simulations: where are we and what can we expect? *AIAA Journal* **38(4)**, 605-612.

Kaltenbach, H.-K., Gerz, T. & Schumann, U., 1994 Large-eddy simulation of homogeneous turbulence and diffusion in stably stratified shear flow. *J. Fluid Mech.* **280**, 1-40.

Kang, H. S., Chester, S. & Meneveau, C., 2003 Decaying turbulence in an active-grid-generated flow and comparisons with large-eddy simulation. *J. Fluid Mech.* **480**, 129-160.

Khani, S. & Waite, M. L., 2013 Effective eddy viscosity in stratified turbulence. *J. of Turbl.* **14(7)**, 49-70.

Khani, S. & Waite, M. L., 2014 Buoyancy scale effects in large-eddy simulations of stratified turbulence. *J. Fluid Mech.* **754**, 75-97.

Khani, S. & Waite, M. L., Large eddy simulations of stratified turbulence: the dynamic Smagorinsky model. Submitted to *J. Fluid Mech.*, 2014.

Kleissl, J., Kumar, V., Meneveau, C. & Parlange, M. B., 2006 Numerical study of dynamic Smagorinsky model in large-eddy simulation of the atmospheric boundary layer: Validation in stable and unstable conditions. *Water Resour. Res.* **42**, W06D10.

Kimura, Y. & Herring, J. R., 2012 Energy spectra of stably stratified turbulence. *J. Fluid Mech.* **698**, 19-50.

Kolmogorov, A. N., 1941 The local structure of turbulence in incompressible viscous fluid for very large Reynolds number. *Dok. Akad. Nauk. SSSR* **30**, 301-305.

Kraichnan, R. H., 1967 Inertial ranges in two-dimensional turbulence. *Phys. Fluids* **10**, 1417-1423.

Kraichnan, R. H., 1976 Eddy viscosity in two and three dimensions. *J. Atmos. Sci.* **33**, 1521-1536.

Laval, J.-P., McWilliams, J. C. & Dubrulle, B., 2003 Forced stratified turbulence: Successive transition with Reynolds number. *Phys. Rev. E* **68**, 036308.

Leith, C. E., 1990 Stochastic backscatter in a subgrid-scale model: plane shear mixing layer. *Phys. Fluids A* **2(3)**, 297-299.

Leonard, A., 1974 Energy cascade in large eddy simulation of turbulent fluid flow. *Adv. Geophys.* **18**A, 237-248.

Lesieur, M., 1990 Turbulence in Fluids. *Kluwer Acad. Publrs.* Dordrecht.

Lesieur, M. & Métais, O., 1996 New trends in large-eddy simulations of turbulence, *Annu. Rev. Fluid Mech.* **28**, 45-82.

Lesieur, M. & Rogallo, R., 1989 Large-eddy simulation of passive scalar diffusion in isotropic turbulence. *Phys. Fluids A* **1(4)**, 718-722.

Lilly, D. K., 1967 The representation of small-scale turbulence in numerical simulation experiments. In *NCAR Manuscript* **281**, Nationl. Centr. for Atmosph. Res., Boulder, Co, USA, 99-164.

Lilly, D. K., 1983 Stratified turbulence and the mesoscale variability of the atmosphere. *J. Atmos. Sci.* **40**, 749-761.

Lilly, D. K., 1992 A proposed modification of the Germano subgrid-scale closure method. *Phys. Fluids A* **4(3)**, 633-635.

Lindborg, E., 2006 The energy cascade in strongly stratified fluid. *J. Fluid Mech.* **550**, 207-242.

Lu, H. & Porté-Agel, F., 2014 On the development of a dynamic non-linear closure for large-eddy simulation of the atmospheric boundary layer. *Boundary-Layer Meteorol*, doi:10. 1007/s10546-013-9906-y.

Lumley, J. L., 1964 The spectrum of nearly inertial turbulence in stably stratified fluid. *J. Atmos. Sci.* **21**, 99-102.

Marstorp, L., Brethouwer, G. & Johansson, A. V., 2007 A stochastic subgrid model with application to turbulent flow and scalar mixing. *Phys. Fluids* **19**, 035107.

Mashayek, A. & Peltier, W. R., 2013 Shear-induced mixing in geophysical flows: does the route to turbulence matter to its efficiency? *J. Fluid Mech.* **725**, 216-261.

Meneveau, C., 2012 Germano identity-based subgrid-scale modeling: a brief survey of variations on a fertile theme. *Phys. Fluids* **24**, 121301.

Meneveau ,C., & Katz J. 2000 Scale-invariance and turbulence models for large-eddy simulation. *Ann. Rev. Fluid Mech.* **32**, 1-32.

Meneveau, C., Lund, T. S. & Cabot, W. H. R., 1996 A Lagrangian dynamic subgrid-scale model of turbulence. *J. Fluid Mech.* **319**, 353-385.

Métais, O. & Lesieur, M., 1992 Spectral large-eddy simulation of isotropic and stably stratified turbulence. *J. Fluid Mech.* **239**, 157-194.

Moin, P. & Mahesh, K., 1998 Direct numerical simulation: A tool in turbulence research. *Annu. Rev. Fluid Mech.* **30**, 539-578.

Moin, P., Squires, K., Cabot, W. H. & Lee, S., 1991 A dynamic subgrid-scale model for compressible turbulence and scalar transport. *Phys. Fluids A* **3(11)**, 2746-2757.

O'Brien, J., Urzay, J., Ihme, M., Moin, P. & Saghafian, A., 2014 Subgrid-scale backscatter in reacting and inert supersonic hydrogen-air turbulent mixing layers. *J. Fluid Mech.* **743**, 554-584.

Orszag, S. A., 1971 On the elimination of aliasing in finite-difference schemes by filtering high-wavenumber components. *J. Atmos. Sci.* **28**, 1074-1074.

Paoli, R., Thouron, O., Escobar, J., Picot, J., & Cariolle, D., 2013 High-resolution large-eddy simulations of sub-kilometer-scale turbulence in the upper troposphere lower stratosphere. *Atmos. Chem. Phys. Discuss.* **13**, 31891-31932.

Piomelli, U., 1999 Large-eddy simulation: achievements and challenges. *Prog. Aerosp. Sci.* **35**, 335-362.

Piomelli, U., 2014 Large eddy simulations in 2030 and beyond. *Phil. Trans. R. Soc. A* **732**:20130320.

Piomelli, U., Cabot, W. H., Moin, P. & Lee, S., 1991 Subgrid-scale backscatter in turbulent and transitional flows. *Phys. Fluids A* **3(7)**, 1766-1771.

Pope, S. B., 2000 Turbulent Flows. *Cambridge University Press*, Cambridge.

Pope, S. B., 2004 Ten questions concerning the large-eddy simulation of turbulent flows. *New J. Phys.* **6(35)**, 1-24.

Porté-Agel, F., Meneveau, C. & Parlange, M. B., 2000 A scale-dependent dynamic model for large-eddy simulation: application to a neutral atmospheric boundary layer. *J. Fluid Mech.* **415**, 261-284.

Praud, O., Fincham, A. M. & Sommeria, J., 2005 Decaying grid turbulence in a strongly stratified fluid. *J. Fluid Mech.* **522**, 1-33.

Remmler, S. & Hickel, S., 2012 Direct and large eddy simulation of stratified turbulence. *Int. J. Heat Fluid Flow* **35**, 13-24.

Remmler, S. & Hickel, S., 2014 Spectral eddy viscosity of stratified turbulence. *J. Fluid Mech.* **755**, R6, doi:10.1017/jfm.2014.423.

Richardson, L. F., 1922 Weather prediction by numerical process. *Cambridge University Press*, Cambridge.

Riley, J. J. & de Bruyn Kops, S. M., 2003 Dynamics of turbulence strongly influenced by buoyancy. *Phys. Fluids* **15**, 2047-2059.

Riley, J. J., & Lelong, M.-P., 2000 Fluid motions in the presence of strong stable stratification. *Annu. Rev. Fluid Mech.* **32**, 613-657.

Riley, J. J., & Lindborg, E., 2008 Stratified turbulence: a possible interpretation of some geophysical turbulence measurements, *J. Atmos. Sci.* **65**, 2416-2424.

Rose, H. A. & Sulem, P. L., 1978 Fully developed turbulence and statistical mechanics. *Le Journal de Physique* **39**, 441-484.

Schaefer-Rolffs, U. & Becker, E., 2013 Horizontal momentum diffusion in GCMs using the dynamic Smagorinsky model *Mon. Wea. Rev.* **141**, 887-899.

Siegel, D. A. & Domaradzki, J. A., 1994 Large-eddy simulation of decaying stably stratified turbulence. *J. Phys. Oceanogr.* **24**, 2353-2386.

Smagorinsky, J., 1963 General circulation experiments with the primitive equations. I. The basic experiment *Mon. Weather Rev.* **91(3)**, 99-164.

Smith, L. M., & Waleffe F. 2002 Generation of slow large scales in forced rotating stratified turbulence. *J. Fluid Mech.* **451**, 145-168.

Smyth, W. D. & Moum, J. N., 2000 Anisotropy of turbulence in stably stratified mixing layers. *Phys. Fluids* **12(6)**, 1343.

Vallis, G. K., 2006 Atmospheric and oceanic fluid dynamics. *Cambridge University Press*, Cambridge.

Waite, M. L., 2014 Direct numerical simulations of laboratory-scale stratified turbulence. Modelling Atmospheric and Oceanic Flows: Insights from Laboratory Experiments, (eds. T. von Larcher & P. Williams), *American Geophysical Union*, Washington, DC., 159-175.

Waite, M. L., 2011 Stratified turbulence at the buoyancy scale. *Phys. Fluids A* **23**, 066602.

Waite, M. L. & Bartello, P., 2004 Stratified turbulence dominated by vortical motion. *J. Fluid Mech.* **517**, 281-303.

Wan, F. & Porté-Agel, F., 2011 Large-eddy simulation of stably-stratified flow over a steep hill. *Boundary-Layer Meteorol* **138**, 367-384.

Weinbrecht, S. & Mason, P. J., 2008 Stochastic backscatter for cloud-resolving models. Part I: implementation and testing in a dry convective boundary layer. *J. Atmos. Sci.* **65**, 123-139.